ISSN 2587-1366

TUJE

TURKISH JOURNAL OF ENGINEERING

VOLUME 5 ISSUE 1 JANUARY 2021

Dr. Ghazi DROUBI
Robert Gordon University Engineering Faculty
Scotland, UK

JOURNAL SECRETARY

Nida DEMİRTAŞ
nidademirtas@mersin.edu.tr

TURKISH JOURNAL OF ENGINEERING (TUJE)

Turkish Journal of Engineering (TUJE) is a multi-disciplinary journal. The Turkish Journal of Engineering (TUJE) publishes the articles in English and is being published 4 times (January, April, July and October) a year. The Journal is a multidisciplinary journal and covers all fields of basic science and engineering. It is the main purpose of the Journal that to convey the latest development on the science and technology towards the related scientists and to the readers. The Journal is also involved in both experimental and theoretical studies on the subject area of basic science and engineering. Submission of an article implies that the work described has not been published previously and it is not under consideration for publication elsewhere. The copyright release form must be signed by the corresponding author on behalf of all authors. All the responsibilities for the article belongs to the authors. The publications of papers are selected through double peer reviewed to ensure originality, relevance and readability.

AIM AND SCOPE

The Journal publishes both experimental and theoretical studies which are reviewed by at least two scientists and researchers for the subject area of basic science and engineering in the fields listed below:

Aerospace Engineering
Environmental Engineering
Civil Engineering
Geomatic Engineering
Mechanical Engineering
Geology Science and Engineering
Mining Engineering
Chemical Engineering
Metallurgical and Materials Engineering
Electrical and Electronics Engineering
Mathematical Applications in Engineering
Computer Engineering
Food Engineering

PEER REVIEW PROCESS

All submissions will be scanned by iThenticate® to prevent plagiarism. Author(s) of the present study and the article about the ethical responsibilities that fit PUBLICATION ETHICS agree. Each author is responsible for the content of the article. Articles submitted for publication are priorly controlled via iThenticate ® (Professional Plagiarism Prevention) program. If articles that are controlled by iThenticate® program identified as plagiarism or self-plagiarism with more than 25% manuscript will return to the author for appropriate citation and correction. All submitted manuscripts are read by the editorial staff. To save time for authors and peer-reviewers, only those papers that seem most likely to meet our editorial criteria are sent for formal review. Reviewer selection is critical to the publication process, and we base our choice on many factors, including expertise, reputation, specific recommendations and our own previous experience of a reviewer's characteristics. For instance, we avoid using people who are slow, careless or do not provide reasoning for their views, whether harsh or lenient. All submissions will be double blind peer reviewed. All papers are expected to have original content. They should not have been previously published and it should not be under review. Prior to the sending out to referees, editors check that the paper aim and scope of the journal. The journal seeks minimum three independent referees. All submissions are subject to a double blind peer review; if two of referees gives a negative feedback on a paper, the paper is being rejected. If two of referees gives a positive feedback on a paper and one referee negative, the editor can decide whether accept or reject. All submitted papers and referee reports are archived by journal Submissions whether they are published or not are not returned. Authors who want to give up publishing their paper in TUJE after the submission have to apply to the editorial board in written. Authors are responsible from the writing quality of their papers. TUJE journal will not pay any copyright fee to authors. A signed Copyright Assignment Form has to be submitted together with the paper.

PUBLICATION ETHICS

Our publication ethics and publication malpractice statement is mainly based on the Code of Conduct and Best-Practice Guidelines for Journal Editors. Committee on Publication Ethics (COPE). (2011, March 7). Code of Conduct and Best-Practice Guidelines for Journal Editors. Retrieved from http://publicationethics.org/files/Code%20of%20Conduct_2.pdf

PUBLICATION FREQUENCY

The TUJE accepts the articles in English and is being published 4 times (January, April, July and October) a year.

CORRESPONDENCE ADDRESS

Journal Contact: tuje@mersin.edu.tr

CONTENTS

Volume 5 – Issue 1

ARTICLES

Turkish Journal of Engineering

https://dergipark.org.tr/en/pub/tuje

e-ISSN 2548-0960

A brief review on attack design and detection strategies for networked cyber-physical systems

Mustafa Sinasi Ayas *[1]

[1]*Karadeniz Technical University, Engineering Faculty, Department of Electrical and Electronics Engineering, Trabzon, Turkey*

Keywords
Networked cyber-physical system
Cyber-security
Attack design
Attack detection
Control-theoretic
CPS

ABSTRACT

Networked cyber-physical systems (NCPSs) can be found in various fields such as industrial process, robotics, smart buildings, energy, healthcare systems, transportation, and surveillance. Recently accomplished real-time attacks indicate security vulnerabilities that weaken the reliability of NCPSs. Research areas on the security of NCPSs can be categorized into two groups: from the perspective of information security, from the perspective of control theory. In this paper, first possible attack locations on the control scheme of a NCPS which can be divided into three different groups namely sensor side, actuator side, and state estimator side are discussed and then a brief survey containing some recent studies on security strategies for NCPSs from the perspective of control theory is presented. After that attack detection strategies for a NCPS are briefly introduced and a general architecture utilized for attack detection on a NCPS is presented. In addition, some of recent studies on attack detection strategies for NCPSs from the perspective of control theory are discussed.

1. INTRODUCTION

Networked cyber-physical systems (NCPSs) compose of cyber (computation units and communication units) and physical (sensors and actuators) components interacting in a framework (Cárdenas et al. 2008) as shown in Fig. 1. Large-scale and distributed monitoring and control applications have led to increased interest on NCPSs in recent years. NCPSs can be found in various fields such as industrial process control (Wang et al. 2008), robotics (Meng et al. 2011), smart buildings (Kleissl and Agarwal 2010), energy (Barthels et al. 2011), healthcare systems (Lee and Sokolsky 2010), transportation (Lau et al. 2011), and surveillance (Chen et al. 2012). Although the integration of cyber and physical components in NCPSs increases system efficiency, it also exposes security vulnerabilities that weaken the reliability of critical NCPSs (Sandberg et al. 2015). Recently accomplished real-time attacks such as the Maroochy water breach (Slay and Miller 2007), multiple power blackouts in Brazil (Conti 2010), the StuxNet worm attack to Siemens' supervisory control and data acquisition (SCADA) systems (Karnouskos 2011), the SQL Slammer worm attack on the Davis-Besse nuclear plant (Kuvshinkova 2003) prove the mentioned security vulnerabilities in NCPSs. These successful attacks signify that information security mechanisms of NCPSs are insufficient to assure their healthy operation and NCPSs are prone to malfunction under attacks. Therefore, specifically designed control systems are required to complete the security mechanism (Pasqualetti et al. 2015).

Security of NCPSs is an up-to-date and challenging issue on which researchers have paid intensive attention to remedy the vulnerabilities. Basically, the research areas on the security of NCPSs can be categorized into two groups. In the first group, the researchers consider the issue from the perspective of information security, while the other group take into account the issue from the perspective of control theory.

In this paper, first, a brief survey on attack design strategies for NCPSs from the perspective of control theory is presented. Then, general architecture utilized for attack detection on a NCPSs is introduced. After that, some of recent papers on attack detection strategies for NCPSs from the perspective of control theory are

* **Corresponding Author**

*(msayas@ktu.edu.tr) ORCID ID 0000 – 0001 – 8113 – 4817

Cite this article

Ayas M S (2021). A brief review on attack design and detection strategies for networked cyber-physical systems. Turkish Journal of Engineering, 5(1), 01-07

Review Article / DOI: 10.31127/tuje.640282

Received: 30/10/2019; Accepted: 12/04/2020

discussed. In Section 2, the papers related to attack design for NCPSs are discussed. Section 3 introduces an architecture employed for attack detection on NCPSs and presents a brief literature review on attack detection strategies for NCPSs. Should be noted that the studies which is taken into account in this paper do not cover the all literature.

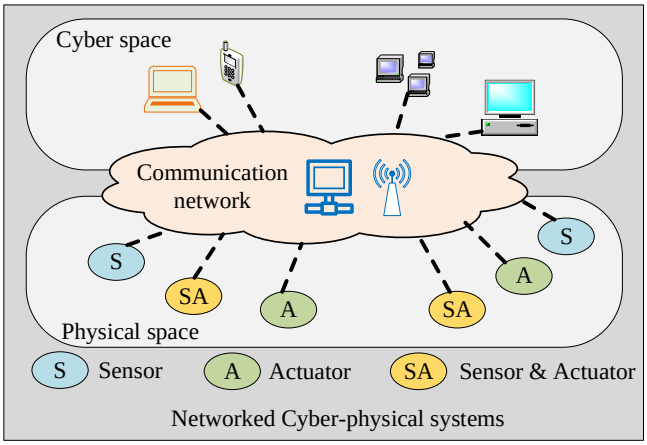

Figure 1. Holistic view of NCPSs

2. ATTACK DESIGN STRATEGIES FOR A NCPS

Possible attack locations on the control scheme of a NCPS can be categorized into three different groups: sensor side, actuator side, and state estimator side. Sensor side attacks are performed by spoofing measured sensor signals, i.e. the real time sensor data are modified by the attacker. Similarly, in the actuator side attacks, the attacker spoof the produced control signals required for actuators. State estimator side attacks can be either at the output or input of the estimator, i.e. attacker can modify either estimated state values or control signals provided as input to the estimator. These mentioned attacks are actually performed at the input-output of the main blocks such as controller, system and estimator in a closed loop system. Note that this paper does not cover attacks performed on cyber-side to change parameters of the controller.

Assume that physical plant is modelled in continuous-time state-space form given in Eq. (1) and a controller based observer has the form presented in Eq. (2).

$$\begin{aligned} \dot{x}(t) &= Ax(t) + Bu(t) \\ y(t) &= Cx(t) + Du(t) \end{aligned} \tag{1}$$

$$\begin{aligned} \dot{\hat{x}}(t) &= A\hat{x}(t) + Bu(t) + L(y(t) - C\hat{x}(t) + Du(t)) \\ u(t) &= -K\hat{x}(t) + Gr(t) \end{aligned} \tag{2}$$

where *r(t)* is reference input signal, *(A,C)* is observable, *(A,B)* is controllable, $\hat{x}(t)$ represents state vector of the observer, *u(t)* is the produced control signal, G is a prefilter matrix determined considering steady-state error, *L* and *K* matrices are chosen such that $(A-LC)$ and $(A-BK)$ are Hurwitz.

The block diagram of the physical plant model and controller based observer given in Eqs. (1 and 2) is shown in Fig. 2.

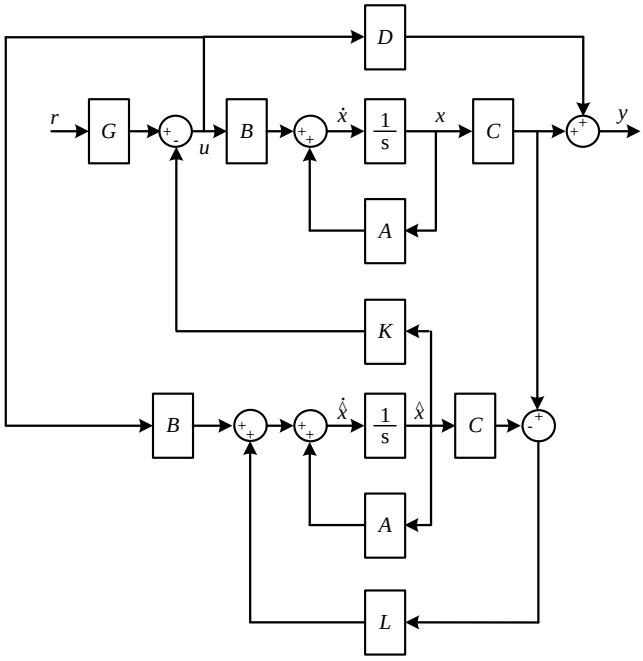

Figure 2. The block diagram of the physical plant model and controller based observer

2.1. Sensor Side Attacks

A sensor side attack can be represented by a time varying $\Delta y(t)$ signal which is added to measured sensor data by the attacker (Djouadi et al. 2014). By spoofing sensor data, the output of the system represented by *y(t)* is modified and general state-space model is written as in Eq. (3).

$$\begin{aligned} \dot{x}(t) &= Ax(t) + Bu(t) \\ y_a(t) &= Cx(t) + Du(t) + \Delta y(t) \end{aligned} \tag{3}$$

where $y_a(t)$ corresponds system output under attack.

2.2. Actuator Side Attacks

Actuator side attacks are employed to spoof control signals directly utilized in state-space models. Assume that a time varying $\Delta u(t)$ signal is added to the produced control signal. Then, the state-space model of the plant is written as in Eq. (4) (Ayas and Djouadi 2016).

$$\begin{aligned} \dot{x}(t) &= Ax(t) + B(u_a(t)) \\ y(t) &= Cx(t) + D(u_a(t)) \end{aligned} \tag{4}$$

where $u_a(t) = u(t) + \Delta u(t)$ represent modified control signal.

2.3. State Estimator Side Attacks

In this case, the attacker is able to spoof either the input of the estimator, i.e. control signals provided as input to the estimator, or the output of the estimator, i.e. estimated state vector. If the attacker modify only the input control signal of the estimator then controller based observer has the following form in Eq. (5).

On the other hand, the attacker can directly modify the output of the estimator by adding a $\Delta\hat{x}(t)$ signal to the

estimated state vector. In this case, the model of the controller based observer is written as in Eq. (6).

A general closed loop system containing state estimator for a NCPS is demonstrated in Fig. 3. In the figure, possible attack locations for the mentioned three category are emphasized with red icons.

$$\dot{\hat{x}}_a(t) = A\hat{x}(t) + B(u(t) + \Delta u_o(t)) + L(y(t) - C\hat{x}(t) + D(u(t) + \Delta u_o(t)))$$
$$u(t) = -K\hat{x}_a(t) + Gr(t) \quad (5)$$

$$\dot{\hat{x}}_a(t) = A(\hat{x}(t) + \Delta\hat{x}(t)) + Bu(t) + L(y(t) - C(\hat{x}_a(t) + \Delta\hat{x}(t)) + Du(t))$$
$$u(t) = -K(\hat{x}(t) + \Delta\hat{x}(t)) + Gr(t) \quad (6)$$

where $\hat{x}_a(t)$ represent the attacked state vector.

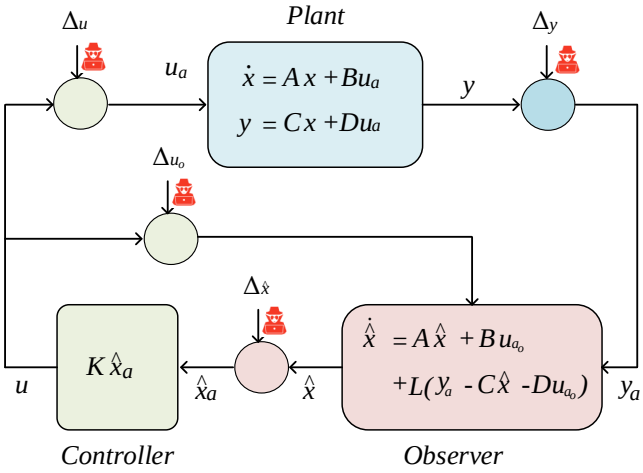

Figure 3. Possible actuator, sensor, and state attacks on a general closed loop system

Unlike traditional IT systems, where security is based on the advocacy of data-related features and services, cyber attacks on NCPS can affect physical processes due to their feedback structure. Hence, NCPS security should take into account threats on both the cyber and physical layers. Within this scope three dimensional attack-scenario space seen in Fig. 4. was presented in (Teixeira et al. 2015) by considering control systems perspective. Commonly used specific attack types such as replay attack, denial-of-service (DoS) attack, bias-injection attack, zero dynamics attack, eavesdropping attack and covert attack are positioned in the attack space considering axes which are system knowledge, disruption resources and disclosure resources. For example, DoS and eavesdropping attacks require only disruption and disclosure resources, respectively, whereas replay attack utilizes both of the resources. On the other hand, for a covert attack model knowledge is necessary in addition to disruption and disclosure resources.

The general approach in attack design for a NCPS has been to focus on the effect of specific attacks against the NCPS. (Amin et al. 2009) have studied the effect of deception and DoS attacks on discrete-time linear dynamical systems. Deception attacks aim to compromise the trustworthiness of some data of sensors and actuators by changing their values. On the other hand, DoS attacks compromise availability of sensor and actuator data by jamming the communication channel. As a result legitimate users are unable to get a respond to their requests, i.e. a lack of accessibility of sensor and actuator components occurs.

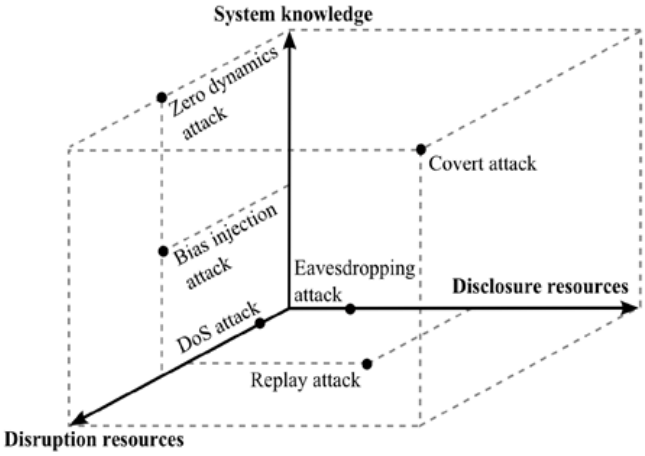

Figure 4. Three dimensional attack-scenario space (Teixeira et al. 2015)

(Mo et al. 2010) presented specific deception attacks named false data injection attacks against state estimator used in a discrete-time linear time-invariant Gaussian system. A Kalman filter was used as state estimator in the study. The false data injection attack scenario designed as a constrained control problem and the solution of this problem is provided using ellipsoidal approximation approach to show the solution space of the control problem.

(Liu et al. 2011) studied the effect of false data injection attacks against state estimators in electric power systems. The researchers successfully launched the false data injection attacks to state estimator and injected arbitrary errors into the certain state variables without being detected. The study indicates that design of undetectable false data injection attacks is possible even the adversary has limited resources.

(Teixeira et al. 2010) introduced stealthy deception attacks against state estimators in SCADA system operating in power grids. The researchers indicated that widely used bad data detection hypothesis tests, i.e. the performance index test and the largest normalized residual test, do not guarantee detection of cyber-attacks.

(Djouadi et al. 2014) studied on sensor signal attacks on observer-based controlled systems and formulate optimal sensor attack for both finite and infinite horizon linear quadratic (LQ) control. Then, the researchers considered actuator signal attack case and introduce optimal actuator attack for both finite and

infinite horizon LQ control on observer-based controlled systems (Djouadi et al. 2015).

(Ayas and Djouadi 2016) focused on theoretical analysis of undetectable sensor and actuator attacks on observer-based controlled systems. The researchers formulated explicit equations of both undetectable sensor and actuator signal attacks. Furthermore, they showed that the actuator signal attack is optimal in the sense of minimal energy attack signal.

(Hao et al. 2015) introduced stealthy attack design strategies for state estimators in power grid. The researchers indicated that the proposed random attack construction algorithm is able to launch exceptionally sparse attack vectors and these attacks successfully compromise certain state variables.

(Feng et al. 2017) presented a deep learning-based framework to launch stealthy attacks on industrial control systems with minimal a-priori knowledge of system. The researchers also showed that the proposed framework contains an adversarial learning method providing bypass the employed anomaly detector. In addition, the framework determined the optimal amount of bias injection at each time step.

(Wu et al. 2018) studied on the effect of optimal data injection attack which is characterized considering optimal control theory. Two different design problem were considered by the researchers who emphasized that the proposed optimal attack strategies have a high possibility to be launched. The impressive side of this study is that the adversaries can analyze the worst case impact of the applied attack according to the attack location.

(Lu and Yang 2020) examined the effects of false data injection attacks on power networks under sensor failures. A bad data detector and a state estimator were used in the power networks. They design a class of sparse undetectable attack (SUA) to decrease state estimation performance without being detected. The effectiveness of the proposed SUA design was demonstrated using IEEE 5, 9, and 30-bus systems. The proposed SUA disrupt the state estimator and as a result, the bad data detector fails to detect both sensor failures and the designed attacks.

(Song et al. 2019) studied on problem of state estimation problem for multi-sensor systems subjected to undetectable attacks. First, a sufficient condition was derived for the undetectable attack. Then, an undetectable attack design method was presented. The researchers showed the performance of the proposed attack scheme and estimator under by carrying out a simulation example.

3. ATTACK DETECTION STRATEGIES for a NCPS

Attack detection strategies for a NCPS should take both cyber and physical layers of the NCPS into consideration. In addition to traditional IT systems considering network traffic and try to keep data safe, physical plant should also be taken into account to detect attacks. Therefore, a model of the physical plant is required to predict behavior of the plant to a known control input signal. Assume that the control signal $u_a(t)$ seen in Fig. 3 is a regular control signal produced by the controller, i.e. $u_a(t)$ is not under attack, and $u_a(t)$ can be monitored meaning that it is known. Then, using the model of the physical plant, expected output signal, i.e. $\hat{y}(t)$ can be estimated. The estimated output signal is simply compared to measured sensor output signal $y(t)$ to potentially detect any sensor side attack mentioned in the previous section. If the attacker has spoofed the sensor data, an alarm is triggered at that time. The same scenario can be modified to detect actuator side attacks and state estimator side attacks. Note that there might be false alarm depending of the estimation accuracy of the considered signals, i.e. $\hat{y}(t)$, $\hat{u}_a(t)$, and $\hat{x}_a(t)$. As a result, in order to detect attacks on a physical plant, the model of the plant and a detector, i.e. anomaly detection algorithm, are required. Fig. 5. shows a general architecture utilized for attack detection on a NCPS. Should be noted that the detector part of the framework is actually the main part that the researchers focus on to detect subjected attacks summarized in Fig. 4. For instance, (Mo et al. 2014) proposed χ^2 failure detector to detect replay attack, while (Hu et al. 2019). proposed a residual based detection approach by using skewness analysis of the residual signal. In the architecture given in Fig. 5., alarm is triggered by considering both produced control signals and measured output sensor signals. In the scenario given in the figure, attackers spoof both actuator A_2 and sensor S_2 and so alarm is triggered.

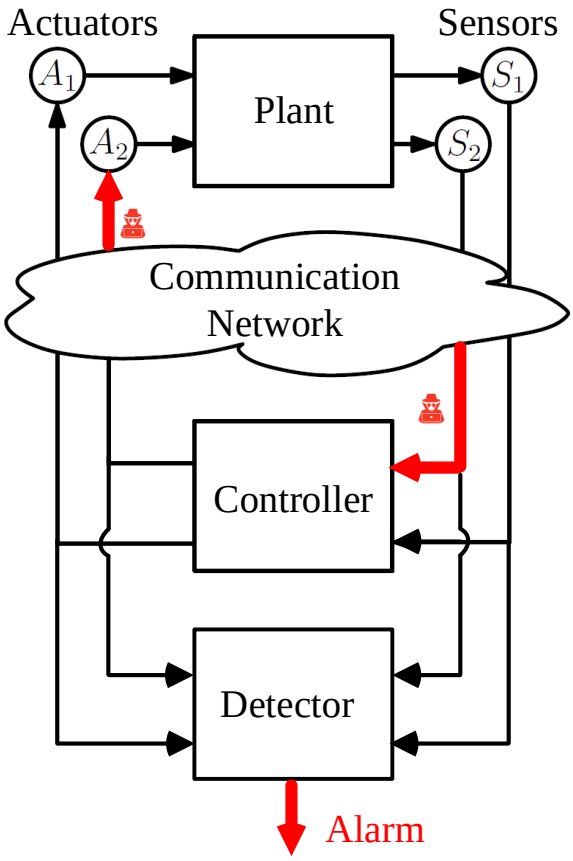

Figure 5. A general architecture utilized for attack detection

The aforementioned attack detection architecture actually based on monitoring regular behavior of the physical plant. By considering this manner, researchers

have performed studies on attack detection strategies for NCPSs from the perspective of control theory. Some of recent ones are discussed below.

(Pasqualetti et al. 2013) designed both distributed and centralized attack detection and identification monitors by considering monitoring limitations of CPSs subject to exogenous attacks. The IEEE 118 bus system and the IEEE RTS96 power network subjected to false data injection attack were utilized to show the effectiveness of the designed monitors even under noises and uncertainties. (Pasqualetti et al. 2013) showed that dynamic monitors have superiority over static monitors.

(Manandhar et al. 2014) studied detection of false data injection attacks on smart grids. They presented a robust security framework based on the χ^2 detector and Euclidean detector, which was also proposed in the study. Kalman filter which fed these detectors was used as the estimator. The proposed framework was tested on IEEE 9-bus power systems both using χ^2 detector and Euclidean detector. The obtained results show that Euclidean detector is capable of detecting statistically derived false data injection attacks while χ^2 detector is not capable of detecting them.

(Liu et al. 2014) introduced a false data detection framework for power grids. They defined detection of false data injection attacks as a matrix separation problem. Low rank matrix factorization and nuclear norm minimization were used to solve this problem. IEEE 57 and 118-bus systems were utilized in numerical experiments to illustrate the performance of the proposed detection framework. The results indicate that malicious attacks in the power grids are detected by the framework.

(Mo et al. 2014) presented a problem containing Kalman estimator, LQG optimal controller, and χ^2 failure detector for an LTI system. They showed that replay attack is feasible and proposed countermeasures against replay attack. A zero-mean Gaussian noise signal was utilized as authentication signal. The authentication signal was added as a marking to optimal control signal produced by the LQG controller. Although this marking process improved detectability of the replay attack, the control performance of the system was decreased. Therefore, the relationship between control performance and detection rate was characterized in the study by considering maximum control performance and detection rate.

(Rawat et al. 2015) introduced the χ^2 detector and cosine similarity matching approaches in order to detect false data injection attacks on smart grids. Kalman filter was utilized to estimate expected measurement values and a comparison was performed between the estimated and measured real values for attack detection. Numerical experiments were carried out and the results indicate that cosine similarity matching approach is capable of detecting both false data injection attacks and random attacks whereas χ^2 detector is competent of detecting only random attacks.

(Deng et al. 2017) proposed a defense framework against false data injection attacks on power systems. They designed a least-budget defense framework to enhance immunity against this kind of attacks by considering the relationship of a rational attacker and defender. In addition, (Deng et al. 2017) presented solution to meter selection problem, which was considered as a mixed integer nonlinear programming problem and solved thanks to Bender's decomposition. Numerical experiments were carried out by using IEEE 9, 14, 30, 118, and 300-bus systems to verify the proposed defense framework.

(Hu et al. 2019) focused on detection of stealthy attacks on CPSs. They proposed a residual based detection approach by using skewness analysis of the residual signal. Hu et al. showed that a residual signal has a skewed distribution if an adversary perform a specific attack. Therefore, stealthy attacks on CPSs can be detected by considering residual skewness coefficients obtained from regular case, i.e. attack-free case, and under attack case of the CPSs. On two different experiments, effectiveness of the skewness analysis based approach was verified. The researchers indicated that the proposed approach has the disadvantage of parameter selection which depends on human experience. It was emphasized that the proposed approach is suitable for real-time implementation.

(Li et al. 2019) presented a cyberattack detection framework based on online learning algorithms for industrial control system. The researchers proposed adaptive regularized cost-sensitive multiclass online learning scheme to detect cyberattack in the industrial control system. They utilized power system and gas pipeline to demonstrate the performance of the proposed cyberattack detection framework. The results show that the proposed online learning scheme is effective for cyberattack detection in industrial control systems.

(Luo et al. 2019) proposed a framework for smart grids to detect bias injection attacks and isolate them. They introduced nonlinear observer-based distributed detection method, which was demonstrated to be robust against external disturbances. In addition, the researchers also presented an interval residual-based detection standard to emphasize the restrictions of the predefined threshold.

4. CONCLUSION

Some of the studies in the literature about attack design and detection strategies for NCPSs from the perspective of control theory are briefly presented in this paper. In most of the studies, researchers assume that all state variables are either accurately measurable or determined utilizing some kind of estimators. Furthermore, some of them formulate the attack strategy for either single-input and single-output (SISO) systems or multiple-input and multiple-output (MIMO) systems. However, uncertainties of system parameters and process noises should be considered. In addition, attack design strategies should be characterized for both SISO and MIMO systems. One more opinion is to focus on optimal attack strategies to inject worst case attack to NCPs instead of specific attacks based on many assumptions.

In a general manner, attack design and detection strategies for NCPSs is a difficult issue and requires approaches from different areas such as robust control, fault-tolerant control, systems, networked control systems and big data analysis.

REFERENCES

Amin S, Cárdenas A A & Sastry S S (2009). Safe and secure networked control systems under denial-of-service attacks. In International Workshop on Hybrid Systems: Computation and Control. Springer, Berlin, Heidelberg, 5469, 31-45. ISBN 978-3-642-00602-9

Ayas M S & Djouadi S M (2016). Undetectable sensor and actuator attacks for observer based controlled Cyber-Physical Systems. IEEE Symposium Series on Computational Intelligence, 1-7. DOI: 10.1109/SSCI.2016.7849882

Barthels A, Ruf F, Walla G, Fröschl J, Michel H U & Baumgarten U (2011). A model for sequence based power management in cyber physical systems. In International Conference on Information and Communication on Technology. Springer, Berlin, Heidelberg, 87-101. ISBN 978-3-642-23447-7

Cárdenas A A, Amin S & Sastry S (2008). Secure control: Towards survivable cyber-physical systems. The 28th International Conference on Distributed Computing Systems Workshops, Beijing, China, 495-500. DOI: 10.1109/ICDCS. Workshops.2008.40

Chen J, Tan R, Xing G, Wang X & Fu X (2012). Fidelity-aware utilization control for cyber-physical surveillance systems. IEEE Transactions on Parallel and Distributed Systems, 23(9), 1739-1751. DOI: 10.1109/TPDS.2012.74

Conti J P (2010). The day the samba stopped [power blackouts]. Engineering & Technology, 5(4), 46-47. DOI: 10.1049/et.2010.0410

Deng R, Xiao G & Lu R (2017). Defending against false data injection attacks on power system state estimation. IEEE Transactions on Industrial Informatics, 13(1), 198-207. DOI: 10.1109/TII.2015.2470218

Djouadi S M, Melin A M, Ferragut E M, Laska J A & Dong J (2014). Finite energy and bounded attacks on control system sensor signals. 2014 American Control Conference, Portland, Oregon, USA, 1716-1722. DOI: 10.1109/ACC.2014.6859001

Djouadi S M, Melin A M, Ferragut E M, Laska J A, Dong J & Drira A (2015). Finite energy and bounded actuator attacks on cyber-physical systems. 2015 European Control Conference (ECC), Linz, Austria, 3659-3664. DOI: 10.1109/ECC.2015.7331099

Feng C, Li T, Zhu Z & Chana D (2017). A deep learning-based framework for conducting stealthy attacks in industrial control systems. arXiv preprint arXiv:1709.06397. Available online: https://arxiv.org/abs/1709.06397

Hao J, Piechocki R J, Kaleshi D, Chin W H & Fan Z (2015). Sparse malicious false data injection attacks and defense mechanisms in smart grids. IEEE Transactions on Industrial Informatics, 11(5), 1-12. DOI: 10.1109/TII.2015.2475695

Hu Y, Li H, Yang H, Sun Y, Sun L & Wang Z (2019). Detecting stealthy attacks against industrial control systems based on residual skewness analysis. EURASIP Journal on Wireless Communications and Networking, 74. DOI: 10.1186/s13638-019-1389-1

Karnouskos S (2011). Stuxnet worm impact on industrial cyber-physical system security. IECON 2011-37th Annual Conference of the IEEE Industrial Electronics Society, Melbourne, VIC, Australia, 4490-4494. DOI: 10.1109/IECON.2011.6120048

Kleissl J & Agarwal Y (2010). Cyber-physical energy systems: Focus on smart buildings. Design Automation Conference, Anaheim, CA, USA, 749-754. DOI: 10.1145/1837274.1837464

Kuvshinkova S (2003). SQL Slammer worm lessons learned for consideration by the electricity sector. North American Electric Reliability Council, 1(2), 5.

Lau J K S, Tham C K & Luo T (2011). Participatory cyber physical system in public transport application. 2011 Fourth IEEE International Conference on Utility and Cloud Computing, Victoria, NSW, Australia, 355-360. DOI: 10.1109/UCC.2011.59

Lee I & Sokolsky O (2010). Medical cyber physical systems. Design automation conference, Anaheim, CA, USA, 743-748.

Li G, Shen Y, Zhao P, Lu X, Liu J, Liu Y & Hoi S C H (2019). Detecting cyberattacks in industrial control systems using online learning algorithms. Neurocomputing, 364, 338-348. DOI: 10.1016/j.neucom.2019.07.031

Liu L, Esmalifalak M, Ding Q, Emesih V A & Han Z (2014). Detecting false data injection attacks on power grid by sparse optimization. IEEE Transactions on Smart Grid, 5(2), 612-621. DOI: 10.1109/TSG.2013.2284438

Liu Y, Ning P & Reiter M K (2011). False data injection attacks against state estimation in electric power grids. ACM Transactions on Information and System Security (TISSEC), 14(1), 13. DOI: 10.1145/1952982.1952995

Lu A Y & Yang G H (2020). False data injection attacks against state estimation in the presence of sensor failures. Information Sciences, 508, 92-104. DOI: 10.1016/j.ins.2019.08.052

Luo X, Wang X, Zhang M & Guan X (2019). Distributed detection and isolation of bias injection attack in smart energy grid via interval observer. Applied Energy, 256, 113703. DOI: 10.1016/j.apenergy.2019.113703

Manandhar K, Cao X, Hu F & Liu Y (2014). Detection of faults and attacks including false data injection attack in smart grid using Kalman filter. IEEE transactions on control of network systems, 1(4), 370-379. DOI: 10.1109/TCNS.2014.2357531

Meng W, Liu Q, Xu W & Zhou Z (2011, September). A cyber-physical system for public environment perception and emergency handling. IEEE International Conference on High Performance Computing and Communications, Banff, AB, Canada, 734-738. DOI: 10.1109/HPCC.2011.104

Mo Y, Chabukswar R & Sinopoli B (2014). Detecting integrity attacks on SCADA systems. IEEE Transactions on Control Systems Technology, 22(4), 1396-1407. DOI: 10.1109/TCST.2013.2280899

Mo Y, Garone E, Casavola A & Sinopoli B (2010). False data injection attacks against state estimation in wireless sensor networks. 49th IEEE Conference on Decision and Control (CDC), Atlanta, GA, USA, 5967-5972. DOI: 10.1109/CDC.2010.5718158

Pasqualetti F, Dörfler F & Bullo F (2013). Attack detection and identification in cyber-physical systems. IEEE transactions on automatic control, 58(11), 2715-2729. DOI: 10.1109/TAC.2013.2266831

Pasqualetti F, Dorfler F & Bullo F (2015). Control-theoretic methods for cyberphysical security: Geometric principles for optimal cross-layer resilient control systems. IEEE Control Systems Magazine, 35(1), 110-127. DOI: 10.1109/MCS.2014.2364725

Rawat D B & Bajracharya C (2015). Detection of false data injection attacks in smart grid communication systems. IEEE Signal Processing Letters, 22(10), 1652-1656. DOI: 10.1109/LSP.2015.2421935

Sandberg H, Amin S & Johansson K H (2015). Cyberphysical security in networked control systems: An introduction to the issue. IEEE Control Systems Magazine, 35(1), 20-23. DOI: 10.1109/MCS.2014.2364708

Slay J & Miller M (2007). Lessons learned from the maroochy water breach. International Conference on Critical Infrastructure Protection, Springer, Boston, MA, 73-82.

Song H, Shi P, Lim C C, Zhang W A & Yu L (2019). Attack and estimator design for multi-sensor systems with undetectable adversary. Automatica, 109, 108545. DOI: 10.1016/j.automatica.2019.108545

Teixeira A, Amin S, Sandberg H, Johansson K H & Sastry S S (2010). Cyber security analysis of state estimators in electric power systems. 49th IEEE conference on decision and control (CDC), Atlanta, GA, USA, 5991-5998. DOI: 10.1109/CDC.2010.5717318

Teixeira A, Shames I, Sandberg H & Johansson K H (2015). A secure control framework for resource-limited adversaries. Automatica, 51, 135-148. DOI: 10.1016/j.automatica.2014.10.067

Wang Y, Vuran M C & Goddard S (2008). Cyber-physical systems in industrial process control. ACM Sigbed Review, 5(1), 12. DOI: 10.1145/1366283.1366295

Wu G, Sun J & Chen J (2018). Optimal data injection attacks in cyber-physical systems. IEEE transactions on cybernetics, 48(12), 3302-3312. DOI: 10.1109/TCYB.2018.2846365

Turkish Journal of Engineering

https://dergipark.org.tr/en/pub/tuje

e-ISSN 2548-0960

Microstructure and mechanical properties of similar and dissimilar laser welds of dp600 and dp1000 steel sheets used in the automotive industry

Oguz Tuncel*[1], Hakan Aydın[1], Sukriye Cetin[1]

[1]*Bursa Uludağ University, Engineering Faculty, Mechanical Engineering Department, Bursa, Turkey*

Keywords
Nd:YAG laser welding
DP600 steel
DP1000 steel
Mechanical properties
Microstructure

ABSTRACT

Dual-phase (DP) steel sheets are the most widely used steel group in the automotive industry. When these steel sheets are used in car body components, welding is inevitably needed during the manufacturing process. Although the resistance spot welding (RSW) is the most widely used welding method in the automotive industry, the newly popular laser welding has gained more importance in the welding of these steel grades in recent years. In this work, the DP600 and DP1000 steel sheets were joined as double-sided with the pulsed Nd: YAG (Neodymium-doped Yttrium Aluminum Garnet (Y3Al5O12)) laser welding. Performing similar or dissimilar weld of DP steel sheets is an inevitable demand in the modern automotive industry. So, in this study similar (DP600-DP600, DP1000-DP1000) and dissimilar (DP600-DP1000) steel sheets were welded in the flat position with the butt joint. In order to evaluate welding performance, microstructural studies and mechanical tests were performed, and experiments carried out in this context include optical microscope studies, tensile tests and Vickers microhardness measurements. The tensile strength of the similar welded joints is a little bit lower than the base metals (BM). But, for dissimilar weld, the tensile strength is even lower than DP600-DP600 joint. And the microstructure of the welded joints are composed of martensite, retained austenite and bainite in the fusion zone and a mixture of martensite, bainite, ferrite, retained austenite and tempered martensite in heat affected zone (HAZ).

1. INTRODUCTION

Dual-phase (DP) steels have commonly used as advanced high strength steel (AHSS) in the automotive industry nowadays to reduce vehicle weight, improve fuel economy and passenger safety. The term dual phase is due to its microstructure. The combination of DP steels consists of soft ferrite matrix and hard martensitic phase. In this combination of two phases, hard martensite phase provides the high strength and soft ferrite matrix provides good formability and ductility. The volume fraction of the martensite determines the strength and grade of the DP steel (Liu et al. 2015; Dong et al. 2014; Saha et al. 2014). The steels used automotive industry must be easy formable, weldable, coatable and repairable. For having these features, DP steels are being implemented in auto-body parts easily like floor panel, hood outer, quarter panel inner, rear rails, safety cage components, etc. (Bandyopadhyay et al. 2016; Hazratinezhad et al. 2012)

Welding is the mostly used joining technique during the manufacturing of automotive body components. Recently, laser welding has gained popularity because of flexibility, ease of automation, high welding speed, high power density, small heat affected zone (HAZ), high weld bead depth-to-width ratio and low thermal distortion of the workpiece. So, laser welding has been considered potentially replace with other commonly used fusion welding techniques such as resistance and arc welding (Sharma and Molian 2011; Yuce et al. 2017; Mohammadpour et al. 2018). Also, pulsed Nd:YAG laser welding has several advantages over the other laser sources because of control the laser parameters precisely including pulse duration and pulse frequency (Hekmatjou and Naffakh-Moosavy 2018).

There are several studies on the laser welding of DP steels in the literature. (Parkes et al. 2013) studied the evaluation the microstructure and fatigue properties of fiber laser welded (FLWed) high strength low alloy (HSLA) and dual–phase (DP980) steels in similar and dissimilar combinations. The weld zone contained martensite, bainite, tempered martensite, and ferrite phases. Soft zone occurred on DP980 side and lower microhardness values than the base metal (BM) were

* **Corresponding Author**

*(otuncel@uludag.edu.tr) ORCID ID 0000 – 0002 – 6886 – 6367
(hakanay@uludag.edu.tr) ORCID ID 0000 – 0001 – 7364 – 6281
(sukriyecetin7@gmail.com) ORCID ID 0000 – 0002 – 3888 – 699X

Cite this article

Tuncel O, Aydın H & Cetin S (2021). Microstructure and mechanical properties of similar and dissimilar laser welds of dp600 and dp1000 steel sheets used in the automotive industry. Turkish Journal of Engineering, 5(1), 08-14

Research Article / DOI: 10.31127/tuje.649975

Received: 22/11/2019; Accepted: 02/01/2020

measured in this zone. (Fernandes et al. 2017) aimed to determine the weldability and optimum welding parameters of Nd: YAG laser welded DP600 sheets. As a result of the hardness studies, they found a hardness increase of nearly 100% in the melting zone compared to the BM. (Wang et al. 2016) investigated the effect of energy input on the microstructure and mechanical properties of DP1000 steel butt joint using Nd:YAG laser welding. They measured 86-91% of the strength of the DP1000 steel BM of laser welded joints, and detected tempered martensite in the HAZ. (Xia et al. 2008) made the Nd:YAG laser welds on DP450, DP600 and DP980 steels over a wide range of heat inputs. In the result of their study, the total extent of HAZ softening in a DP weld at large heat input was proportional to the martensite content of the steel. (Węglowski et al. 2009) investigated the microstructure, mechanical properties, fatigue strength and residual stresses of laser welded dual phase HDT580X steel. The results of their study revealed that the HDT 580X steel was characterized by good laser weldability. In their study, the tensile strength of the welded joints was about BM, and microstructure of the welded joints was composed of lath martensite in the fusion zone and mixture of lath martensite, bainite and ferrite in the HAZ. (Sun et al. 2016) studied the metallurgical phenomena of welded joints of DP590 steel sheets using pulsed laser with increasing pulse frequency. They showed that increasing pulse led to an increase in overlapping factor (-22.5%-75.5%) and average power between two laser spots, which could result in penetration depth increasing. Also, in their study over 54.5% overlapping factor, they achieved 100% penetration depth. (Di et al. 2017) fiber laser welded 1.5 mm thick dissimilar DP780 and DP980 steel sheets. In their study, in the HAZ region tempered martensite and retained austenite were the reason of the decrease in hardness compared the BM.

This study aims to investigate the pulsed Nd:YAG laser welding capabilities of similar and dissimilar DP steels (DP600-DP600, DP600-DP1000, DP1000-DP1000), which are increasingly used in the automobile industry. Welding operations were conducted as double-sided. Vickers microhardness measurements and tensile tests were carried out to determine the mechanical properties of welds. Also, the weld region was examined using an optical microscope for macrostructure and microstructure studies.

2. EXPERIMENTAL DETAILS

Commercial DP600 and DP1000 steel sheets with a thickness of 1 mm were selected for this study. The chemical composition and tensile properties of the BM's were listed in Tab. 1 and 2, respectively. DP600 and DP1000 steel sheets were cut into pieces in dimensions of 100 mm x 260 mm before the welding processes. Laser welding operations were performed by assembling the sheets in the square butt-joint configuration using a pulsed SISMA SWA 300 Nd:YAG laser welding machine with a maximum mean power of 300W. A special fixture was made to ensure complete contact between the forehead surface of the weld samples, and this fixture was mounted to the workbench of the welding machine (Fig. 1). All welds were conducted perpendicular to the rolling direction (Fig. 2a). Argon shielding gas was employed during laser welding operations. The focal length was 120 mm above the sheet surface. The capacity of the welding device was insufficient for single-sided welding. Therefore the welds were performed as double-sided DP600-DP600, DP600-DP1000 and DP1000-DP1000 in constant parameters 65% charge, 5 ms pulse duration, 5 Hz frequency, 1.4 mm focal spot diameter and 4 mm/s welding speed (Table 3). In the double-sided welding process, first the front face was welded, then the other face was welded. Weld parameters were chosen according to the experience of the authors in their previous studies and the welding device capacity also considered. With these parameters overlapping factor calculated 43.66% by using the formula in Eq. 1 (Sun et al. 2016).

$$Q_f = [1- (V/f) / (D+VT)] \times 100 \quad (1)$$

Where V is welding speed (4 mm/s), f is pulse frequency (5 hz), T is pulse duration (5ms) and D refers to laser spot size on the workpiece (1.4 mm).

The welded samples were machined perpendicular to the welding direction in accordance with ASTM E8/E8M (ASTM 2009) (Fig. 2b). To evaluate the mechanical properties of the welds, the uniaxial tensile tests were carried out on a computerized UTEST-7014 tensile testing machine at room temperature with a constant crosshead displacement speed of 5 mm/min. The tensile properties were evaluated by averaging the value of five specimens under the same welding condition. An extensometer with a gauge length of 65 mm was used to measure the elongation during the tensile tests. After welding, optical microscopy was used to characterize the macrostructure and microstructure of the welded samples. Before the microstructure and microhardness studies metallographic specimens were cut from the weld cross-section, grounding and polishing processes were carried out, and then samples etched with 3% nital solution for 10-15 seconds. Vickers microhardness measurements were performed on the metallographic samples using a DUROLINE-M microhardness tester with a 100 gram load with a holding time of 10 seconds. Microhardness measurements were done from the first welding pass to see the effect of the final thermal cycle. The hardness values were measured spacing of 100 μm along the center of the first pass.

Table 1. Chemical properties of DP600 and DP1000 steels

Steel	C	Mn	Si	Cu+Cr+Ni	Cr
DP600	0.12	1.40	0.5	1.3	-
DP1000	0.16	1.89	0.26	-	0.44

Table 2. Mechanical properties of DP600 and DP1000 steels

Steel	Yield Strength (MPa)	Tensile Strength (MPa)	Elongation (%)
DP600	370	630	24
DP1000	660	1020	13.5

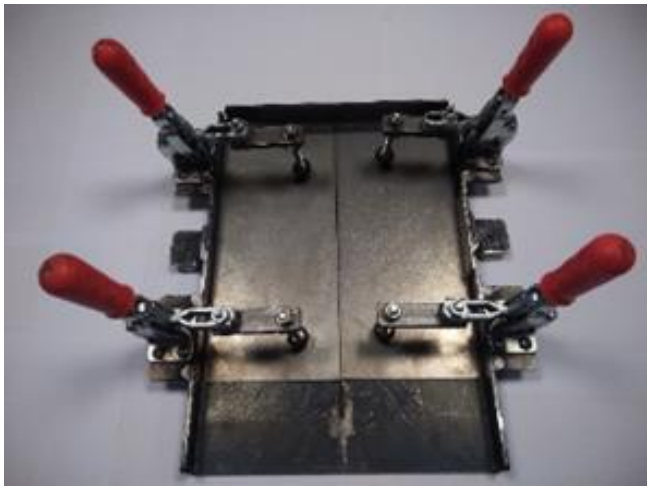

Figure 1. The fixture used in the welding operations

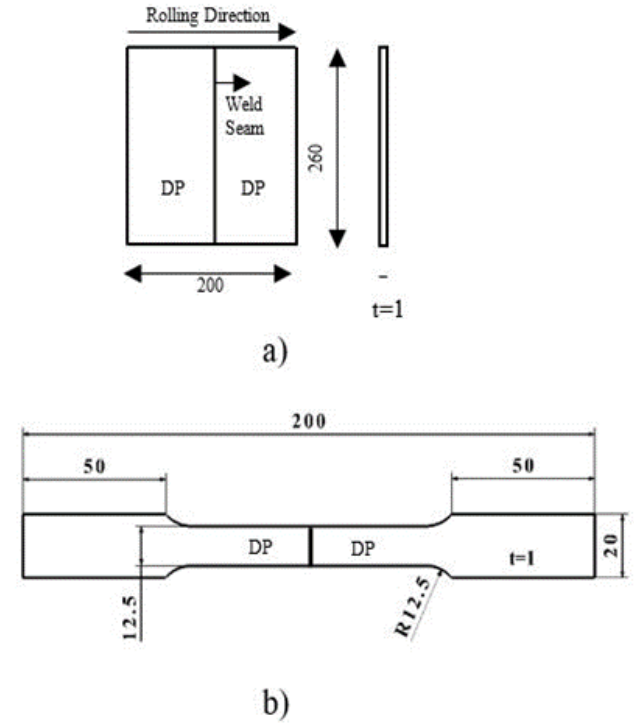

Figure 2. a) Schematic illustration of laser welded DP steel sheets; b) Dimensions of the tensile test specimens

Table 3. Welding parameters used in this study

Charge	Pulse Duration Time	Pulse Frequency	Focal Spot Diameter	Welding Speed
%	ms	Hz	mm	mm/s
65	5	5	1.4	4

3. RESULTS and DISCUSSIONS

To determine the quality of the double-sided laser welded joints, the tensile strength of the joints were experimentally conducted using tensile tests. The tensile test results exhibited that the weld combination significantly affected the tensile performance of double-sided laser welded DP600-DP600, DP600-DP1000 and DP1000-DP1000 steel sheet joints at the same welding parameters (Tab. 4).

The tensile strength of Nd:YAG laser welded DP600-DP600, DP600-DP1000 and DP1000-DP1000 steel sheets are shown in Fig. 3. The highest weld strength in these joints (880 MPa) was observed in DP1000-DP1000 joint. The lowest weld strength (586.5 MPa) was found in DP600-DP1000 joints. On the other hand, the effect of welding combination on the elongation of the double-sided laser welded joints can also be seen in Fig. 4. The highest elongation in these joints (29.12%) was for DP600-DP600 joint. And, the lowest elongation (8.82%) was for DP1000-DP1000 joint. These elongation values are quite enough for the automobile industry.

Table 4. Tensile strength and elongation of the laser welded joints (average values)

Weld Combination	Tensile Strength (MPa)	Elongation (%)
DP600-DP600	610.6	29.12
DP600-DP1000	586.5	15.46
DP1000-DP1000	880	8.82

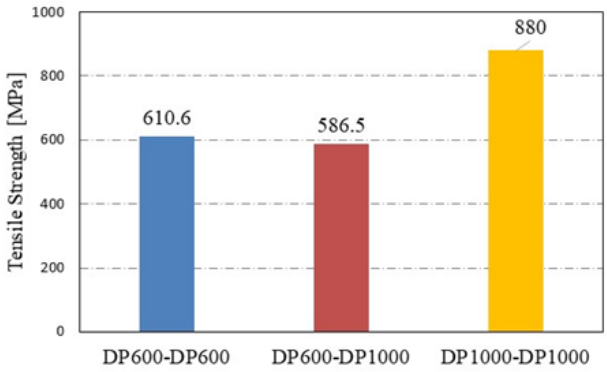

Figure 3. Tensile strength of Nd:YAG laser welded DP600-DP600, DP600-DP1000 and DP1000-DP1000 steel sheets

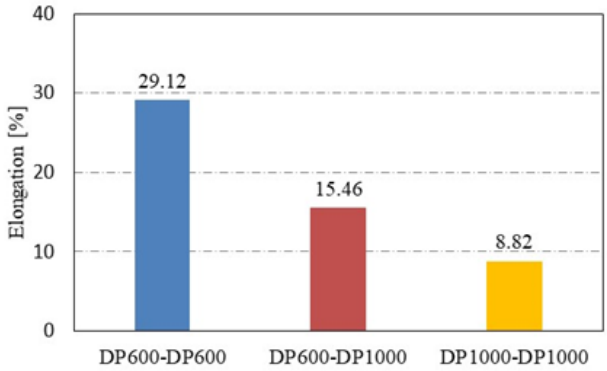

Figure 4. Elongation of Nd:YAG laser welded DP600-DP600, DP600-DP1000 and DP1000-DP1000 steel sheets

Fig. 5, Fig. 6 and Fig. 7 show the microhardness measurement results of the samples produced with DP600-DP600, DP600-DP1000 and DP1000-DP1000 joints, respectively. Measurements were done at 100 µm intervals along a line, starting from the center of the fusion zone until reaching the BM for similar welds. Also, dissimilar weld microhardness measurements were done from DP600 BM to DP1000 BM along a line with 100 µm intervals. Different hardness values were measured in the fusion zone, HAZ and BM regions along the line. The highest hardness values were obtained in the fusion zone at three different welding combination (Fig. 5, Fig. 6 and Fig. 7). The effective martensite

formation in the fusion zone is the reason why the highest hardness value obtained in this region. The increase in hardness as it moves away from the weld center in the fusion zones is due to the fine martensitic structures obtained as a result of relatively faster cooling. In three different samples, similarly narrow HAZ regions were observed. The width of the HAZ regions is roughly 300 µm. The hardness of these regions falls down from the fusion zone to the BM. This hardness drop is associated with a small amount of ferrite and tempered martensite near the BM. Furthermore, the tempering of the BM in a narrow area between the HAZ and the BM on the DP1000 sides caused significantly softening with the formation of ferrite and iron carbide (Fig.6, Fig.7).

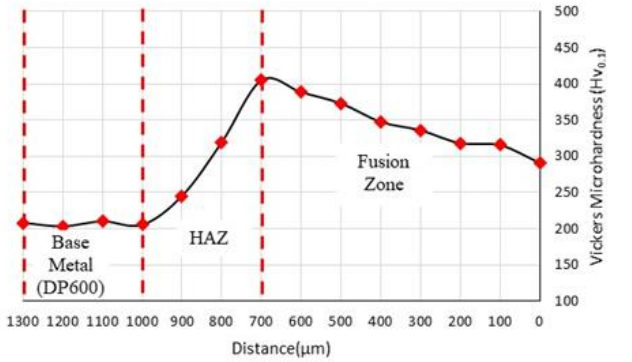

Figure 5. Microhardness variation of the weld zone in the DP600-DP600 sample

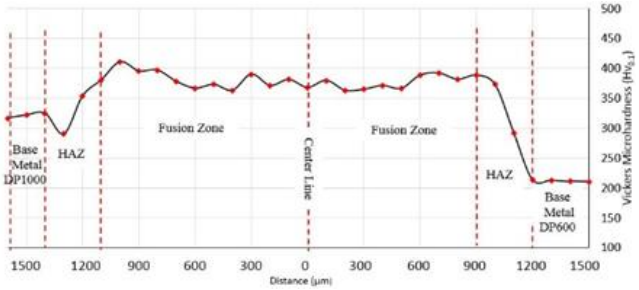

Figure 6. Microhardness variation of the weld zone in the DP600-DP1000 sample

Macro images of similar and dissimilar welded samples were shown in Fig 8. In Fig. 8a,b,c there were small black holes in the centre of weld zone because of insufficient weld penetration depth. Various regions from the weld zone were selected for microstructure examinations. And, X shape joint image was seen in all double-sided welded samples.

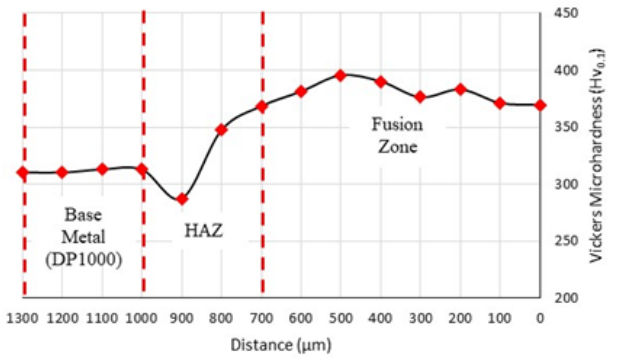

Figure 7. Microhardness variation of the weld zone in the DP1000-DP1000 sample

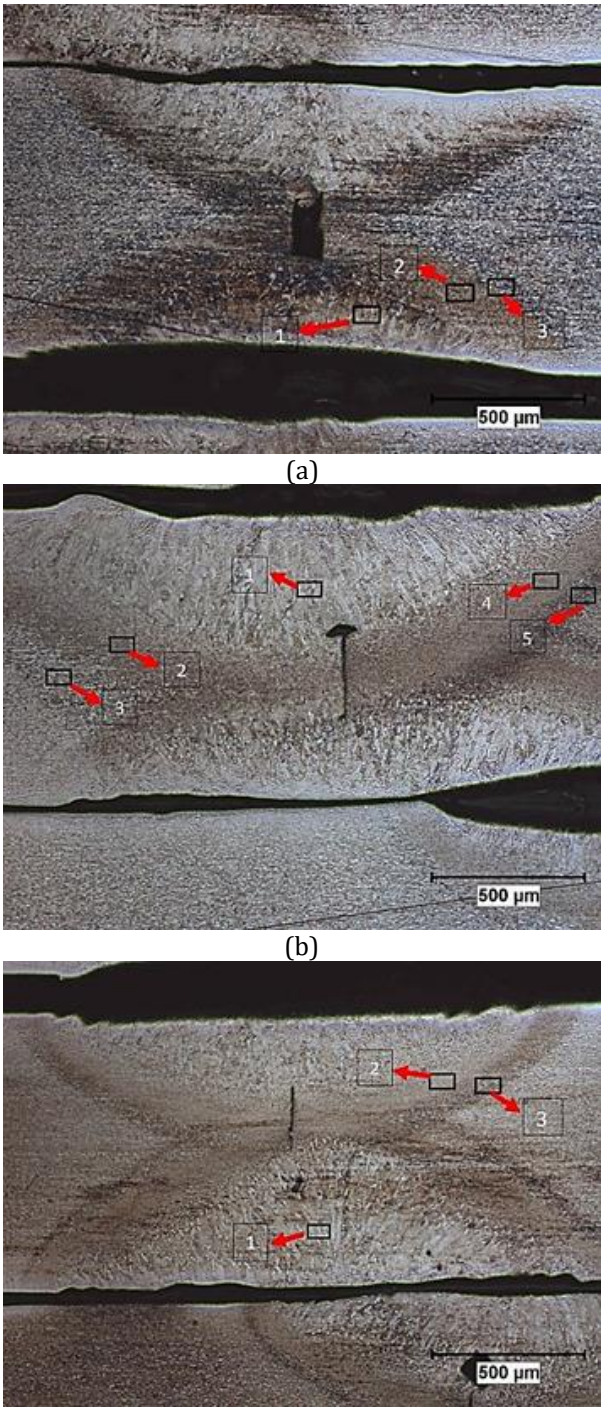

(a)

(b)

(c)

Figure 8. Macro images of the welded samples a) DP600-DP600, b) DP600-DP1000, c) DP1000-DP1000

Images of marked regions for DP600-DP600 joint in Fig. 8a were showed in Fig. 9. In Fig. 8 1st, 2nd and 3rd regions show fusion zone, HAZ and intersection of HAZ and BM, respectively. In the 1st region, melting was achieved as a result of heat input and then as a result of rapid cooling which is characteristic of laser welding, martensite and some bainite occurred (Fig 9a). The 2nd region contains the phases of bainite and tempered martensite, and some martensite near fusion zone (Fig 9b). And, the 3rd region has predominantly BM microstructure properties and there is a small amount of bainite and tempered martensite near HAZ in this region (Fig 9c).

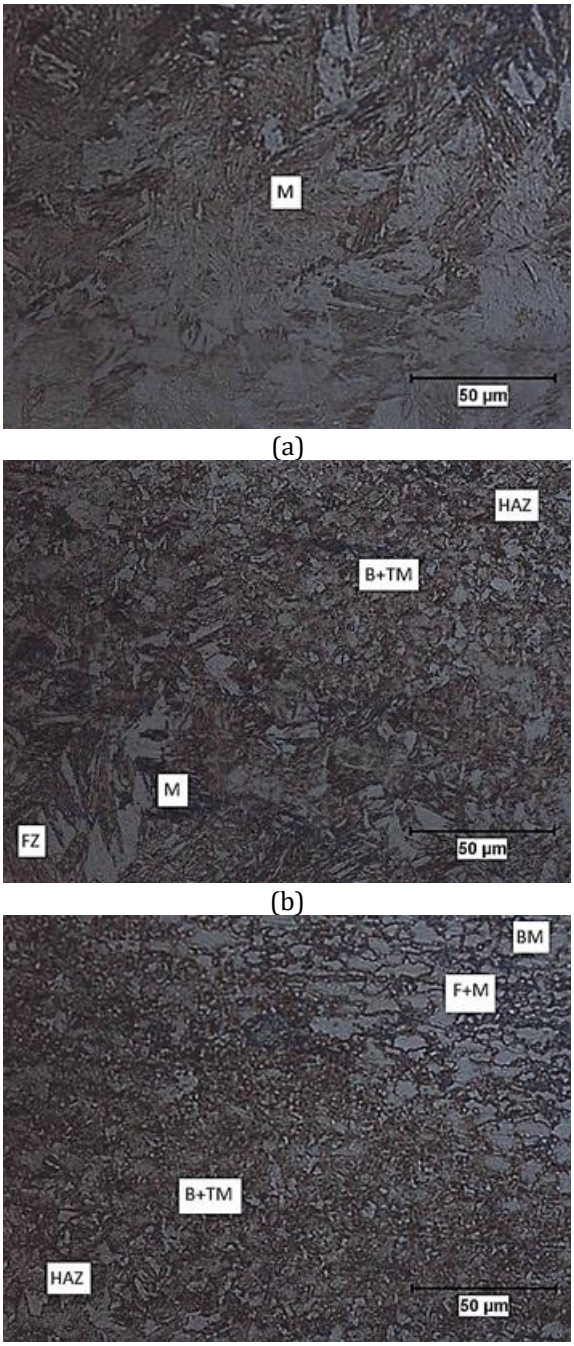

Figure 9. The microstructures of Nd:YAG laser welded DP600-DP600 joints a) Fusion zone b) HAZ c) Transition from HAZ to BM (F:Ferrite, M:Martensite, B:Bainite, TM: Tempered Martensite).

Images of marked regions for DP600-DP1000 joint in Fig. 8b were showed in Fig. 10. In Fig. 8 1st, 2nd, 3rd, 4th and 5th regions show fusion zone, HAZ on DP600 side, the intersection of HAZ and BM on DP600 side, HAZ on DP1000 side and the intersection of HAZ and BM on DP1000 side, respectively. The 1st region consists entirely of lath martensite (Fig. 10a). The 2nd region is composed of bainite and tempered martensite (Fig 10b). The 3rd region has highly BM microstructural properties. Also, near HAZ on DP600 side, the tempered martensite and bainite are observed (Fig. 10c). The 4th region consists of tempered martensite, retained austenite and bainite mixture (Fig 10d). The 5th region, which is softened zone, contains tempered martensite, bainite, ferrite and iron carbides (Fig 10e).

Images of marked regions for DP1000-DP1000 joint in Fig. 8c were showed in Fig. 11. In Fig. 11 1st region shows the fusion zone, 2nd region HAZ and 3rd region intersection of HAZ and BM. In the 1st region, martensite was formed completely and ıts thought there can be a little amount of retained austenite (Fig. 11a). The 2nd region is in the HAZ, which consists of martensite, bainite, retained austenite and tempered martensite (Fig 11a). The 3rd region is in the intersection of HAZ and BM, which consists of tempered martensite, bainite and highly include BM phases (Ferrite+Martensite) (Fig 11c).

4. CONCLUSION

In this study, the effects of weld combination on microstructure and mechanical properties of DP600-DP600, DP600-DP1000 and DP1000-DP1000 steel sheets welded with Nd: YAG laser device were investigated. The results obtained in this study are summarized as follows:

- In similar welds, DP600-DP600 weld strength approximately equal to BM strength (97% of BM), but DP1000-DP1000 weld strength lower than the DP1000 BM strength (86% of BM). The reason for lower tensile strength of DP1000-DP1000 weld is a big amount of hard martensite formation.
- In dissimilar weld (DP600-DP1000) tensile strength approximately equal to DP600 BM strength (93% of DP600 BM).
- The hardness values obtained in the fusion zone are in complete harmony with the fusion zone microstructures. Hard lath martensitic phases have emerged in the fusion zones. This is the reason why the hardness values of the fusion zone are considerably higher than the BM.
- In the DP 1000 steel, a tempered BM structure (tempered martensite and ferrite) occurs between HAZ and the BM. As a result, lower hardness values than the BM were measured.

ACKNOWLEDMENT

This study is supported by the Scientific Research Fund (BAP) of Uludag University (Project Contract No. HDP (MH)-2017/47).

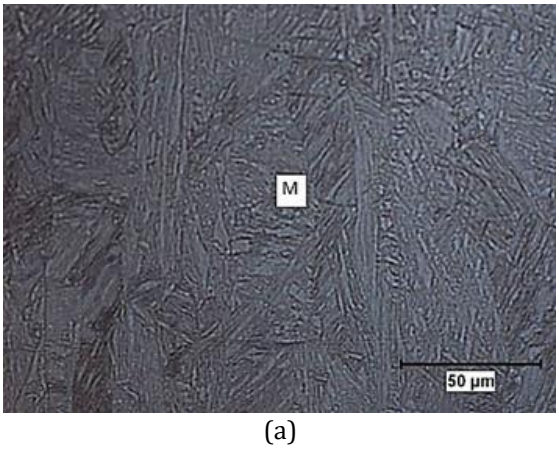

(a)

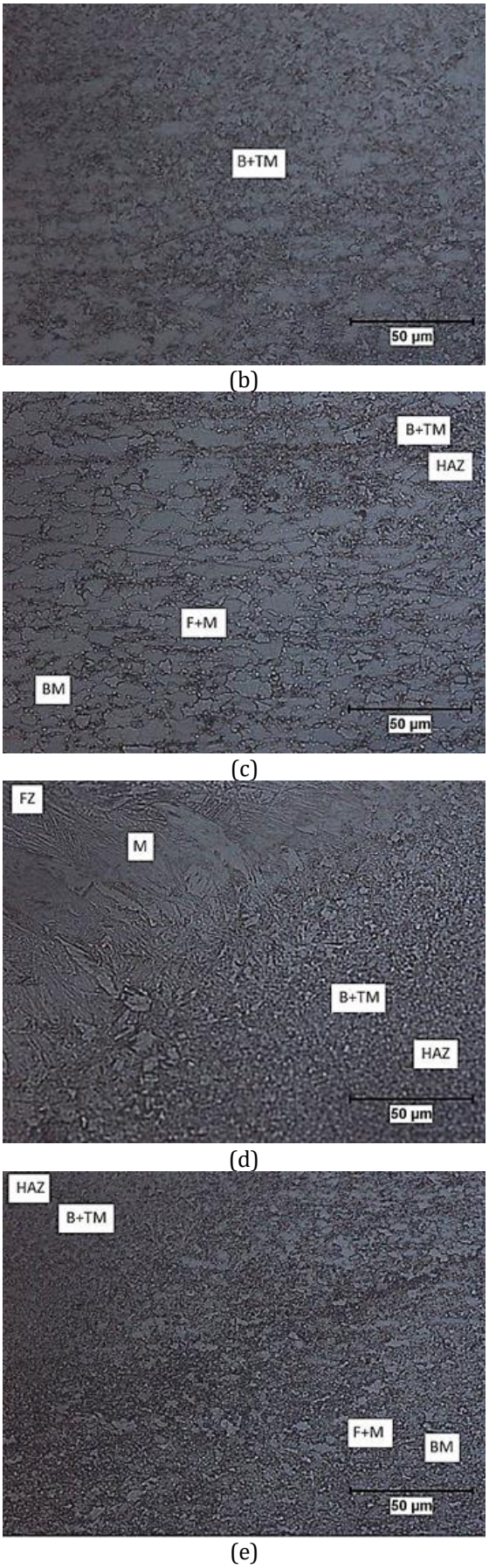

Figure 10. The microstructures of Nd:YAG laser welded DP600-DP1000 joints a) Fusion Zone b) HAZ on DP600 side c) Transition from HAZ to BM on DP600 side d) HAZ on DP1000 side e) Transition from HAZ to BM on DP1000 side (F:Ferrite, M:Martensite, B:Bainite, TM:Tempered Martensite).

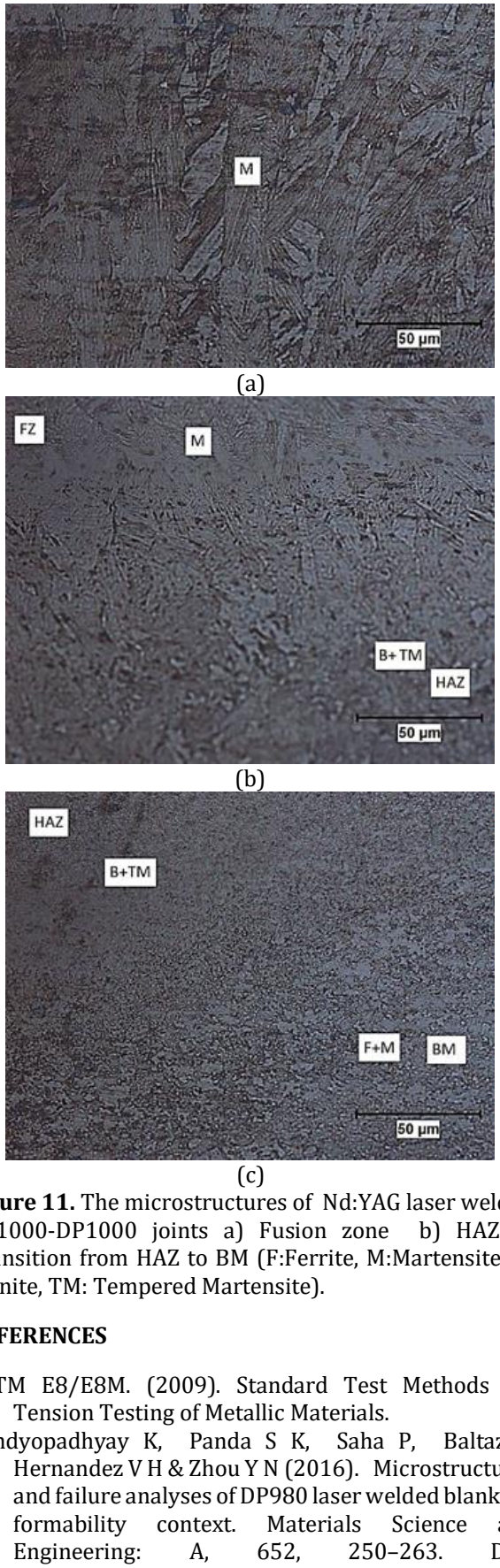

Figure 11. The microstructures of Nd:YAG laser welded DP1000-DP1000 joints a) Fusion zone b) HAZ c) Transition from HAZ to BM (F:Ferrite, M:Martensite, B: Bainite, TM: Tempered Martensite).

REFERENCES

ASTM E8/E8M. (2009). Standard Test Methods for Tension Testing of Metallic Materials.

Bandyopadhyay K, Panda S K, Saha P, Baltazar-Hernandez V H & Zhou Y N (2016). Microstructures and failure analyses of DP980 laser welded blanks in formability context. Materials Science and Engineering: A, 652, 250–263. DOI: 10.1016/j.msea.2015.11.091

Di H, Sun Q, Wang X & Li J (2017) Microstructure and properties in dissimilar/similar weld joints between DP780 and DP980 steels processed by fiber laser welding. Journal of Materials Science & Technology,

33(12), 1561-1571. DOI: 10.1016/j.jmst.2017.09.001

Dong D, Liu Y, Yang Y, Li J, Ma M & Jiang T (2014) Microstructure and dynamic tensile behavior of DP600 dual phase steel joint by laser welding. Materials Science & Engineering: A, 594, 17–25. DOI: 10.1016/j.msea.2013.11.047

Fernandes F A O, Oliveira D F & Pereira A B (2017). Optimal parameters for laser welding of advanced high-strength steels used in the automotive industry. Procedia Manufacturing, 13, 219–226. DOI: 10.1016/j.promfg.2017.09.052

Hazratinezhad M, Mostafa Arab N B, Sufizadeh A R & Torkamany M J (2012) Mechanical and metallurgical properties of pulsed neodymium-doped yttrium aluminum garnet laser welding of dual phase steels. Materials and Design, 33, 83–87. DOI: 10.1016/j.matdes.2011.06.070

Hekmatjou H & Naffakh-Moosavy H (2018). Hot cracking in pulsed Nd:YAG laser welding of AA5456. Optics and Laser Technology, 103, 22–32. DOI: 10.1016/j.optlastec.2018.01.020

Liu Y, Dong D, Wang L, Chu X, Wang P & Jin M (2015). Strain rate dependent deformation and failure behavior of laser welded DP780 steel joint under dynamic tensile loading. Materials Science and Engineering: A, 627, 296–305. DOI: 10.1016/j.msea.2014.12.103

Mohammadpour M, Yazdian N, Yang G, Wang H P, Carlson B & Kovacevic, R (2018). Effect of dual laser beam on dissimilar welding-brazing of aluminum to galvanized steel. Optics and Laser Technology, 98, 214–228. DOI: 10.1016/j.optlastec.2017.07.035

Parkes D, Xu W, Westerbaan D, Nayak S S, Zhou Y, Goodwin F, Bhole S & Chen D L (2013). Microstructure and fatigue properties of fiber laser welded dissimilar joints between high strength low alloy and dual-phase steels. Materials and Design, 51, 665–675. DOI: 10.1016/j.matdes.2013.04.076

Saha D C, Westerbaan D, Nayak S S, Biro E, Gerlich A P & Zhou Y (2014) Microstructure-properties correlation in fiber laser welding of dual-phase and HSLA steels. Materials Science and Engineering: A, 607, 445–453. DOI: 10.1016/j.msea.2014.04.034

Sharma R S & Molian P (2011) Weldability of advanced high strength steels using an Yb: YAG disk laser. Journal of Materials Processing Technology, 211(11), 1888–1897. DOI: 10.1016/j.jmatprotec.2011.06.009

Sun Q, Di H S, Li J C & Wang X N (2016). Effect of pulse frequency on microstructure and properties of welded joints for dual phase steel by pulsed laser welding. Materials and Design, 105, 201–211. DOI: 10.1016/j.matdes.2016.05.071

Wang J, Yang L, Sun M, Liu T & Li H (2016) Effect of energy input on the microstructure and properties of butt joints in DP1000 steel laser welding. Materials and Design, 90, 642–649. DOI: 10.1016/j.matdes.2015.11.006

Węglowski M S, Kwieciński K, Krasnowski K & Jachym R (2009). Characteristics of Nd:YAG Laser Welded Joints of Dual Phase Steel. Archives of Civil and Mechanical Engineering, 9(4), 85–97. DOI: 10.1016/S1644-9665(12)60072-7

Xia M, Biro E, Tian Z L & Zhou Y N (2008) Effects of heat input and martensite on HAZ softening in laser welding of dual phase steels. ISIJ International, 48(6), 809–814. DOI: 10.2355/isijinternational.48.809

Yuce C, Tutar M, Karpat F, Yavuz N & Tekin G (2017). The effect of process parameters on the microstructure and mechanical performance of fiber laser-welded AA5182 aluminium alloys. Strojniski Vestnik/Journal of Mechanical Engineering, 63, 510–518.

Turkish Journal of Engineering

https://dergipark.org.tr/en/pub/tuje

e-ISSN 2548-0960

An investigation on the geomechanical properties of fiber reinforced cohesive soils

Özgür Lütfi Ertuğrul [*1], **Fatma Dülger Canogullari** [2]

[1]*Mersin University, Faculty of Engineering, Department of Civil Engineering, Mersin, Turkey*
[2]*Toros University, Faculty of Engineering, Department of Civil Engineering, Mersin, Turkey*

Keywords
Fiber
Soil improvemnt
Cohesive soil

ABSTRACT

In recent years, the use of natural and synthetic fibers in soil improvement has become widespread in soil mechanics applications. Easy to use and low cost fibers have been the subject of many geotechnical researches in recent years. In this study, results of previous mechanical experiments performed on fiber-cohesive soil mixtures were reviewed in a systematical approach. Based on the data derived from the experimental studies available in the literature, it has been observed that various soil properties including soil strength have improved with increasing density of the fibers up to a certain level. The percentage of added fiber has a significant effect on improving soil properties. Based on statistical analysis, simple correlation relationships were suggested based on the investigated test database.

1. INTRODUCTION

Many soil improvement methods are practiced today for improving the properties of soils. The choice of suitable method depends upon the type of soil, material available, durability and sustainability. Out of these various materials, natural or synthetic fibers can also be used for soil improvement (Patil and Pusadkar 2019).

The first documented engineering use of natural fibers in a road construction was reported in 1926 by the South Carolina Highways Department, undertaking a series of field tests on the use of woven cotton fabrics as a simple type of geotextile to reduce cracking and raveling failure of roads. From that time, various different materials were used as soil improvement technique. In recent years, soil reinforcement with synthetic and natural fibers are gaining importance since the demand for ground improvement is increasing due to growing construction sector. The use of natural fibers, such as bamboo, jute and coir as soil reinforcing materials has been prevalent for a long time in several South Asian nations. Synthetic fibers such as polypropylene, polyester, polyethylene and glass fibers have also been used for soil reinforcement (Mali and Singh 2014).

Since the fibers have higher tensile strengths than natural cohesive soils, fiber-ground mixtures can achieve much greater shear strength values than fiber-free soils. Fibers are thought to be efficient, especially on soils close to the surface where effective tensile and shear strength is low due to smaller confining stress.

2. GENERAL PROPERTIES OF FIBERS

Fibers, which have been used for soil reinforcement, have many advantages as listed below (Darvishi 2014):

- Mixing fibers with the soil is as easy as mixing other materials such as cement and lime used for stabilization.
- If homogeneous mixing is achieved, the fibers provide isotropic strength in the soil.
- Environment conditions have relatively low impact on fiber reinforced soils.

With the advances in chemistry, synthetic fibers are being produced in large quantities and becoming commercially available day by day. Synthetic fibers can be produced according to required specifications. For example, geometry of synthetic fibers can be controlled, shape of fibers and surface conditions can be changed in order to improve friction properties of fibers. Most synthetic fibers do not biodegrade when exposed to difficult environmental effects such as UV light, moisture and temperature (Krenchel 1973).

* **Corresponding Author**

*(ertugrul@mersin.edu.tr) ORCID ID 0000 – 0002 – 1270 – 3649
(fatma.dulger@toros.edu.tr) ORCID ID 0000 – 0002 – 0927 – 7132

Cite this article

Ertugrul O L & CAnogulları F D (2021). An investigation on the geomechanical properties of fiber reinforced cohesive soils. Turkish Journal of Engineering, 5(1), 15-19.

Research Article / DOI: 10.31127/tuje.651222

Received: 26/11/2019; Accepted: 17/01/2020

2.1. General Properties of Polypropylene Fibers

Polypropylene is a 100% synthetic fiber, which is transformed from 85% propylene. The monomer of polypropylene is propylene.

Polypropylene fibers are low cost products having good impact resistance. They have low friction coefficients and provide very good electrical insulation. Besides, polypropylene fibers have good chemical resistance. Although polypropylene fibers melt at 160-170°C, they maintain most of their mechanical properties up to that temperatures. Polypropylene fibers are resistant to strong acids and bases. They retain their rigidity even after many bends. On the other side, polypropylene has some disadvantages such as low UV resistance, high thermal expansion, low weather resistance and oxidation susceptibility. The physical properties of polypropylene fibers are shown in Table 1.

Table 1. Physical properties of polypropylene fibers

Property	Value
Tensile strength (gf/den)	3.5 to 5.5
Elongation (%)	40 to 100
Abrasion resistance	Good
Moisture absorption (%)	0 to 0.05
Softening point (°C)	140
Melting point (°C)	165
Relative density	0.91
Thermal conductivity (W/mK)	6.0
Electric insulation	Excellent

3. LITERATURE REVIEW

Nataraj and McManis (1997) investigated the strength and deformation characteristics of soils reinforced with randomly distributed fibrillated fibers. The laboratory tests were conducted on a cohesive soil. The main properties of the clay tested in this study are shown in Table 2.

Table 1. Properties of the clay

Liquid limit (%)	Plastic limit (%)	Plasticity index (%)	C (kPa)	ϕ (°)	w_{opt} (%)
44	18	26	84	19.5	17.9

The fibers used in this study are 25 mm long and are produced by American Synthetic Industry Corporation. In many studies, the diameter, strength or type of fiber was considered, but in this study, same type of fibers were used throughout the experimental study. Fibers were mixed into the soil by hand or by mechanical mixer. In this study, the mixture of soil and fibers was taken to a large metal pan and uniformly mixed by adding a certain amount of water. Fiber density was examined as 0.1%, 0.2% and 0.3% of dry soil weight.

In the compaction tests, the relationship between dry unit weight and moisture density was investigated by comparing fiber reinforced and unreinforced soils. The increase in fiber density increased the dry unit volume weight slightly and decreased the moisture density. The clay specimens were compacted with a 178 N compaction force in 3 layers using 30 blows per layer.

Clay specimens were prepared at maximum dry unit weight and optimum moisture ratio and they were subjected to unconfined compression tests. Three different size specimens were tested (33mm×72 mm, 70 mm ×140 mm, and 100 mm × 117 mm).

According to the test results, the strength of all reinforced clay specimens increases with increasing moisture content. The strength of clay samples with a fiber content of 0.2% and 0.3% is significantly higher than that of a sample with a fiber content of 0.1%.

Clay specimens with and without fibers were subjected to direct shear tests in 64 mm and 100 mm cutting boxes. The specimens were prepared at maximum dry unit weight and optimum moisture content. The clay specimens which have 0.3% fiber content reached higher shear stress values than the other specimens. California Bearing Ratio tests were conducted on reinforced and unreinforced clay specimens at maximum dry densities and moisture contents (ASTM D 698).

The CBR value for the unreinforced clay specimen increased from 8.44 to approximately 12.6 for specimens with a 0.3% fiber content.

Puppala and Musenda (2000) conducted unconfined compressive tests using Irving (PI = 55) and San Antonio (PI = 46) clays. The results indicated increased strength and ductility of the soil with increasing fiber content. The effect of fiber length was also evaluated and it was found that as the length of the fibers was increased from 2.54 mm to 5.08 inches, the strength and axial strain at failure also increased.

The shear strength of the fiber-reinforced sand at large shear displacement has been investigated by Heineck et al. (2005), who reported that although fiber-reinforced soil did not outperform the unreinforced sand in terms of initial stiffness, its shear strength was superior to that of the unreinforced soil with no loss even at large shear displacements of 250 mm.

Abdi et al. (2008) studied the consolidation settlement and swelling characteristics of clays with inclusion of 5, 10, and 15 mm polypropylene fibers at fiber content of 1%, 2%, 4% and 8% by weight of dry soil. They concluded that addition of randomly distributed polypropylene fibers resulted in reducing the consolidation settlement of the clay soil. Length of fibers had an insignificant effect on this soil characteristic, whereas fiber contents proved more influential and effective. Inclusion of polypropylene fibers to the clay soil resulted in reducing the amount of swelling after unloading. The effect was proportional to the fiber content. But at constant fiber contents, the amount of swelling was not significantly affected by increasing fiber length.

Jiang et al. (2010) performed tests on a cylindrical clayey soil sample of 61.8 mm diameter. Fibers of 0.02-0.05 mm diameter and 15, 20 and 25 mm length were mixed at 0%-0.4% densities and a series of shear strength experiments were performed. At the end of the experiments, it was observed that the cohesion value and the internal friction angle increased with increasing fiber density and length.

Sravya and Suresh (2016) observed that the effect of synthetic-fibers in the restricted swelling of expansive soils. One-dimensional swell-consolidation tests were carried out to determine the behavior changes in the soil samples. It is noticed that increasing fiber content causes

a decrease in swelling pressure while increasing the unconfined compressive strength (UCS) and CBR values.

Mirzababaei et al. (2018) carried out a series of multi-stage drained reverse direct shear tests. The soft clay samples reinforced with 0.25% and 0.50% polypropylene fibers of 6 mm, 10 mm and 19 mm in length. Results showed an increase of the shear strength with the increase of fiber content and length.

Ma et al. (2018) studied the fiber reinforced clay in different fiber content and different confining pressure. Laboratory triaxial tests were carried out to investigate the reinforcement mechanism. The test results showed that the shear strength of fiber reinforced clay was greater than that of pure clay.

Soltani et al. (2018) reported the effect of two kind of tape-shaped fibers. In this investigation, two different fiber widths (2.5 mm, and 7 mm) were used as the reinforcement for the expansive soil. The fiber contents used this study were 0.5%, 1%, and 1.5%. Each fiber type has two lengths/aspect ratios (15/2.5 and 30/2.5) for fiber-A type, and (15/7 and 30/7) for fiber-B type. In case of constant width for a given fiber type it was observed that the direct function of improvement of expansive soil is fiber content and length.

Tong et al. (2019) investigated the addition of fibers improves the shear strength of the reinforced clay and effectively improves the deformation resistance of the fiber-reinforced clay. The addition of fibers increased the internal friction angle and cohesion of the clay.

Benziane et al. (2019) carried out a series of direct shear box tests to compare unreinforced and reinforced soil with different contents of fibers. The experimental results showed that the mechanical characteristics was improved with the addition of polypropylene fibers.

Hussein and Ali (2019) studied the effect of adding polypropylene fiber on the behavior of expansive soil. In this study Unconfined Compression Test, One-Dimensional Consolidation Test, Swelling Test, Sieve Analysis and Cycle Swell Shrink Test were carried out and test results were saved. The results showed that the increase in percentage of polypropylene fiber (PPF) led to decrease the swelling and to increase the unconfined compression strength.

Test data obtained from many experimental studies available in the literature were compiled in Table 3 and graphs were presented with a series of regression equations (Ertugrul and Canoğulları 2019). In the regression equations LL denotes the liquid limit of the soil and d_f denotes the fiber density in percent.

Considering the data for the effect of fiber density on the cohesion, following regression model was fitted:

$$c = \alpha + \beta^*(LL/PL) + \gamma^*(d_f)$$

Coefficients (with 95% confidence bounds):

α= 115.3 (66.2, 164.4)

β = -17.45 (-39.61, 4.712)

γ= 18.93 (11.07, 26.8)

On behalf of the goodness of fit, R-square value is found as 0.9043.

Considering the data for the effect of fiber density on the internal friction angle of soil, following regression model was fitted:

$$\Phi = \zeta + \eta^*(LL/PL) + \psi^*(d_f)$$

Coefficients (with 95% confidence bounds):

ζ = 41.57 (36.85, 46.3)

η = -6.088 (-8.219, -3.957)

ψ = 0.3998 (-0.3562, 1.156)

On behalf of the goodness of fit, R-square value is found as 0.8949.

Table 3. A summary of previous test results

LL/PL ratio	Fiber density, d_f (%)	c (kPa)	ϕ(°)
36.4/18.6	0	75,5	27,5
(Tang et al. 2007)	0.05	95,9	28,2
	0.15	103	29,7
	0.25	115,6	31,6
44/18	0	84	19,5
(Nataraj and McManis 1997)	0.3	122,5	32
50/21	0	40	26
(Pradhan et al 2012)	0.1	90	30.1
	0.2	90	40.9
	0.3	95	44.1
	0.4	96	44.4
	0.5	50	52
65/27.6	0	97	27.3
(Naeini and Sadjadi 2008)	1	105	34.2
	2	109.9	36.3
	3	103.7	37.1
	4	100.6	37.3
72/29.9	0	160.9	20.3
(Naeini and Sadjadi 2008)	1	163.2	25.6
	2	168	27.4
	3	163	28.1
	4	149	28.5
78.58/31.5	0	185	17.4
(Naeini and Sadjadi 2008)	1	190.4	22.5
	2	194	24
	3	190	24.7
	4	188	25.3
52.9/27.5	0	59	5.5
(Maheshwari 2011)	0.2	70	18.65
	0.5	76	26.58
	1	64	23.65
	1.5	62	13.69
26.93/20.19	0	49.16	34.07
(Bo et al. 2013)	0.1	94.01	35.71
	0.2	138.29	36.36
	0.3	228.35	35.95
74/27	0	6.1	25
(Mirzababaei 2018)	0.25	33	22
	0.5	43	25.7
32.6/16.8	0.2	380	32
(Wei et al. 2018)	0.25	368	33
	0.3	350	33
57.1/19.7	0	64	21
(Wang et al. 2019)	0.4	72.32	24.57
74/27	0	6.1	25
(Mirzababaei 2018)	0.25	28.7	26.9
	0.5	41.1	24.1
38.94/20.43	0	34.9	25.5
(Ma et al. 2018)	0.2	35.96	25.9
	0.4	41.26	28.2
	0.6	44.81	30
	0.8	48.75	27.2
	1.0	45.72	26.5

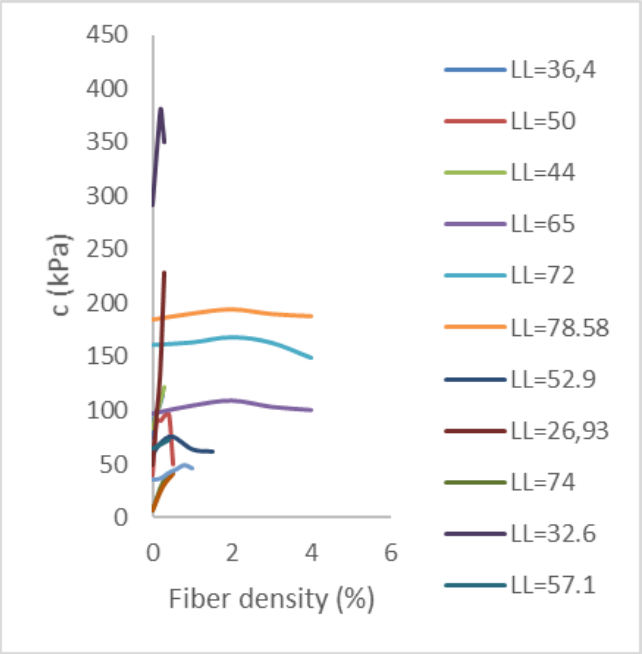

Figure 1. Effect of soil – fiber density on cohesion

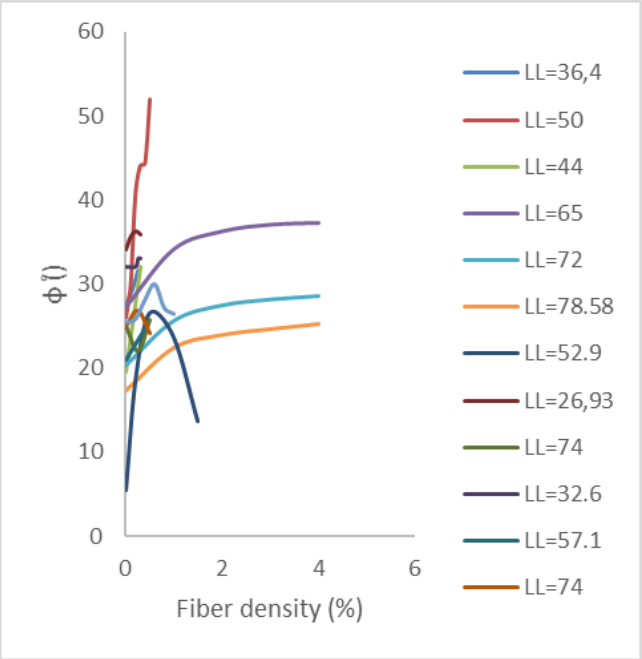

Figure 2. Effect of the soil – fiber density on the friction angle

4. CONCLUSION

Soil improvement techniques are used to improve the engineering properties of soils. These techniques vary by the application methods and soil types that can be improved. The addition of geosynthetic materials (fibers, geomembranes and geotextiles) is a new improvement technique that ensures uniformity in the soil during construction. In recent years, the use of fiber in soil improvement has become widespread. Easy to use and low cost fibers have been the subject of many geotechnical researches. Since the fibers have higher tensile strengths than natural cohesive soils, fiber-ground mixtures can achieve much greater shear strength values than fiber-free soils. The over-all effects of random fiber inclusion on clays observed, suggests potential applications of fiber reinforced soils in shallow foundations, embankments over soft soils, liners, covers and other earthworks that may suffer excessive deformations.

Clays are known for their high compressibility and low shear strength. Previous studies have mainly evaluated the effects of additives such as sand, cement and lime on these properties of clay and the results have shown that soil properties have improved.

In this study, results of experiments on fiber - added cohesive soils are investigated. Test data obtained from many previous studies available in the literature were compiled within the scope of this study and graphs were presented with a series of regression equations.

According to the performed analyses, it was been observed that the shear strength of the reinforced soils increases with fiber content , the consolidation settlement of clayey soils mixed with polypropylene fibers were decreased considerably. Fiber length has a small effect on this soil property, while fiber density has been observed to be quite effective on the mechanical and consolidation characteristics of the untreated soil.

REFERENCES

Abdi M R, Parsapajouh A & Arjomand M A (2008). Effects of Random Fiber Inclusion on Consolidation, Hydraulic Conductivity, Swelling, Shrinkage Limit and Desiccation Cracking of Clays. International Journal of Civil Engineering, 6(4), 284-292.

ASTM D 698 (2000) Fundamental principles of soil compaction. American Society for Testing and Materials, West Conshohocken.

Benziane M M, Della N, Denine S, Sert S & Nouri S (2019). Effect of randomly distributed polypropylene fiber reinforcement on the shear behavior of sandy soil. Studia Geotechnica et Mechanica, 41(3), 151-159. DOI: 10.2478/sgem-2019-0014

Bo L, Linli J, Ningyu Z & Sinong L (2013). Centrifugal and numerical analysis of geosynthetic-reinforced soil embankments , Paris, 2429-2432.

Darvishi A (2014). Behavior of Fiber Reinforced Sand Under Static Load. MSc Thesis, İstanbul Technical University, Istanbul, Turkey.

Ertugrul O L & Canogullari D F (2019). An investigation on the geomechanical properties of fiber reinforced cohesive soils. 2nd Cilicia International Symposium on Engineering and Technology, Mersin, Turkey, 500-503.

Heineck K S, Coop M R & Consoli N C (2005). Effect of micro-reinforcement of soils from very small to large shear strains. Journal of Geotechnical and Geoenvironmental Engineering, 131(8) ,1024–1033, DOI:10.1061/(ASCE)1090-0241(2005)131:8(1024).

Hussein S A & Ali H A (2019). Stabilization of Expansive Soils Using Polypropylene Fiber. Civil Engineering Journal, 5(3), 624-635. DOI: 10.28991/cej-2019-03091274

Jiang H, Cai Y & Liu J (2010). Engineering properties of soils reinforced by short discrete polypropylene fiber. J Mater Civil Eng ASCE 22(12):1315.

Krenchel H (1973). Fiber reinforced brittle matrix materials. Proceedings of international symposium on fiber reinforced concrete, Ottawa.

Ma Q, Yang Y, Xiao H, Xing W (2018). Studying Shear Performance of Flax Fiber-Reinforced Clay by Triaxial Test. Advances in Civil Engineering. DOI: 10.1155/2018/1290572

Maheshwari K V, Desai A K & Solanki D H (2011). Performance of Fiber Reinforced Clayey Soil. Electronic Journal of Geotechnical Engineering 16:1067-1082.

Mali S & Singh B (2014). Strength Behaviour of Cohesive Soils Reinforced with Fibers. International Journal of Civil Engineering Research, 5(4), 353-360.

Mirzababaei M, Arulrajah A, Haque A, Nimbalkar S & Mohajerani A (2018). Effect of fiber reinforcement on shear strength and void ratio of soft clay. Geosynthetics International, 25(4), 471–480. DOI: 10.1680/jgein.18.00023

Naeini S A & Sadjadi S M (2008). Effect of Waste Polymer Materials on Shear Strength of Unsaturated Clays. Electronic Journal of Geotechnical Engineering, 13,1-12.

Nataraj M S & McManis K L (1997). Strength and Deformation Properties of Soil Reinforced With Fibrillated Fibers. Geosynthetics International, 4(1), 65-79. DOI: 10.1680/gein.4.0089

Patil L B & Pusadkar S S (2019). Natural Fibers as Geo-Reinforcement-A Review. International Journal of Innovations in Engineering and Science, 4(8), 119-123.

Pradhan P K, Kar R K & Naik A (2012). Effect of Random Inclusion of Polypropylene Fibers on Strength Characteristics of Cohesive Soil. Geotechnical and Geological Engineering, 30, 15–25. DOI 10.1007/s10706-011-9445-6

Puppala A & Musenda C (2000). Effects of Fiber Reinforcement on Strength and Volume Change in Expansive Soils. Transportation Research Record 1736, 00-0716.

Soltani Amin, An Deng & Abbas Taheri (2018). Swell–compression characteristics of a fiber–reinforced expansive soil. Geotextiles and Geomembranes 46.2 183-189.doi:10.1016/j.geotexmem.2017.11.009.

Sravya S & Suresh K (2016). Swell and Strength Characteristics of Expansive Soil Reinforced with Synthetic Fibers. i-Manager's Journal on Civil Engineering, 6(4). DOI:10.26634/jce.6.4.8236.

Tang C, Shi B, Gao W, Chen F & Cai Y (2007). Strength and mechanical behavior of short polypropylene fiber reinforced and cement stabilized clayey soil. Geotextiles and Geomembranes 25; 194–202.

Tong F, Ma Q & Xing W (2019). Improvement of Clayey Soils by Combined Bamboo Strip and Flax Fiber Reinforcement. Advances in Civil Engineering. DOI: 10.1155/2019/7274161

Wang Y, Guo P & Li X (2019). Behavior of Fiber-Reinforced and Lime-Stabilized Clayey Soil in Triaxial Tests. Applied Sciences, 9(5). DOI: 10.3390/app9050900

Wei L, Chai S X, Zhang H Y & Shi Q (2018). Mechanical Properties of Soil Reinforced with Both Lime and Four Kinds of Fiber. Construction and Building Materials, 172, 300-308. DOI: 10.1016/j.conbuildmat.2018.03.248

Turkish Journal of Engineering

https://dergipark.org.tr/en/pub/tuje

e-ISSN 2548-0960

Improved HYBRID intelligent controller design for MPPT of stand-alone PV System

Okkes Fatih Kececioglu[1], Ahmet Gani *[1], Mustafa Sekkeli [1]

[1]*Kahramanmaras Sutcu Imam University, Engineering and Architecture Faculty, Department of Electrical and Electronics Engineering, Kahramanmaraş, Turkey*

Keywords
Hybrid intelligent controller
MPPT
Stand-alone PV system

ABSTRACT

Photovoltaic (PV) systems have low power conversion efficiency, so maximum power point tracking (MPPT) control methods are utilized to maximize the efficiency of PV systems. The present study proposes an improved hybrid intelligent controller design for the MPPT of stand-alone PV system. The hybrid intelligent control structure is integrated into Angle of Incremental Conductance (AIC) method and Interval Type-2 Takagi-Sugeno-Kang Fuzzy Logic Controller (IT2-TSKFLC). The proposed hybrid intelligent controller offers a superior performance in terms of dealing with uncertainties of sudden changes under different environmental conditions. A simulation model is created in Matlab/Simulink using daily data from a real solar PV plant to evaluate the performance of the proposed hybrid intelligent controller. The simulation findings demonstrated that the proposed hybrid intelligent controller displays a highly stable and robust performance in terms of tracking maximum power point compared to a conventional AIC MPPT method against various uncertainties stemming from disturbing inputs such as solar irradiance and panel temperature variations.

1. INTRODUCTION

Solar energy is a clean, abundant and sustainable energy source which bears a great potential for energy needs in the future. Photovoltaic (PV) power generation has become very widespread around the world (Dogmus et al. 2017). However, PV power generation systems have three main drawbacks: high installation cost, low power conversion efficiency and high dependence on environmental conditions such as solar irradiance and temperature.

In general, a PV panel, power converter, and load can be found in a basic PV system. Power converter is the most crucial component of a PV system. In the existing literature, various power converter topologies are used for PV systems. A power converter controls the power flow from a PV panel to the load (Kececioglu et al. 2018). Buck, Boost and Buck-Boost converter, which is also known as conventional power DC-DC converters, are among the most widely used power converter topologies. Conventional DC-DC power converters offer a limited output voltage and power transfer efficiency because of parasitic elements in their circuit topology. Therefore, high voltage conversion gain DC-DC power converters eliminate this problem. Voltage lift technique overcomes parasitic elements for high voltage conversion gain DC-DC power converters. Luo converters provide several advantages such as a higher output voltage, power density, efficiency and a lower output voltage ripple (Luo 1997). In the present study, Modified Positive Output Luo Converter (MPOLC) with re-lift configuration is used to provide high voltage gain conversion.

Current-Voltage (I-V) and Power-Voltage (P-V) characteristic curves of a PV panel are non-linear and vary depending on environmental conditions. On these curves is an optimum power point called maximum power point (MPP) and thus the PV panel generates maximum output power at the MPP (Dixit et al. 2018). MPPT control methods enable PV systems to overcome high dependence on environmental conditions. In the existing literature, MPPT methods are divided into two categories as conventional and intelligent methods. While Hill-climbing (HC), perturb and observe (P&O), incremental conductance (IC) and angle of incremental conductance (AIC) are conventional MPPT methods, Artificial Neural Network (ANN) and Fuzzy Logic (FL) are

* **Corresponding Author**

(fkececioglu@ksu.edu.tr) ORCID ID 0000 – 0001 – 7004 – 4947
*(agani@ksu.edu.tr) ORCID ID 0000 – 0002 – 6487 – 6066
(msekkeli@ksu.edu.tr) ORCID ID 0000 – 0002 – 1641 – 3243

Cite this article

Kececioglu O F, Gani A & Sekkeli M (2021). Improved HYBRID intelligent controller design for MPPT of stand-alone PV System. Turkish Journal of Engineering, 5(1), 20-28

Research Article / DOI: 10.31127/tuje.652229

Received: 28/11/2019; Accepted: 18/01/2020

intelligent MPPT methods (Soon and Mekhilef 2015). Conventional MPPT methods pose some problems such as continuous oscillation, low tracking speed and power losses around MPP. Intelligent MPPT methods, however, offer a high tracking speed, accuracy and efficiency (Radjai et al. 2015).

Type-2 Fuzzy Logic System (T2FLS) has been recently used to overcome uncertainties in the modeling process. The output power of a PV panel depends on solar irradiance and panel temperature affected by atmospheric conditions, leading to uncertainties in the operation of a PV system. Compared to Type-1 Fuzzy Logic System (T1FLS) in a PV system, T2FLS is more successful when it comes to handling uncertainties (Kumbasar 2016).

In the present study, a new improved hybrid intelligent controller is proposed in order to reach maximum power of a PV panel with minimum oscillations and the highest tracking speed under all environmental conditions. The proposed hybrid intelligent controller for the MPPT of the PV system relies on the AIC and Interval Type-2 Takagi-Sugeno-Kang Fuzzy Logic Controller (AIC IT2-TSKFLC).

The present study is organized as follows: MPOLC re-lift configuration for PV system is analyzed in Section 2.The proposed hybrid intelligent controller is presented in Section 3. Simulation studies and dynamic performance of the proposed method are discussed in Section 4. Finally, the conclusions of the study are explained in Section 5.

2. ANALYSIS OF MPOLC RE-LIFT CONFIGURATION FOR PV SYSTEM

The output voltage of a single PV panel does not suffice for on-grid or off grid-connected PV systems, and thus it must be increased, which requires a higher voltage level provided by the series connection of PV panels. However, the number of series-connected PV panels may bring about limitations in practice such as PV voltage isolation, efficiency and shadowing effect. As a result, step-up converters such as MPOLC are essential to provide high voltage conversion gain for PV systems (Ozdemir et al. 2017).The proposed MPOLC re-lift configuration performs the MPPT of a PV system without needing any additional DC/DC converter, and prevents losses caused by an additional DC/DC converter. MPOLC in a re-lift configuration is derived from the positive output Luo converter in a self-lift configuration. Instead of using two switches in the positive output Luo converter, MPOLC in re-lift configuration uses a single switch to perform a DC-DC step-up voltage conversion. The voltage lift technique improves circuit properties. MPOLC is analyzed operating in the continuous conduction mode. Circuit elements of MPOLC are assumed to be ideal when steady-state analysis is carried out (Kececioglu 2019). The steady-state analysis is carried for two different modes: switch-on and switch-off. MPOLC with a re-lift configuration is shown in Fig. 1.*Vs* is the input voltage, and V_L is the load voltage of MPOLC.

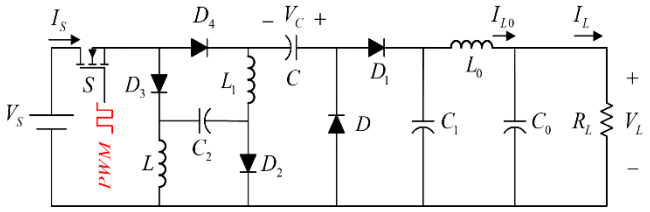

Figure 1. Modified positive output Luo converter with re-lift configuration

2.1. Analysis for Mode-1: Switch-On

The equivalent circuit of MPOLC for the switch-on mode is shown in Fig.2. In the switch-on mode, *D1-D2-D3-D4* diodes are forward biased, while D diode is reverse biased.

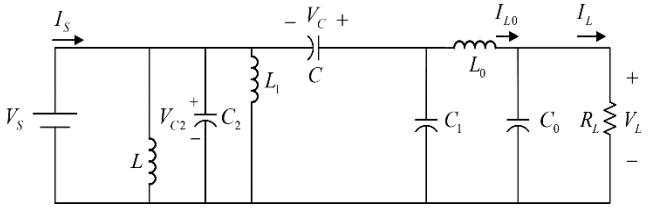

Figure 2. Equivalent circuit for switch-on

The voltage across the inductors *L* and L_1 are equal to input voltage (V_S). The voltage across capacitor C_2, V_{C2} is also equal to V_S, and defined as:

$$v_L = L\frac{di_L}{dt} = v_{L1} = L_1\frac{di_{L1}}{dt} = V_S = V_{C2} \quad (1)$$

Similarly, inductor L_0 current equation is calculated as:

$$v_{L0} = L_0\frac{dI_{L0}}{dt} = V_{C1} - V_L \quad (2)$$

Using Kirchhoff's voltage law, an equation related voltage across capacitor *C* and C_0 is defined as:

$$V_S + V_C = V_{C1} \quad (3)$$

Current (i_{C0}) through capacitor C_0 is expressed as:

$$i_{C0} = C_0\frac{dv_{C0}}{dt} = I_{L0} - I_L \quad (4)$$

Using Kirchhoff's current law, the current equations for *C*, C_1 and C_2 are calculated as:

$$i_C - i_{C1} = C\frac{dv_C}{dt} - C_1\frac{dv_{C1}}{dt} = I_{L0} \quad (5)$$

$$i_C + i_{C2} = C\frac{dv_C}{dt} + C_2\frac{dv_{C2}}{dt} = I_S - i_L - i_{L1} \quad (6)$$

2.2. Analysis for Mode-1: Switch-Off

The equivalent circuit of MPOLC for the switch off mode is shown in Fig. 3. *D* diode is forward biased and *D1-D2-D3-D4* diodes are reverse biased when S switch is turned off.

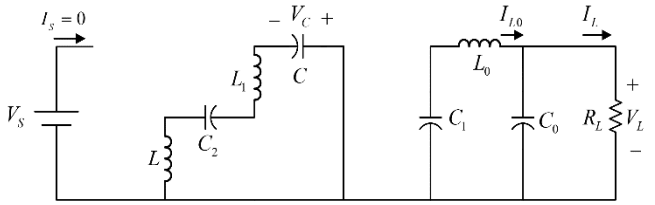

Figure 3. Equivalent circuit for switch-off

The current through the capacitor C_0 is expressed as:

$$i_{C0} = C_0 \frac{dv_{C0}}{dt} = I_{L0} - I_L \tag{7}$$

Similarly, current through capacitors C, C_1 and C_2 are defined as:

$$i_{C1} = C_1 \frac{dv_{C1}}{dt} = -I_{L0} \tag{8}$$

$$i_{C2} = i_C = C_2 \frac{dv_{C2}}{dt} = C \frac{dv_C}{dt} = -i_{L1} = -i_L \tag{9}$$

The voltage across inductors L_0 is calculated as:

$$v_{L0} = L_0 \frac{dI_{L0}}{dt} = V_{C1} - V_L \tag{10}$$

The voltage across inductors L and L_1 are defined as:

$$V_{L-OFF} + V_{L1-OFF} + V_{C2} - V_C = 0 \tag{11}$$

or

$$v_L = L \frac{di_L}{dt} = V_{L1-OFF} + V_{C2} - V_C \tag{12}$$

or

$$v_{L1} = L_1 \frac{di_{L1}}{dt} = V_{L-OFF} + V_{C2} - V_C \tag{13}$$

The inductor current i_L increases in the mode-1 period, and decreases in the mode-2 period. V_S and $-V_{L\text{-}OFF}$ are the corresponding voltages across L. Therefore,

$$DTV_I = (1-D)TV_{L-OFF} \tag{14}$$

Therefore,

$$V_{L-OFF} = \frac{D}{1-D} V_S \tag{15}$$

In a similar way, the inductor current i_{L1} increases in the mode-1 period, and decreases in the mode-2 period. The corresponding voltages across L_1 are V_S and $-V_{L1\text{-}OFF}$. Thus,

$$DTV_I = (1-D)TV_{L1-OFF} \tag{16}$$

and

$$V_{L1-OFF} = \frac{D}{1-D} V_S \tag{17}$$

The Eq. 11 can be modified using Eqs. 1, 15 and 16 as follows:

$$\frac{D}{1-D} V_S + \frac{D}{1-D} V_S + V_S - V_C = 0 \tag{18}$$

$$V_C = \frac{1+D}{1-D} V_S \tag{19}$$

Using Eqs. 2-3, the output voltage of converter (V_L) is calculated as:

$$V_L = V_S + V_C \tag{20}$$

$$V_L = V_S + \frac{1+D}{1-D} V_S = \frac{2}{1-D} V_S \tag{21}$$

The voltage transfer ratio (M) is calculated as:

$$M = \frac{V_L}{V_S} = \frac{2}{1-D} \tag{22}$$

2.3. Design Constraints of MPOLC

In MPOLC analysis, element boundary values are calculated using Eqs. 23-30 based on current changes in inductors and voltage changes in capacitors. The variation ratio of the current through inductor L is expressed as:

$$\zeta = \frac{\Delta I_L / 2}{I_L} = \frac{R_L D}{M^2 fL} \tag{23}$$

Similarly, the variation ratio for inductor L_1 is defined as:

$$\zeta_1 = \frac{\Delta I_{L1} / 2}{I_{L1}} = \frac{R_L D}{M^2 fL_1} \tag{24}$$

The variation of the current through diode I_D is given as:

$$\xi = \frac{\Delta I_D / 2}{I_D} = \frac{R_L D}{fL_{eq} M^2} \tag{25}$$

Here, L_{eq} is the equivalent inductance $L//L_1$. The variation ratio of the voltage across the capacitor C is calculated as:

$$\sigma = \frac{\Delta V_C / 2}{V_C} = \frac{1}{fCR_L(1+D)} \tag{26}$$

In a similar way, the variation ratio for capacitor C_1 is defined as:

$$\sigma_1 = \frac{\Delta V_{C1} / 2}{V_{C1}} = \frac{1}{fC_1 R_L M} \tag{27}$$

The variation ratio for the capacitor C_2 is expressed as:

$$\sigma_2 = \frac{\Delta V_{C2}/2}{V_{C2}} = \frac{M}{2fC_2R_L} \quad (28)$$

The variation ratio of the current through the inductor L_0 is calculated as:

$$\zeta_0 = \frac{\Delta I_{L0}/2}{I_{L0}} = \frac{1}{8f^2C_1ML_0} \quad (29)$$

Finally, the variation ratio of the voltage across the capacitor C_0 is expressed as:

$$\sigma_0 = \frac{\Delta V_{CO}/2}{V_{CO}} = \frac{1}{64R_LMf^3L_0C_0C_1} \quad (30)$$

The boundary between continuous conduction mode (CCM) and discontinuous conduction mode (DCM) is calculated when the diode current I_D becomes zero during switch-off mode prior to the next switch-on period. The boundary condition for DCM is $\xi \geq 1$ and calculated as:

$$\frac{RD}{fL_{eq}M^2} \geq 1 \quad (31)$$

The Eq. 31 can be used to find the minimum value of equivalent inductance L_{eq} required for the CCM operation of the MPOLC for given load resistance (R_L) and switching frequency (f) values (Pansare et al. 2017).

3. PROPOSED HYBRID INTELLIGENT CONTROLLER

Fuzzy logic control (FLC) is a popular method for performing MPPT in a PV system. Numerous studies (Tai et al. 2016) in the literature indicated that Type-1 FLC (T1FLC) did not display a high performance in highly uncertain situations in the system. On the other hand, a Type-2 FLC using Type-2 fuzzy sets displayed a better performance. In the present study, a hybrid intelligent controller, AIC IT2-TSKFLC, is proposed for the MPPT of a PV system with a combination of AIC algorithm and Type-2 FLC. The proposed hybrid intelligent controller is shown in Fig.4.

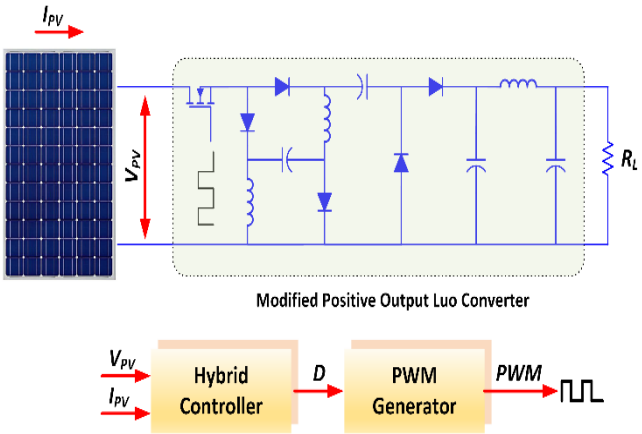

Figure 4. Proposed hybrid intelligent controller

As shown in Fig. 4, the proposed hybrid intelligent controller is used on the PV system consisting of a PV panel and MPOLC. Instantaneous voltage (V_{PV}) and current (I_{PV}) are calculated using PV panel using voltage and current sensors. The AIC algorithm is used to generate the error function of IT2-TSKFLC, which is responsible for the minimization of the error of MPP. IT2-TSKFLC calculates the duty ratio of the converter (D). The output of the proposed hybrid intelligent controller is applied to switching device of MPOLC via PWM generator. The control signal, which is the output of IT2-TSKFLC, is generated by Type-2 Fuzzy Sets. A Type-2 Fuzzy Set consists of triples $(x,u):\mu_{\tilde{A}}(x,u)$ where x $\in$ X is a primary membership value, u $\in J_x$ (J_x represents the range of primary membership for a given x), and a secondary membership, $\mu_{\tilde{A}}(x,u)$ for each member of domain, can be expressed as follows:

$$\tilde{A} = \left\{\left((x,u),\mu_{\tilde{A}}(x,u)\right) \mid \forall x \in X, \forall u \in J_x \subseteq [0,1], \mu_{\tilde{A}}(x,u) \in [0,1]\right\} \quad (32)$$

Footprint of uncertainty (FOU) in Fig. 5 is the limited domain corresponding to the primary uncertainty of Type-2 fuzzy set between upper ($\overline{\mu}_{\tilde{A}}$) and lower ($\underline{\mu}_{\tilde{A}}$) membership functions. It is assumed that FOU domain between upper and lower membership functions in Type-2 fuzzy set is an infinite Type-1 membership function. While the main properties of the general Type-2 fuzzy sets were preserved, interval Type-2 fuzzy sets were introduced as an alternative that reduces the computational burden (Mendel and John 2002). When all $\mu_{\tilde{A}}(x,u)$ is equal to 1, $\tilde{A}$ is an interval Type-2 fuzzy set. Interval Type-2 fuzzy sets can be defined as follows:

$$\tilde{A} = \left\{\left((x,u),1\right) \mid \forall x \in X, \forall u \in J_x \subseteq [0,1]\right\} \quad (33)$$

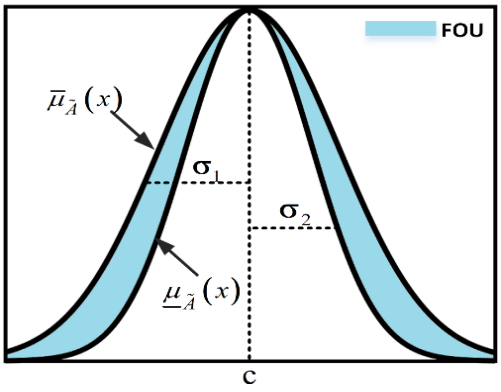

Figure 5. Gaussian type-2 fuzzy set

Both general and interval Type-2 fuzzy logic membership functions are three dimensional. However, they differ in terms of secondary membership function value of an interval Type-2 fuzzy logic function, which is equal to 1. Hence, their computational time is shorter compared to general Interval Type 2 Fuzzy Logic Controller (IT2-FLC). IT2-FLC consists of four parts: fuzzifier, rules & inference, type reducer and defuzzifier. The internal structure of IT2-FLC is shown in Fig. 6.

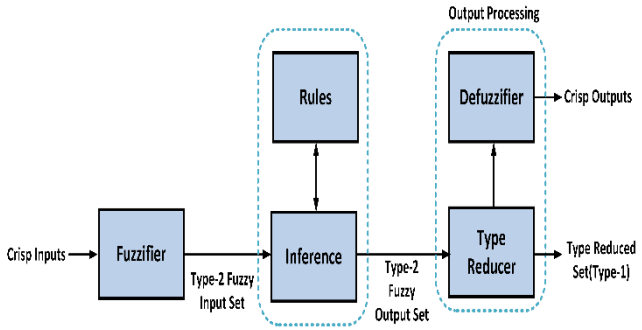

Figure 6. The internal structure of IT2-TSKFLC

In the present study, the antecedent parameters of IT2-TSKFLC are preferred as Type-2 fuzzy sets, and consequent parameters are selected as zero-order polynomials (Karnik et al. 1999). The rule base can be defined as:

$$R^k : IF\ x_1\ is\ \tilde{A}_1^{\,j}\ AND\ x_2\ is\ \tilde{A}_2^{\,n}$$
$$THEN\ R_k = p_k x_1 + q_k x_2 + r_k \qquad (34)$$

where k=1,2,....,25 denotes rule numbers, x_1, x_2 represent input variables (*e*, *de*), $\tilde{A}_1^{\,j}$ and $\tilde{A}_2^{\,n}$ are membership functions, R_k is the rule output and p_k , q_k , r_k are the consequent parameters. As shown in Fig. 5, Gaussian type membership function is used in the present study. The mathematical equations of Gaussian type membership function are given in Eqs. 35- 36.

$$\overline{\mu}_{A_i^j}(x_i) = \exp\left\{-\frac{1}{2}\left(\frac{x_i - c_{ij}}{\overline{\sigma}_{ij}}\right)^2\right\} \qquad (35)$$

$$\underline{\mu}_{A_i^j}(x_i) = \exp\left\{-\frac{1}{2}\left(\frac{x_i - c_{ij}}{\underline{\sigma}_{ij}}\right)^2\right\} \qquad (36)$$

Here, $\mu_{A_i^j}(x_i)$ is the degree of membership for input variable, c_{ij} denotes the mean value of function, σ_{ij} is standard deviation, and x_i is the input variable (Acikgoz et al. 2019). The controller proposed in the present study has two inputs (*e*, *de*) and a single output (*D*) which is duty ratio for DC-DC converter. The detailed structure of IT2-TSKFLC is shown in Fig. 7.

As shown in Fig. 7, IT2-TSKFLC configuration has seven layers.

Layer-1: This is the input layer. As shown in Fig. 4, the inputs of controller (*e*, *de*) are generated AIC algorithm using (V_{PV}, I_{PV}) values of PV panel and are described in Eq. 37. The characteristic curves of the AIC algorithm are shown in Fig. 8. It can be observed that the angle equals to zero around MPP point.

$$\tan^{-1}\left(\frac{I_{pv}}{V_{pv}}\right) + \tan^{-1}\left(\frac{dI_{pv}}{dV_{pv}}\right) = 0 \qquad (37)$$

Layer-2: This layer determines the degrees of the membership functions for inputs. The membership functions of the input and the rule base of the proposed hybrid intelligent controller must be determined based on MPP condition for IT2-TSK fuzzy inference system. The membership functions are labeled as (MF_1-MF_5), The membership functions are determined for error (*e*) and change of error (*de*) of the proposed hybrid control structure. Input membership functions are scaled based on a range of (-1, +1). Five Gaussian membership functions designed for the inputs are shown in Fig. 9.

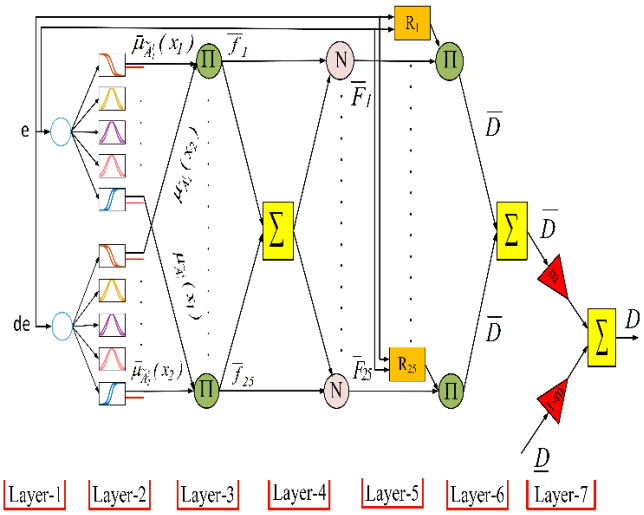

Figure 7. The structure of IT2-TSKFLC

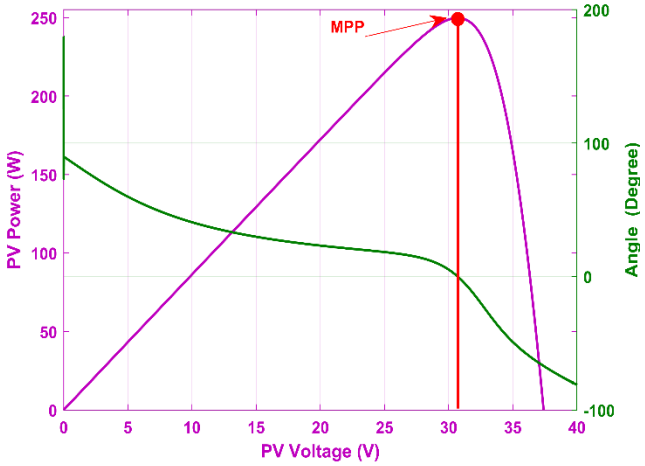

Figure 8. AIC angle curve and PV panel power compared with voltage characteristic curves

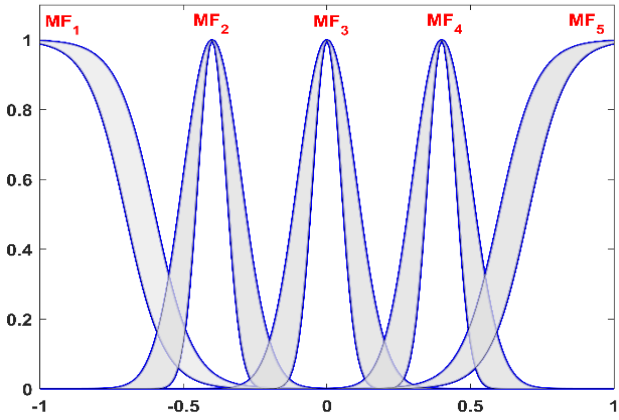

Figure 9. Five Gaussian membership functions designed for inputs

Layer-3: The third layer of the IT2-TSKFLC consists of the nodes represented by *Π*. The firing strengths of the

fuzzy rules are defined as lower and upper using product operator. The fuzzy rules of the proposed hybrid intelligent controller are presented in Table 1.The mathematical equations of the Layer-3 are calculated as:

$$\overline{f}_{(n-1)\times J+j} = \overline{\mu}_{A_1^j}(x_1) * \overline{\mu}_{A_2^n}(x_2) \quad n=1,2,\ldots,N \text{ and } k=(n-1)\times J+j \tag{38}$$

$$\underline{f}_{(n-1)\times J+j} = \underline{\mu}_{A_1^j}(x_1) * \underline{\mu}_{A_2^n}(x_2) \quad n=1,2,\ldots,N \text{ and } k=(n-1)\times J+j \tag{39}$$

Table 1. Fuzzy rules of proposed hybrid intelligent controller

D		de				
		MF1	**MF2**	**MF3**	**MF4**	**MF5**
e	**MF1**	R1	R2	R3	R4	R5
	MF2	R6	R7	R8	R9	R10
	MF3	R11	R12	R13	R14	R15
	MF4	R16	R17	R18	R19	R20
	MF5	R21	R22	R23	R24	R25

MF: Membership Function R: Rule

Layer-4: This layer is also called the normalization layer, and each node is labeled as N. Normalization is calculated by proportioning the firing strength of each node rule to the sum of the firing strengths of all rules. This process can be expressed as:

$$\overline{F_k} = \frac{\overline{f_k}}{\sum \overline{f_k}} \qquad k=1,2,\ldots,25 \tag{40}$$

$$\underline{F_k} = \frac{\underline{f_k}}{\sum \underline{f_k}} \qquad k=1,2,\ldots,25 \tag{41}$$

Layer-5: It is a rule layer. The rule layer outputs are calculated based on the rule base. Layer outputs are calculated as:

$$R_k = p_k e + q_k de + r_k \quad k=1,2,\ldots,25 \tag{42}$$

Layer-6: The multiplication of membership degrees for upper and lower membership functions as well as linear functions is performed in this layer.

$$\overline{D} = \prod_{k=1}^{25} \overline{F_k}\,\overline{R_k} \tag{43}$$

$$\underline{D} = \prod_{k=1}^{25} \underline{F_k}\,\underline{R_k} \tag{44}$$

Layer-7: Biglarbegian-Melek-Mendel (BMM), which is a closed-form type reduction and defuzzification method, is used in this layer (Coteli et al. 2017). Closed mathematical form of type reduction and defuzzification process for the proposed IT2-TSKFLC is defined as:

$$D = m\frac{\sum_{k=1}^{25} \overline{f_k}\,\overline{R_k}}{\sum_{k=1}^{25} \overline{f_k}} + (1-m)\frac{\sum_{k=1}^{25} \underline{f_k}\,\underline{R_k}}{\sum_{k=1}^{25} \underline{f_k}} \tag{45}$$

4. SIMULATION STUDIES

The improved hybrid intelligent controller based on AIC-Interval Type-2 TSK Fuzzy Logic Controller for MPPT is simulated in MATLAB/Simulink environment using Sim Power System Toolbox. Solar irradiance and panel temperature values were obtained from a 10kWp real solar plant in Kahramanmaras. The performance and stability of the proposed control structure are analyzed under real environmental conditions.

4.1. Stand-Alone PV System and MPOLC Modelling

Single PV panel is used for simulation studies. The maximum power of a PV panel at the STC is 250W. Electrical characteristic parameters of the PV panel are given in Table 2. Calculated boundary circuit element values of the MPOLC using above mentioned design constraints are listed in Table 3. The MPOLC circuit element values in the simulation studies are selected higher than the calculated boundary circuit element values for a better continuous conduction mode (CCM) of operation.

Table 2. Electrical characteristic parameters of PV panel

Panel Type	Soltech STH-250-WH	
Optimum Operating Voltage	V_{MP}	30.7 V
Optimum Operating Current	I_{MP}	8.15 A
Open – Circuit Voltage	V_{oc}	37.4 V
Short – Circuit Current	I_{sc}	8.63 A
Maximum Power at STC	P_{max}	250 W
Panel Efficiency	η	15.4 %

Table 3. Calculated boundary circuit element values of MPOLC

V_s	30.7 V	L	0.23 mH
V_L	154.1 V	C_0	62.5 uF
R_L	100 Ω	C	15.61 uF
D	0.6	C_1	4.98 uF
L_o	0.015 mH	f	40 kHz
M	5.02	ζ_1	0.2
ζ	0.2	σ_1	0.01
σ	0.01	σ_2	0.01
σ_o	0.01	ζ_0	0.2
L_1	0.23 mH	C_2	62.74 uF

4.2. Simulation Results

The dynamic response of the proposed hybrid control structure is analyzed using real solar irradiance and panel temperature values. The actual values of solar parameters are obtained throughout a day from ta solar PV plant of power 10kWp installed in Kahramanmaras Sutcu Imam University. A view of solar PV plant is shown in Fig. 10. The actual solar irradiance and panel temperature values obtained from the solar PV plant on 22/08/2019 are shown in Figure 11.

Figure 10. A view of solar PV plant

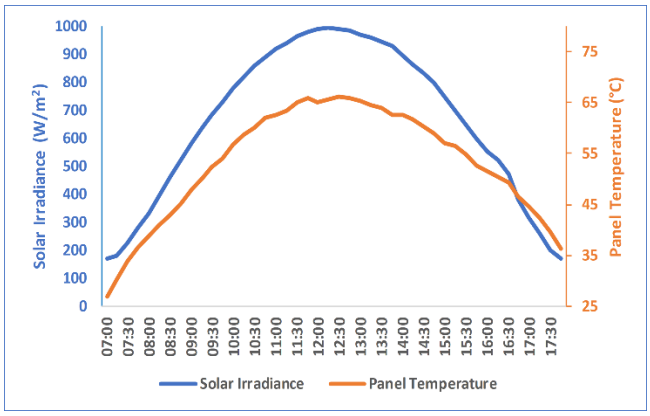

Figure 11. Daily variation of solar irradiance and panel temperature values

Actual values are sampled for the analysis of simulation studies. The sampled values are shown in Fig. 12(a). The output power curves of PV panel versus voltage are shown in Fig 12(b). It can be noted that sampled values and output power curves are analyzed under five different states for this simulation study.

Total simulation time was calculated as 0.3 s. State 1 indicates that solar irradiance and panel temperature values are fixed at 600 W/m² and 25˚C, respectively. The solar irradiance and panel temperature values were suddenly increased from 600 W/m² to 800 W/m² and 25˚C to 40˚C at t=0.1 s. Later, solar irradiance and panel temperature are increased in a similar manner to State 2. At the last two states, solar irradiance and panel temperature are decreased to represent the afternoon of a day for the analysis of MPP tracking performance of the proposed controller. As seen in Fig. 12(b), MPP power values of states are calculated 149.5 W, 187 W, 218 W, 172 W and 119 W, respectively.

Simulation results are given in Fig.13. It can be understood at the first state that PV power with conventional AIC method is 148.4 W, where PV power with the proposed control structure is 149.2 W.

The settling times of the proposed control structure and AIC method are 9.5 ms and 37.8 ms, respectively. At the second and third states of case, the MPP power of the PV panel was increased from 187 W to 218 W. PV power with AIC method was also increased from 186.1 W to 216.6 W. PV power with the proposed hybrid control structure was increased from 186.8 W to 217.9 W. At the last two states, MPP power of the PV panel was decreased from 172 W to 119 W. In addition, PV power with the proposed hybrid control structure was decreased from 171.8 W to 118.7 W, while PV power with AIC method was decreased from 170.8 W to 117.3W. As shown in Fig. 13(b), the proposed hybrid control structure successfully reduced the oscillation of the output power of DC-DC converter. PV power performance of both controllers were compared for all states in terms of transient performance indexes, and the results are summarized in Table 4.Maximum power efficiency demonstrates the extent to which the proposed controller can track MPP. The maximum power efficiency is calculated using ratio of the output power of the panel to the maximum power of the panel. The maximum power efficiencies of both controllers for all states are shown in Fig. 14.

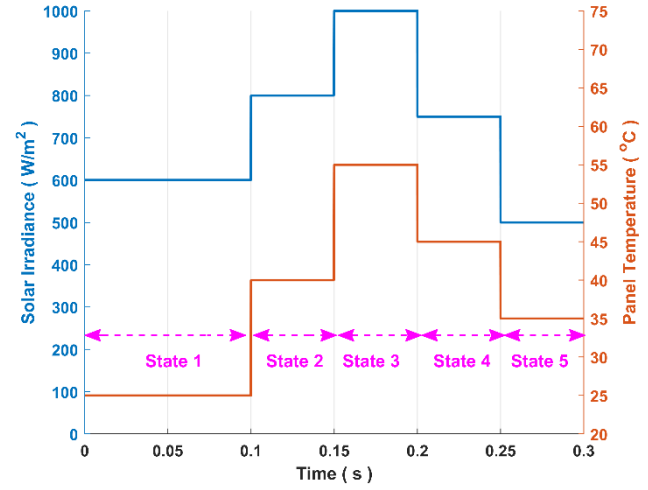

(a)

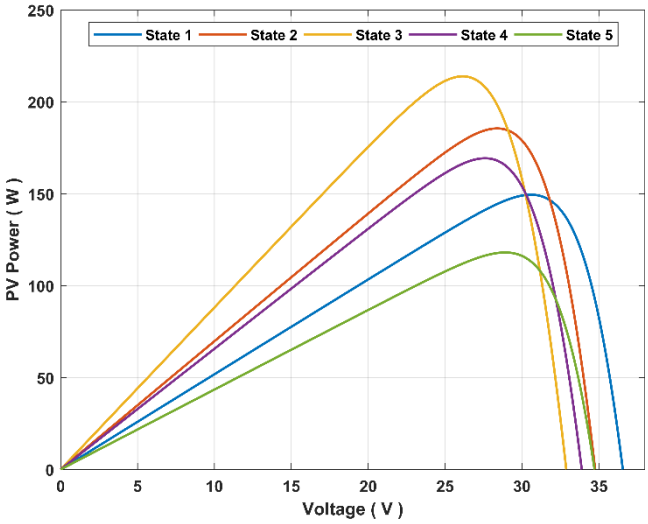

(b)

Figure 12. Solar irradiance and panel temperature (a) and PV power curves (b)

Table 4. Performance comparison of both controllers

All States	AIC - IT2-TSKFLC		AIC	
	Settling Time (ms)	Rise Time (ms)	Settling Time (ms)	Rise Time (ms)
State 1	9.5	1.37	37.8	1.53
State 2	3	0.11	28	17.5
State 3	2	0.12	16	9.5
State 4	2.7	0.09	30	4.8
State 5	5.2	0.09	49	4.2

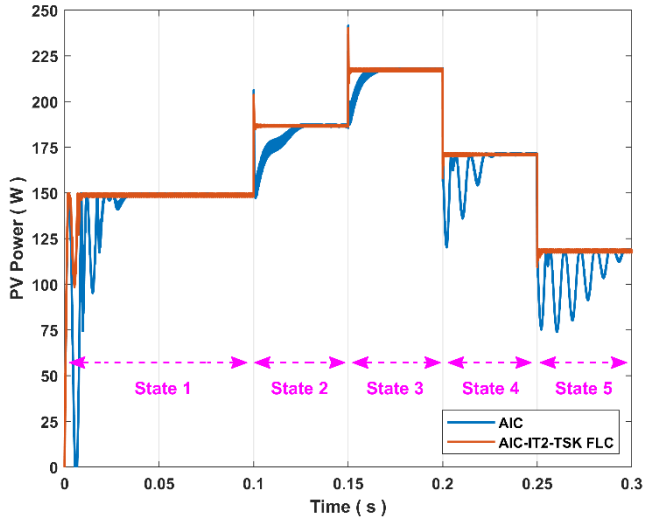

(a)

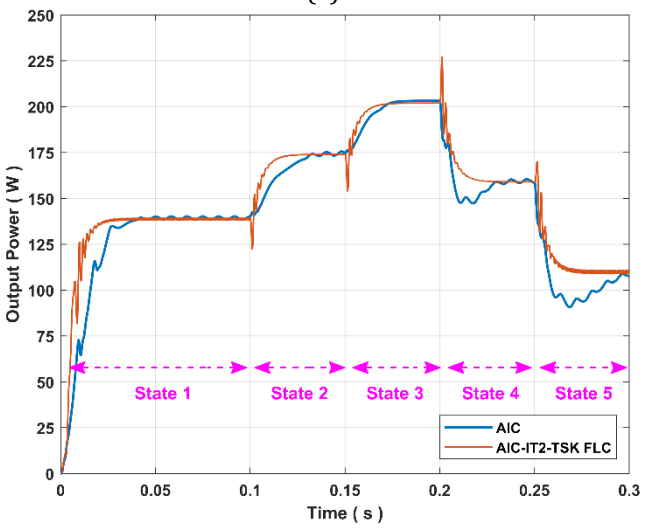

(b)

Figure 13. Output power responses of PV panel (a) and converter (b)

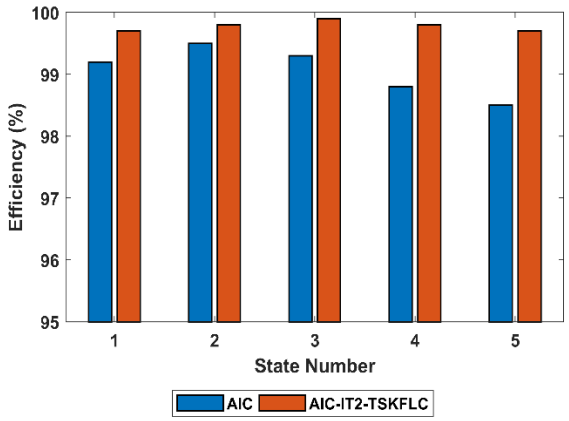

Figure 14. Maximum power efficiency comparison of both controllers

As seen in Fig. 14, the proposed hybrid control structure displays a higher performance compared to conventional AIC method in terms of maximum power efficiencies at all states. As a result, both controller methods extracted almost a maximum power from PV panel following the settling times for all states. While conventional AIC method has a long transient response for all states, the proposed control structure has a shorter transient response and a higher stability of PV power and converter output power. In addition, the proposed control structure tracked MPP values without any oscillation in PV power.

5. CONCLUSION

The present study proposed an improved hybrid control structure combined with AIC and IT2-TSKFLC for maximum power point tracking of a stand-alone PV system. MPOLC with a high voltage conversion gain was preferred for the PV system. IT2-TSKFLC consists of an effective and robust control structure that responded rapidly to unstable environmental conditions, and efficiently tracked MPP. Later, simulation studies were conducted for five different states to test the stability and dynamic performance of the proposed hybrid control structure. The hybrid control structure in the present study was compared with a conventional AIC method. The dynamic performance results obtained from five different states suggest that the proposed hybrid control structure ensured less oscillations and displayed a good steady state response on output powers of PV panel and MPOLC under unstable conditions. The proposed hybrid control structure has provided ms improvements. These improvements will contribute to the more stable and faster operation of the PV system. Furthermore, the proposed hybrid control structure improved its maximum power efficiency under rapidly changing environmental conditions.

ACKNOWLEDGEMENT

This work was financially supported by the Kahramanmaras Sutcu Imam University, Scientific Research Projects Unit, the project entitled “Optimal Control and Implementation of Maximum Power Point in Photovoltaic Systems” under Project No: 2018/5-11 D

REFERENCES

Acikgoz H, Kumar A, Beiranvand H & Sekkeli M (2019). Hardware implementation of type-2 neuro-fuzzy controller-based direct power control for three-phase active front-end rectifiers. International Transactions on Electrical Energy Systems, 29(10), 693-702. DOI: 10.1002/2050-7038.12066

Coteli R, Acikgoz H, Ucar F & Dandil B (2017). Design and implementation of Type-2 fuzzy neural system controller for PWM rectifiers. International Journal of Hydrogen Energy, 42(32), 20759-20771. DOI: 10.1016/j.ijhydene.2017.07.032

Dixit T V, Yadav A & Gupta S (2018). Experimental assessment of maximum power extraction from solar panel with different converter topologies. International Transactions on Electrical Energy Systems, 29(2), 1-33. DOI: 10.1002/etep.2712

Dogmus O, Kilic E, Sit S & Gunes M (2017). Adaptation of Optimized PID Controller with PSO Algorithm to Photovoltaic MPPT System. Kahramanmaraş Sütçü İmam University Journal of Engineering Sciences, 20(4), 1–8.

Karnik N N, Mendel J M & Liang Q (1999). Type-2 fuzzy logic systems. IEEE Transactions on Fuzzy Systems, 7(6), 643–658. DOI: 10.1109/91.811231

Kececioglu O F (2019). Robust control of high gain DC-DC converter using Type-2 fuzzy neural network controller for MPPT. *Journal of Intelligent & Fuzzy Syst*ems, 37(1), 941-651. DOI: 10.3233/JIFS-181770

Kececioglu O F, Acikgoz H & Gani A (2018). Fuzzy - PI Based MPPT Control for Photovoltaic Systems. Innovations in Intelligent Systems and Applications Conference (ASYU), Adana, Turkey. DOI: 10.1109/ASYU.2018.8554023

Kumbasar T (2016). Robust stability analysis and systematic design of single-input interval type-2 fuzzy logic controllers. IEEE Transactions on Fuzzy Systems, 24(3), 675–694. DOI: 10.1109/TFUZZ.2015.2471805

Luo F L (1997). Luo-converters, a series of new DC-DC step-up (boost) conversion circuits. Proceedings of Second International Conference on Power Electronics and Drive Systems, Singapore, 882-888. DOI: 10.1109/PEDS.1997.627511

Mendel J M & John R I B (2002).Type-2 fuzzy sets made simple. *IEEE Transactions on Fuzzy Systems*, 10(2), 117-127. DOI: 10.1109/91.995115

Ozdemir S, Altin N & Sefa I (2017). Fuzzy logic based MPPT controller for high conversion ratio quadratic boost converter. International Journal of Hydrogen Energy, 42(38), 17748-17759. DOI: 10.1016/j.ijhydene.2017.02.191

Pansare C, Sharma S K, Jain C & Saxena R (2017). Analysis of a modified positive output Luo converter and its application to solar PV system. IEEE Industry Applications Society Annual Meeting, Cincinnati, OH, USA, 1–6.

Radjai T, Gaubert J P, Rahmani L & Mekhilef S (2015). Experimental verification of P&O MPPT algorithm with direct control based on fuzzy logic control using CUK converter. International Transactions on Electrical Energy Systems, 25(12), 3492–3508. DOI: 10.1002/etep.2047

Soon T K & Mekhilef S (2015). A fast-converging MPPT technique for photovoltaic system under fast-varying solar irradiation and load resistance. IEEE Transactions on Industrial Informatics, 11(1), 176-186. DOI: 10.1109/TII.2014.2378231

Tai K, El-Sayed A R, Biglarbegian M, Gonzalez C I, Castillo O & Mahmud S (2016). Review of recent type-2 fuzzy controller applications. Algorithms, 9(2), 1-19. DOI: 10.3390/a9020039

Turkish Journal of Engineering

https://dergipark.org.tr/en/pub/tuje

e-ISSN 2548-0960

Evaluation of heavy metal content of salts between Eskıkışla and Ocakbaşı (Kırıkkale) villages

Bilgehan Yabgu Horasan [*1], **Alican Ozturk** [2]

[1]*Selcuk University, Sarayonu Vocational High School, Environmental Protection Technologies, Konya, Turkey*
[2]*Konya Technical University, Faculty of Engineering and Natural Sciences, Geological Engineering Department, Konya, Turkey*

Keywords
Heavy metal
Rock salt
Eskikısla
Ocakbası
Kırıkkale

ABSTRACT

Salt, which is the main nutrient, is a very important raw material in the life of living organisms and industry. Salt production and consumption have improved and increased due to technological developments and industrialization. Salt has been used in the world and in our country since very ancient times. It is used in many fields, especially in the chemical industry, metallurgy, textile, medicine, and agriculture. In addition to sea, lake and spring salts, Turkey has very rich rock salt reserves. The Neogene aged Çankırı-Çorum Basin is one of the important basins where evaporitic formations are observed in the Central Anatolia region. Chemical analyses were carried out to determine the amount of heavy metal in salt samples taken from Oligocene aged units observed in the area between Ocabaşı and Eskikışla springs (Delice) in the Çankırı-Çorum basin. SEM-EDX, XRF and ICP-OES devices were used to determine the geochemical properties and quantities of heavy elements. According to the results of XRF, Na % (33.70-38.30), Cl %(52.10 - 57.70) SO_3 %(0.75-1.93), Al_2O_3 %(0.90-1.93), CaO %(0.58-2.69), MgO %(0.40-1.41) Fe_2O_3 % (0.18-0.64), SiO_2 %(1.75-4.95), SrO, % (<0.010), BaO % (<0.010), Cr_2O_3 %(<0.010), K_2O %(0.008-0.25), MnO %(<0.010) results are found. In the determination of heavy metals made with ICP-OES, it was determined that the heavy metals (Hg, As, Pb, Cd) published in the Turkish food codex salt communiqué were below the limit values.

1. INTRODUCTION

Salt, which is known to have been consumed throughout human history, is known to be a source of income and trade in Chinese civilization, meat and fish salting in Egyptian civilization, a means of paying taxes and salaries to soldiers in Romans, an order of wealth in Renaissance Europe and a sacred food in Central Asian Turkish culture (Caglar 2015). Evaporites are rocks that chemically precipitate as a result of the evaporation of saturated and salty water on the surface or near the surface with the effect of sun rays. Because they provide important information about paleoclimate and environmental conditions and have an economic value industrially, they are important deposits (Altay 2010). They have a wide range of uses, especially in the salt chemical industry, metallurgy, textile, medicine, and agriculture (Donat 2016). Salt, which is known to have been used for different purposes by civilizations in human history, continues to be used by humanity today without losing its importance. Salt is obtained from the ocean (sea waters), lake salts and rock salts (U.S. 2018). Turkey is a country that is self-sufficient in salt production and consumption in 2015, it has received $ 11 million in revenue by exporting salt to 64 countries (Donat 2016). China ranks first in salt production and export in the world, followed by the USA, India, Canada, and Australia (U.S. 2019). The world's largest producer of salt, China, USA, and India, meet a significant portion of salt demand. Among the salt-producing countries on the European continent, Germany leads, followed by Turkey, France, Spain, and Poland. Especially during the harsh winter months, the amount of production is increasing, and most of the salt needed by the European continent is met by these countries. Rock salt (halite), an odorless, water-soluble, easily friable material, consists of Na^+ and Cl^- ions and crystallizes in the cubic system. Although it is colorless in its pure form, it can be in different colors (green, gray, yellow) depending on the environment. The deposits of minerals are different in waters of terrestrial origin and waters of marine origin. The change of molar ratios in seawater creates important changes in the type of minerals and order of the deposition of potassium minerals. Evaporite minerals formed by evaporation of terrestrial waters are more diverse than evaporite minerals formed in waters of

* **Corresponding Author**

*(bilgehanyabgu@gmail.com) ORCID ID 0000 – 0003 – 1899– 0041
(alicanozturktr@gmail.com) ORCID ID 0000 – 0003 – 2748 – 6322

Cite this article

Horasan B Y & Ozturk A (2021). Evaluatıon of heavy metal content of salts between Eskıkışla and Ocakbaşı (Kırıkkale) villages. Turkish Journal of Engineering, 2021, 5(1), 29-34

Research Article / DOI: 10.31127/tuje.652452

Received: 28/11/2019; Accepted: 26/01/2020

marine origin. Borates with economic value, natural soda, and sodium sulfate minerals are formed in a terrestrial environment (Eugster and Hardie 1978; Altay 2010) Operable salt sources are divided into solid and liquid. The areas where liquid production is carried out are oceans, seas, lakes, and water sources containing salt. The areas where solid production is carried out are buried salt deposits. In this context, rock salt deposits observed in the area between Ocakbaşı and Eskikisla plateaus (I - 31 - B3 map) located in the borders of Delice District of Kırıkkale province were investigated and their geochemical properties were examined (Figure 1). In addition, the heavy metal content in the composition of rock salt in the region was evaluated according to the Turkish food index.

2. GEOLOGICAL SETTINGS

The Neogene aged Çankırı-Çorum Basin, located within the Anatolide Tectonic Union, is surrounded by the ophiolitic melange in the north and west, and the Kırşehir Massif in the south (Varol et al. 2004). Old and young tectonic scars are seen in the region (Figure 1). Traces of old and young tectonics are seen in the area. For this reason, the stratigraphy of the underlying rocks is complex. Basin by many researchers (Dellaloğlu 1973; Birgili et al.1975; Seymen 1981; Ünalan and Harput 1983; Kara and Dönmez 1990; Tüysüz and Dellaloğlu 1992; Erdoğan et al. 1996; Seyitoğlu et al. 1997; Varol et al. 2004) have been studied for various purposes. The generally accepted opinion of Tüysüz and Dellaloğlu (1992) regarding the formation of the Çankırı-Çorum Basin is as follows: Çankırı-Çorum Basin, a basin formed after the collision between the two continents on the Izmir-Ankara-Erzincan suture as a result of the collision between Sakarya and Kırşehir in the time interval between late Paleocene(?) early Eocene. The basic units of the basin are Kırşehir Continent, Sakarya Continent, and İzmir-Ankara-Yozgat suture zone. On this foundation, there are units of the Tertiary-aged Çankırı-Çorum Basin. The bottom sedimentary units of the Çankırı-Çorum Basin are Maastrichtian and Paleocene turbidites (Karadenizli 2011; Norman 1972; Kazancı and Varol 1990). The Paleogene part of the filling in the basin consists of marine clastic and the Neogene part consists of terrestrial, clastic and evaporitic rocks. The facies of this filling, which are different and thick, belong to Eocene and Oligocene (Birgili et al. 1975) The Oligocene aged Shin formation, in which salt deposits are found includes massive-stratified conglomerates, parallel and cross-stratified sandstones, stratified siltstones and massive mudstones (Karadenizli 2011).

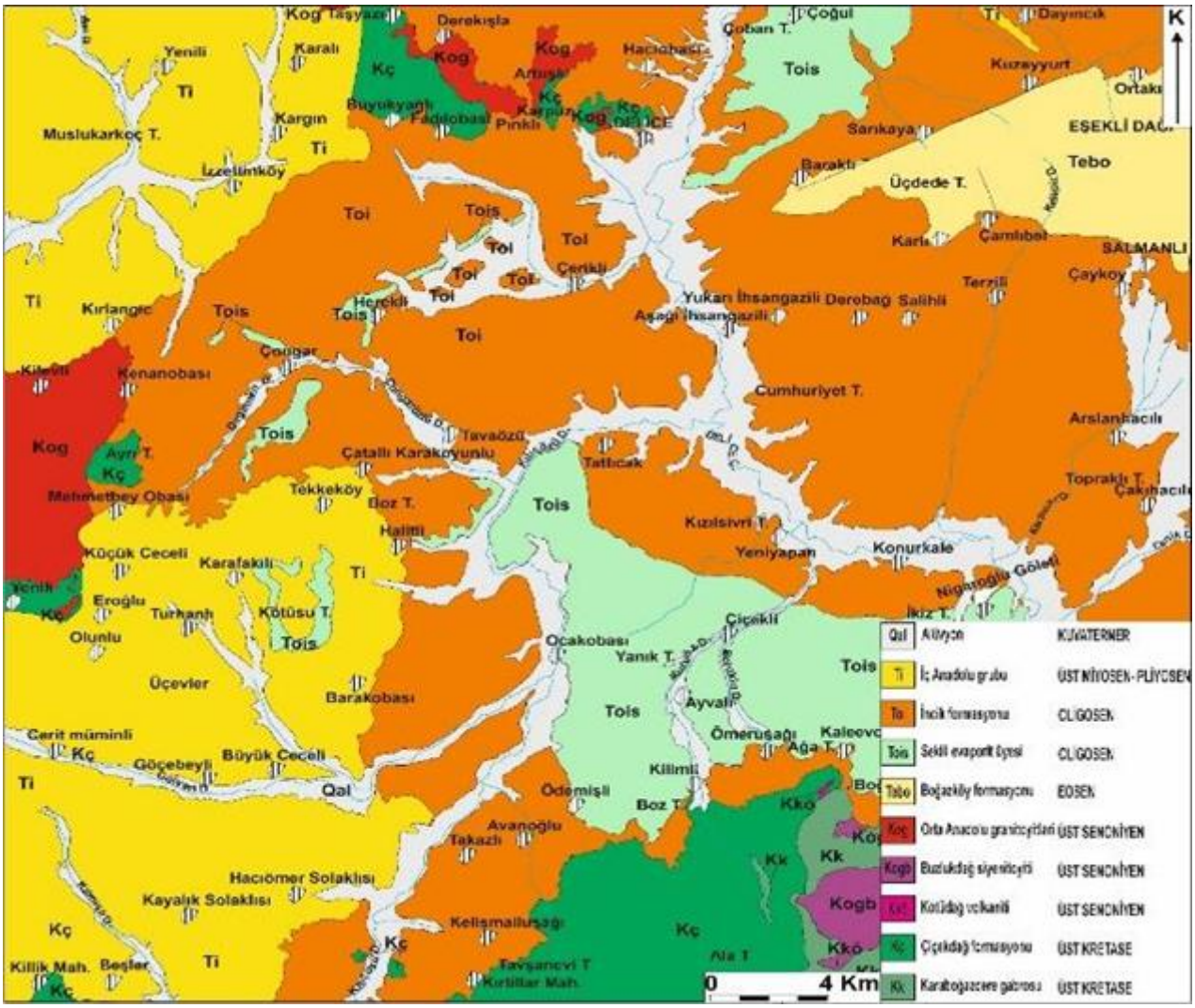

Figure 1. Geological map of the study area and its environs (taken from Dönmez et al. 2005).

2.1. İncik Formation (Toi)

The unit outcrops in large areas in the field and consists of evaporite, red, brown and gray colored, parallel cross-layered, low-cornered round grained, medium-well, loosely affixed terrestrial conglomerate, sandstone and mudstone intercalations. The formation is composed of clastic rocks (Birgili et al. 1975) is called as İncik formation. The lower parts of the İncik formation are intercalated with thin-medium-thick parallel-bedded sandstones, interbedded with medium-well bonded sandstones, gypsum and anhydrite mudstones, and the middle and upper levels are intercalated with mudstones and increasing upwards, cross-layered conglomerate and sandstone (Özgüner and Kızıldağ 2015). Investigation of oil and salt relationship in the study area and its vicinity (Tepecik 2007), investigation of glauberite-halite coexistence in the region (Sönmez 2014) and Halite (NaCl), Gypsum ($CaSO_4$) studies have been carried out for different purposes for salt deposits such as Anhydride ($CaSO_4.2H_2O$), Globerite ($CaNa_2$ $(SO_4)_2$), Tenardite (Na_2SO_4) detection of minerals (Horasan and Ozturk 2019).

2.2. Sekili evaporit member (Tois)

The red, brown, gray, light green, white and variegated colored, medium-thick evaporite, mudstone and sandstone intercalation of the İncik formation is named Sekili evaporite member by Kara (1991). The unit outcrops in the middle and northwest of the Kırşehir-İ31 and İ32 section. The shaped evaporite member is generally composed of anhydrite and gypsum and contains sandstone, and marl intermediate bands and mudstone upward. Gypsum and anhydrides are white and yellowish-white in color, medium-thick bedded, generally pure and crystalline and occasionally lumpy.

It is observed that gypsum and anhydrides are thinner in the lateral direction and mudstones thicken. Sandstone and mudstones are generally thin to medium in thickness and have red-brown, light green and variegated appearance in green colors (Dönmez et al. 2005).

3. MATERIALS AND METHODS

In this study, salt formations observed in the area between Ocakbaşı and Eskikışla springs in Delice district of Kırıkkale province were investigated. The geology of the study area was examined and mapped by using the previous studies. A total of 14 samples were collected during the field studies. Of these samples, 8 Salt (Halite), 2 Gypsum and Anhydrite samples X-RF, 2 Salt (Halit) samples, SEM - EDX and 2 Salt (Halite) ICP-OES and studies were performed. The analyses were carried out in METU MERLAB, Selçuk University İLTEK and Konya Food Agriculture University laboratories.

Textural examinations of SEM-EDX, were performed with Zeis Evo / Is20 brand scanning electron microscope, which is located in Selçuk University Advanced Technology Research and Application Center (İLTEK). The samples taken from the study area were analyzed with 123 eV energy by Bruker brand EDX detector.

X-Ray Fluorescence (XRF) spectrometer is one of the important devices used to determine the elemental and chemical composition. In this study, standard methods were analyzed with Rigaku ZSX Primus II device within METU merlab.

With the ICP-OES, heavy metals contained in salt were analyzed with Perkin Elmer 7000 DV Model device.

3.1. Evaluation of X-RF Results

Chemical analyses were performed on the samples collected from the Sekili member of İncik formation in the study area. Chemical analyses were carried out using X-RF to calculate Na, Cl, SO_3, Al_2O_3, CaO, MgO, Fe_2O_3, SiO_2, SrO, BaO, Cr_2O_3, K_2O, MnO. Na^+ and Cl^- ratios were found to be very high. K_2O value of the main oxides was found to be very low. The lowest Na (33.70%) and Cl (52.10%) values were determined in the Nkt-3 sample and the highest Na (38.30%) and Cl (57.70%) values were determined in Nkt-5 sample. As a result of the alteration occurring in the ophiolitic rocks at the base of the basin, the Mg formed is transported to the sedimentation environment with the effect of groundwater and surface waters, and the magnesite can precipitate at the increasing water level in the lake. In the Sabkha environment, the Halite mineral can be crystallized both within the matrix and individually. Halite can also be deposited by evaporation in an aqueous environment in the lake water (Sönmez 2014). In the field of investigation; Halite (NaCl), Gypsum ($CaSO_4$), Anhydride ($CaSO_4.2H_2O$), Globerite ($CaNa_2$ $(SO_4)_2$), Tenardite (Na_2SO_4) minerals were determined (Horasan and Ozturk 2019).

In the Matrix, clay minerals, Quartz, Serpentine group minerals and minerals of detritic origin can be observed. The lake environment has been fed by both groundwater and above ground waters, due to seasonal changes. Ion enrichment in the lake (Na^+, Cl^-) sedimentation took place as a result of evaporation in the lake during the arid period of the lake and the claystone was deposited in the open conditions in short and long periods in the lake. Successive formation of Halite, anhydrite, and plaster occurred due to the chemistry and temperature of the medium due to seasonal changes (Sönmez 2014). Samples of gypsum ($CaSO_4.2H_2O$) and anhydrite ($CaSO_4$) found in clay bands with glassy brightness and fibrous surfaces were taken at the examination area and chemical analyses were done with XRF (Table 2, 3.)

The dominant gypsum observed in the evaporite basins can be grouped under two headings as primary and secondary. The concept of primary gypsum; sedimentologically formed in the lake or mud plaster undergoes no diagenetic changes that have been used for the preservation of the primary physical and textural properties (Helvacı 2002). Secondary gypsum was generally formed by the intake of anhydrides. There are three formation mechanisms of gypsum formation by anhydride hydration.

These three formation mechanisms;

- Hydration of anhydride into gypsum by taking water into the crystal cage
- Hydration via Basanite series (Step method)

-Formation of plaster by redissolution of anhydrite

The formation of plaster is possible by direct ingress of water directly into the anhydride crystal lattice. The plaster formed in this way is alabastrine and is called secondary gypsum (Helvacı 2002).

Anhydride ($CaSO_4$) is generally characterized by its modular and electrolytic structures in the sabka environment. Since anhydrite minerals are not stable in surface conditions, they are converted to gypsum by the effect of meteoric waters (Helvacı 2002).

Table 1. Results of chemical analysis with XRF on samples taken from the field (Tois)

	Na	Cl	SO_3	Al_2O_3	CaO	MgO	Fe_2O_3	SiO_2	SrO	BaO	Cr_2O_3	K_2O	MnO
Unit	%	%	%	%	%	%	%	%	%	%	%	%	%
1	36.95	57.15	0.45	0.99	0.78	0.73	0.28	2.63	<0.010	<0.010	<0.010	0.12	<0.010
2	37.55	57.40	0.33	0.90	0.68	0.71	0.29	2.10	<0.010	<0.010	<0.010	0.098	<0.010
3	33.70	52.10	2.17	1.93	2.69	1.41	0.64	4.95	<0.010	<0.010	<0.010	0.20	0.010
4	36.75	56.05	0.63	1.05	0.90	0.88	0.40	3.20	<0.010	<0.010	<0.010	0.10	<0.010
5	38.30	57.70	0.18	0.75	0.58	0.40	0.18	1.75	<0.010	<0.010	<0.010	0.060	<0.010
6	34.90	53.61	2.18	1.40	2.35	1.12	0.45	3.68	<0.010	<0.010	<0.010	0.25	0.015
7	37.10	56.02	0.38	0.95	0.90	0.67	0.38	2.60	<0.010	<0.010	<0.010	0.10	<0.010
8	37.10	55.80	0.58	1.13	0.87	0.70	0.40	3.20	<0.010	<0.010	<0.010	0.12	<0.010

Table 2. XRF element results (Tois)

Component	Gypsum (%)	Anhydride (%)
O	49.3	48.7
Ca	27.8	28.6
S	20.1	20.6
C	1.52	1.27
Si	0.66	0.40
Al	0.32	0.14
Fe	0.16	0.091
Mg	0.088	0.078
K	0.048	0.041
Sr	0.035	0.020

Table 3. XRF Anaoxide analysis results (Tois)

Component	Gypsum (%)	Anhydride (%)
SO_3	51.4	52.5
CaO	40.4	41.3
CO_2	5.64	4.72
SiO_2	1.45	0.887
Al_2O_3	0.629	0.270
Fe_2O_3	0.240	0.116
MgO	0.149	0.113
K_2O	0.0604	0.0695
SrO	0.0439	0.0259

3.2. Evaluation of ICP-OES Results

The chemical composition of the brine is linked to the geology of the drainage basin surrounding the lake. Ions concentrated in the lake by evaporation are transported in solutions by streams and groundwater as a result of the decomposition of the surrounding rocks (Hüseyinca 2015). Jones and Deocampo (2003) explained the degradation reactions of certain rocks that are effective in the source areas and their relationships with the main anions and cations. For example, limestones Ca and HCO_3, dolomites Mg, magmatic and metamorphic rocks, depending on the composition of silica-rich Ca-Na-HCO_3, pyrite shales from sulfur-rich waters, hydrothermal waters are rich in SO_4 and basic and ultrabasic rocks are rich in Mg-HCO_3. Apart from these physical factors, another factor affecting the chemistry of lake water is the chemical precipitation and dissolution reactions, because the minerals that reach saturation and precipitate in saltwater decrease the concentration of ions that make up them and cause the saltwater to be enriched by other ions. Conversely, water increases in the lake can dissolve the minerals that have settled and change the chemistry of the saltwater (Smoot and Lowenstein 1991).

The number of heavy metals such as Pb, Cd, Hg, As, Fe, Cr, Al and Zn were determined elementally on 2 samples selected from the collected samples. Hg and Cd could not be detected. According to the Turkish food security communiqué, As, Hg, Pb, and Cd values are well below the limit values (Table 4).

Table 4. ICP - OES Results (Tois)

NICP-1			NICP-2			
H.M	Unit	Result	H.M	Unit	Result	TFC limit Value
Pb	mg/kg	0,018	Pb	mg/kg	0,016	2 mg/kg
Cd	mg/kg	-	Cd	mg/kg	-	0.5 mg/kg
Hg	mg/kg	-	Hg	mg/kg	-	0.1 mg/kg
As	mg/kg	0,067	As	mg/kg	0,058	0.5 mg/kg
Fe	mg/kg	40,4	Fe	mg/kg	38,9	
Cr	mg/kg	0,14	Cr	mg/kg	0,12	
Al	mg/kg	2.04	Al	mg/kg	2,8	
Zn	mg/kg	18,3	Zn	mg/kg	17,6	

3.3. Evaluation of SEM - EDX Results

On the greenish, gray-colored Halite (salt) samples taken from the study area, the presence of Cl, Na, O, Si, Mg, Al, Fe, Ca, K and Ti were determined by scanning electron microscopy (Figure 2a, b, c). Another sample from the study area, transparent, halide (salt) sample was found only Na and Cl (Figure 3). The passage of gray-green clays and salt crystals within the body of salt were examined and the type and percentage of the elements found in the cellar were determined (Fig. 2a, b, c). Na (sodium) and Cl (Chlorine) were detected by SEM-EDX analysis (Fig. 3a, b, c) of the clear halite (salt) sample without any pollution.

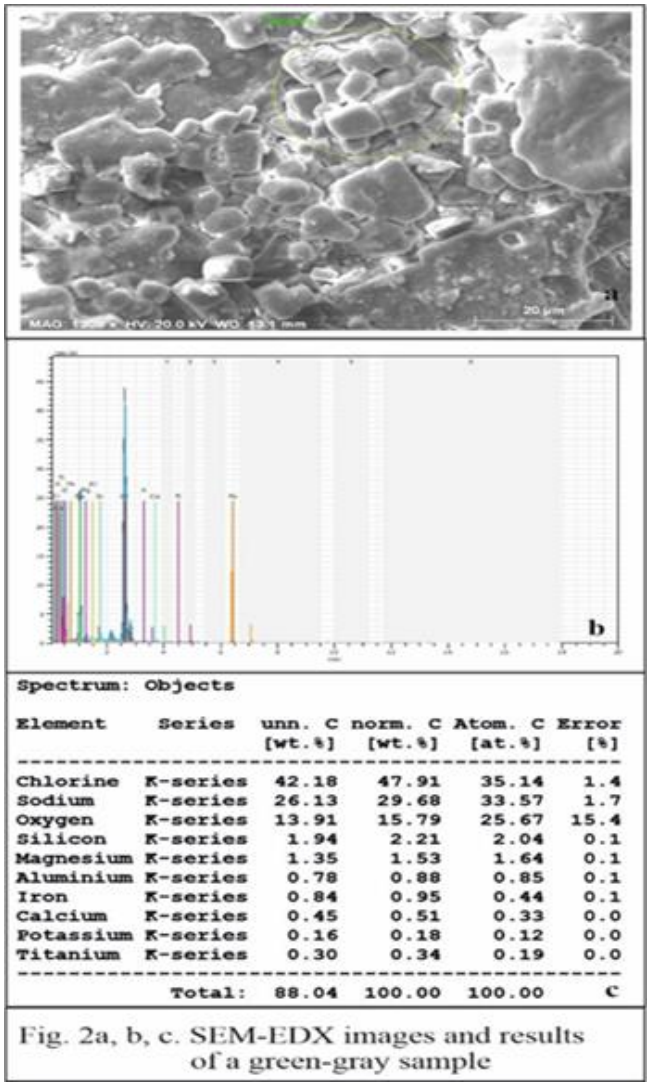

Figure 2. SEM-EDX images and results of a green-gray sample

4. CONCLUSION

The studies in the study area, the previous studies and the analyzes on the sample taken were evaluated together. It was observed during the field studies that the Upper Eocene-Oligocene aged red-colored sandstones and claystone contain small-sized anhydrite and rock salt lenses, Oligocene aged rock salt deposits over this unit and these rock salts are under a gypsum-clay alternation. In the analysis made in greenish-gray colored salt samples, some foreign elements such as Al, Fe, Cr, Zn, Mn, Sr, and Ba have been determined and in some periods of sedimentation depending on the decomposition, transport, and alteration of the rock groups formed by the volcanism of these elements. moved into the crystal structure. Pure transparent Halite (Salt) bands were detected in the alternating rock salt deposits and no other elements other than Na and Cl were found in the SEM - EDX studies. According to the Turkish Food Codex Salt Communiqué, the heavy metals are below the limit value in the chemical analysis results of these samples. Heavy metals were evaluated in terms of their quantities in the body. The values (table 4) were compared according to the Turkish Food Codex Salt Communiqué. It was observed that the amount of heavy metal was below the limit value.

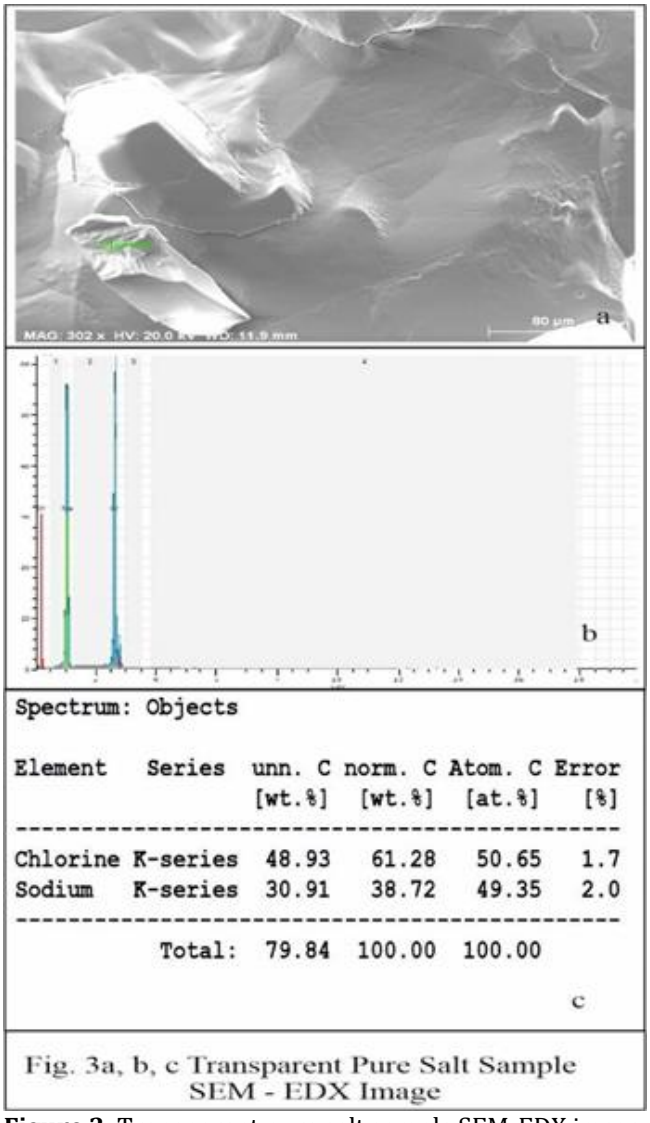

Figure 3. Transparent pure salt sample SEM-EDX image

ACKNOWLEDMENT

The authors thank Safir Tuz A.Ş support this research. As well, we express their sincere gratitude to Asil Kasım Baydar for his frequent discussions and suggestions during the study.

REFERENCES

Altay T (2010). Investigation of mineralogic-geochemical properties and industrıal raw material potential of Neogene aged sedimentary units between Bor-Ulukışla Towns. PhD thesis, Selcuk University, Konya (in Turkish).

Birgili Ş, Yoldaş R & Ünalan G (1975). Geology and petroleum opportunities of Çankırı-Çorum basin. MTA Report, no: 5621. (in Turkish)

Caglar S (2015). İnsanlık tarihini değiştiren bir baharat: Tuz. https://dunyalilar.org/insanlik-tarihini-degistiren-bir-baharat-tuz.html/, Accessed date: 14 September 2019

Dellaloğlu A A (1973). Detail geology and oil possibilities of Iskilip mercury and its south and southwest, MTA Report, no: 6132. (in Turkish)

Donat I (2016). Türkiye'de tuz sektörü. https://www.bloomberght.com/yorum/irfan-donat/1938663-turkiyede-tuz-sektoru, Accessed date: 14 January 2020

Dönmez M, Bilgin Z R, Akçay A E, Kara H, Yergök A F & Esentürk K (2005). MTA 1/100.000 scale Turkey Geological Map series, Kırşehir - İ31-İ32 threader: No: 46-47. MTA General Directorate, Ankara

Erdoğan B, Akay E & Uğur M S (1996). Geology of the Yozgat Region and evolution of the collisional Çankırı Basin. International Geology Review, 38(9), 788-806. DOI: 10.1080/00206819709465362

Eugster H P & Hardie L A (1978). Saline Lakes. New York, NY, Springer-Verlag, 237-293. ISBN: 978-1-4757-1152-3

Helvacı C (2002). Evaporites geology and Turkey Borate Depoists course notes. Chamber of Geological Engineers Page, Ankara. (in Turkish)

Horasan B Y & Ozturk A (2019). Geochemical Properties of Salt Deposits Around Delice (Kırıkkale). CISET - 2nd Cilicia International Symposium on Engineering and Technology, Mersin, TURKEY, 562-564.

Hüseyinca M Y (2015). Mineralogical and geochemical characteristics of the sediments in salt lake and the close vicinity. PhD Thesis, Selçuk University, Konya, Turkey (in Turkish)

Jones B F & Deocampo D M (2003). Geochemistry of saline lakes. Treatise on Geochemistry, 5, 393-424, ISBN 0-08-043751-6

Kara H & Dönmez M (1990) MTA 1 \ 100000 scale geological map of Turkey qualified series, Kırşehir-G 17 threader. MTA General Directorate, Ankara.

Kara H (1991) MTA 1/100 000 scale geological map of Turkey qualified Series, Kırşehir - G 18 threader. MTA General Directorate, Ankara.

Karadenizli L (2011). Oligocene to Pliocene palaeogeographic evolution of the Çankırı-Çorum Basin, Central Anatolia, Turkey. Sedimentary Geology, 237, 1-29. DOI: 10.1016/j.sedgeo.2011.01.008

Kazancı N & Varol B (1990). Development of a mass flow-dominated fan-delta complex and associated carbonate reefs within a transgressive Paleocene succession, Central Anatolia, Turkey. Sedimentary Geology, 68(4), 261–278. DOI: 10.1016/0037-0738(90)90014-K

Norman T (1972). Stratigraphy of Upper Cretaceous — Lower Tertiary strata of Yahşıhan area, east of Ankara. Bulletin of the Geological Society of Turkey, 15(2) 180–276.

Özgüner A M & Kızıldağ İ (2015). Geological survey and research of natural gas storage facilities of KIAS rock salt deposit in Kırıkkale-Sekili evaporite basin. KİAŞ Technical Report, Ankara. (in Turkish)

Seyitoğlu G, Kazancı N, Karakuş K, Fodor L, Araz H & Karadenizli L (1997). Does continuous compressive tectonic regime exist during Late Palaeogene to Late Neogene in NW Central Anatolia, Turkey? Preliminary observations. Turkish Journal of Earth Sciences, 6, 77-83.

Seymen İ (1981). Stratigraphy and metamorphism of the Kırşehir massif around Kaman (Kırşehir). Geological Bulletin of Turkey, 24 (2), 7-14.

Smoot J P & Lowenstein T K (1991). Chapter 3: Depositional environments of nonmarine evaporites. Developments in Sedimentology, 50, 189-347. DOI: 10.1016/S0070-4571(08)70261-9

Sönmez İ (2014). Glauberite-Halite Association in Bozkır Formation (Pliocene, Çankırı-Çorum Basin, Central Anatolia, Turkey). Bulletin of the Mineral Research and Exploration, 149, 153-175.

Tepecik A (2007). Investigation of geology and salt – petroleum relationships around the Bayat Area, Çankırı – Çorum Basin. MS Thesis, Ankara Universty Graduate School of Natural and Applied Sciences, Ankara, Tukey. (in Turkish)

Tüysüz O & Dellaloğlu A A (1992). Tectonic units of Çankırı basin and geological evolution of the basin. Congress of Turkey 9.Petroluem, 333-349.

U.S. Geological Survey (2018). Mineral commodity summaries 2018. U.S. Geological Survey, 200 p. DOI: 10.3133/70194932.

U.S. Geological Survey (2019). "Mineral commodity summaries 2019. U.S. Geological Survey, 200 p. DOI: 10.3133/70202434.

Ünalan G & HARPUT B (1983). Investigations of the source rock within Upper Cretaceous and Lower Tertiary deposits at the western margin of the Çankırı basin (Central Turkey). Bulletin of the Geological Society of Turkey, 26, 177-186.

Varol B, Şen S, Seyitoğlu G, Kazancı N, Karadenizli L, Gül A, Ertan H, Antoine P O, Saraç G, Alçiçek M C (2004). Oligo-Miocene biostratigraphy and filling evolution based on mammalian fossils of the western and southern parts of Çankırı-Çorum basin. MTA report no: 10706, Ankara.

Turkish Journal of Engineering

https://dergipark.org.tr/en/pub/tuje

e-ISSN 2548-0960

Assessing the spatial accuracy of UAV-derived products based on variation of flight altitudes

Semih Sami Akay [*1], **Orkan Özcan** [2], **Füsun Balık Şanlı** [1], **Bülent Bayram**[1], **Tolga Görüm**[2]

[1]*Yıldız Technical University, Faculty of Construction, Geomatics Engineering, İstanbul, Turkey*
[2]*Istanbul Technical University, Eurasia Institute of Earth Sciences, İstanbul, Turkey*

Keywords
Unmanned aerial vehicle
Digital surface model (DSM)
Point cloud
Volumetric analysis

ABSTRACT

Unmanned Aerial Vehicles (UAVs), which can carry a variety of payloads, and be operated automatically or manually with ground control stations. Nowadays, UAVs can make photogrammetric flight plans and obtain photogrammetric data with existing sensor systems. Automatic data acquisition processes provide lower cost, and high spatial and temporal resolution images in a short period of time compared to other measurement methods. As a result, orthomosaics, dense point clouds and digital surface models (DSMs) are produced and these UAV-derived data are used in various disciplines such as constructions, geomatics, earth sciences, etc. In this study, the same flight plans were realized with an UAV at different altitudes and all aerial images were obtained with the same integrated digital camera. As a result of the processing of images acquired from different altitudes, orthomosaics, DSMs and point cloud were produced. In this study, it is aimed to compare the length, areal and volumetric differences of a small geostationary object. Ground control points (GCPs), which were collected by RTK-GPS (Real-Time Kinematic) in conjunction with the flight integrated into data production process in order to highly accurate product. Ultimately, cross-correlation has been done with the produced data and the terrestrial measurement. Results show that the dimension of the object depend on the flight altitude as expected, however the volumetric changes vary due to the uncertainties in the raw point cloud data.

1. INTRODUCTION

Unmanned aerial vehicles (UAVs) can produce surface data with low cost, temporal and spatial resolution data compared to terrestrial and remote sensing methods. UAVs can provide a lot of information related to the surface with the various sensors they have or can be integrated. When UAVs photogrammetric techniques are also compared with satellite and aerial survey, UAVs can provide very high resolution data quickly with high accuracy and low cost (Akar 2017; Eltner et al. 2017; Psirofonia et al. 2017; Thumser et al., 2017).

UAV photogrammetric studies can be performed with automatic or semi-automatic flight plans. Aerial photographs overlapping with flight plans are obtained and photogrammetric processing steps are performed. Point cloud, orthomosaics and DSMs are produced rapidly and accurately by taken photographs from UAVs, dimensions of objects and surface are performed so that information about surface and objects can be obtained (Pérez et al. 2013; Tampubolon and Reinhardt 2015).

DSMs and 3D object models were produced with high accuracy as a result of processing aerial photographs obtained with UAV, which were used to model historical artifacts and calculate the volume of the earth surface (Ulvi and Toprak 2016; Ulvi 2018; Şasi and Yakar 2018). The dimensions of measurements can be performed with different data obtained at different altitudes with UAVs. The area and volume of the objects on the surface can be calculated with the point cloud, DSM and 3D models produced with and without GCPs. Therefore, the measured values of dimensions are very close to the actual values. It was observed that the differences vary according to the objects. In addition, the error values of large objects were found to be in the order of centimeters. As a result of the volumetric analysis, it could be seen that similar results were obtained in the point cloud. In addition, it was seen that the volumetric measurements could be obtained close to the actual values in the analyzes performed with the 3D models. (Akay and Ozcan 2017; Ab Rahman et al. 2017; Stalin and Gnanaprakasam 2017).

* **Corresponding Author**

*(semih.sami.akay@std.yildiz.edu.tr) ORCID ID 0000 – 0002 – 7367 – 8555
(ozcanork@itu.edu.tr) ORCID ID 0000 – 0002 – 7485 – 6157
(fbalik@yildiz.edu.tr) ORCID ID 0000 – 0003 – 1243 – 8299
(bayram@yildiz.edu.tr) ORCID ID 0000 – 0002 – 4248 – 116X
(tgorum@itu.edu.tr) ORCID ID 0000 – 0001 – 9407 – 7946

Research Article / DOI: 10.31127/tuje.653631

Cite this article

Akay S S, Ozcan O, Şanlı F B, Bayram B & Gorum T (2021). Assessing the spatial accuracy of UAV-derived products based on variation of flight altitudes. Turkish Journal of Engineering, 5(1), 35-40

Received: 01/12/2019; Accepted: 21/01/2020

Therefore, UAVs can provide data at any time within specified flight rules and weather conditions. The combination of terrestrial control points and UAV data enables high accuracy data generation. However, with the new generation UAV with PPK (Post-Processed Kinematic), or RTK (Real-Time Kinematic) system, no ground measurements are required to produce high resolution data. Recent studies showed that when the photogrammetric studies performed with UAVs, point cloud data, orthomosaic and DSM can be produced. Therefore, environmental and temporal change analyzes can be performed (Akay and Ozcan 2017; Eltner et al. 2017; Ozcan and Akay 2018a; Ozcan and Akay 2018b Rusnák et al. 2018).

2. STUDY AREA

In this study, UAV flight altitudes have been changed to investigate the accuracy of UAV data and the changes in the dimension of the small green objects was examined (Fig. 1). The study was carried out with a green box in the form of a rectangular prism of small size located on river drainage system. The study area is located in the Büyük Menderes basin located within the borders of Aydın province in the Aegean Region. Figure 1 shows the associated study area on the river drainage system and the ground control points (GCPs) used in the study.

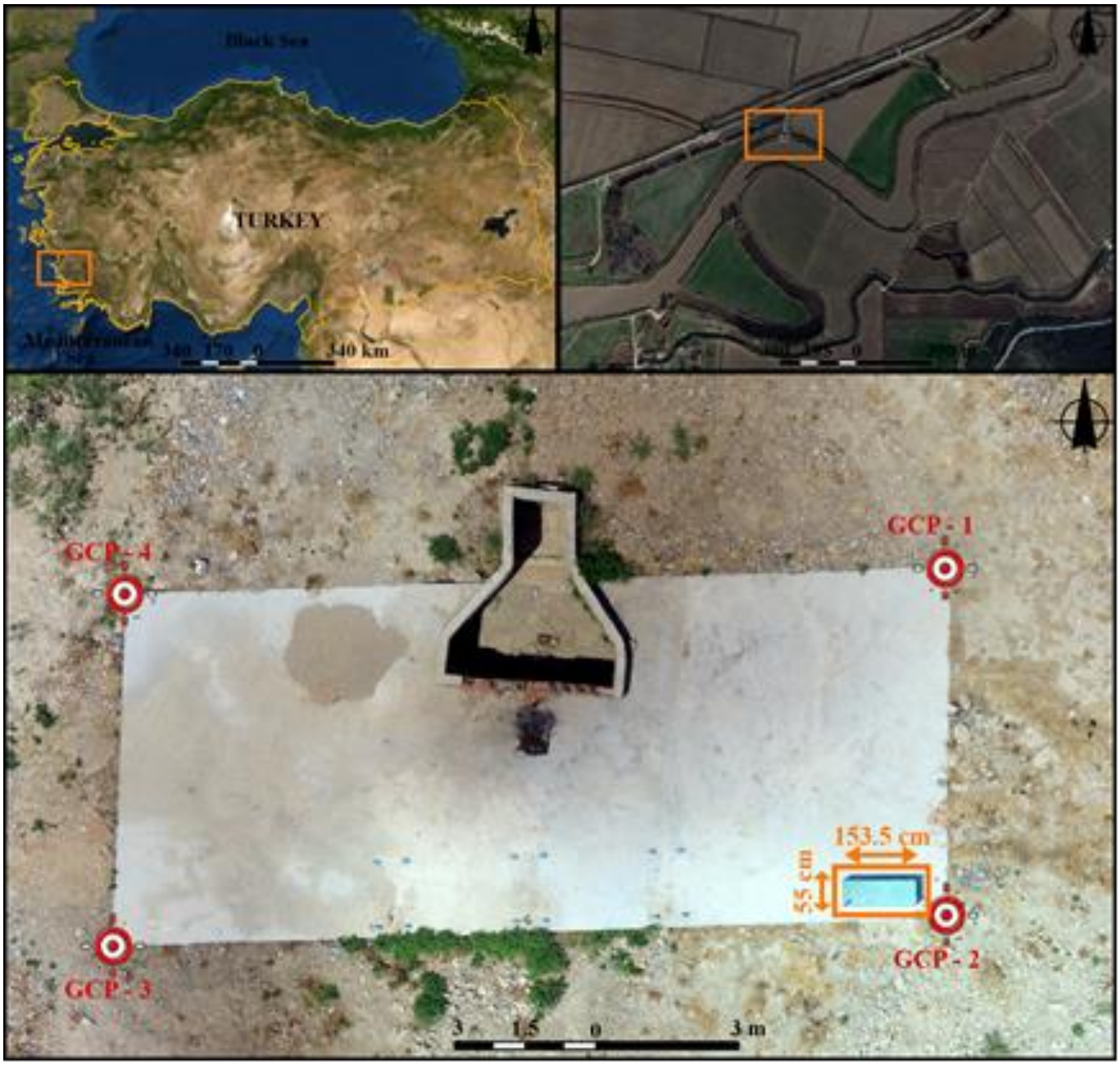

Figure 1. Aerial photo of the study area and GCPs

3. DATASETS and METHODS

In the study, different data were produced by performing flights with an UAV and these data were compared with the actual dimension, area and volume measurements of an object. The flowchart of the processing steps is shown in Figure 2.

UAV flights were performed according to the same flight plan parameters at different altitudes. The DJI Phantom 3 Pro UAV used in the study, which has an

integrated GPS / Glonass system and a 12.76 MP digital camera, is about 1.5 kg. When the integrated digital camera specifications are examined, it has FOV 94°20 mm (35 mm format equivalent) lens, ISO Range is 100-1600 for photographs and image size of camera is 4000×3000. UAV flights were performed at altitudes of 10 m, 40 m, 70 m and 100 m. Table1 shows the UAV flight parameters and the errors of each flight performed at different altitudes. Flight plans were made according to the legal limits and environmental factors (power pole, tree, base station, etc.). Depending on the coverage area, as the flight altitude increased, the number of photographs decreased and 117 images were acquired in the study area.

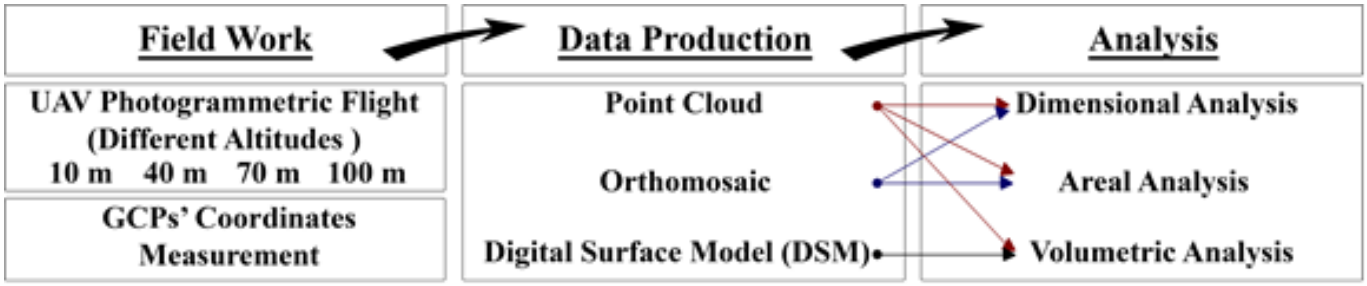

Figure 2. Flowchart of the processing steps

Table 1. Specifications of the UAV data

Flight Alt. (m)	# of images	Overlap ratio (%)	# of GCPs	Image coor. error (pix)	RMSE (m)
10	59	85-85	4	0.203	0.009
40	31	85-85	4	0.192	0.006
70	15	85-85	4	0.190	0.014
100	12	85-85	4	0.198	0.021

GCPs were homogeneously selected from the corners of the study area and the GCPs' coordinate measurements were performed by RTK method after the UAV's flights. GCP measurements were combined with UAV-derived data processing to produce data with high accuracy. Table 2 shows the coordinates of the measured GCPs.

Table 2. Coordinates of the GCPs

GCP #	X (m)	Y (m)	Z (m)
1	530573.296 ± 0.026	4151401.272 ± 0. 026	39.385 ± 0.026
2	530573.206 ± 0.026	4151393.874 ± 0.026	39.321 ± 0.026
3	530555.596 ± 0.032	4151393.286 ± 0.032	39.279 ± 0.032
4	530555.949 ± 0.026	4151400.648 ± 0.026	39.285 ± 0.026

The X, Y and Z coordinates of objects in aerial photographs were calculated with GCPs, external orientation parameters and key points after the bundle block adjustment. Then, the root mean square error (RMSE) values were calculated by square root of the sum of the error of each point (ei) divided by total number of GCPs (N) in all directions for each flight to produce data with high accuracy (Eq. (1) (Pix4D 2020). The calculated RMSE values are shown in Table 1. Besides, the image coordinate error values were less than half pixel value.

$$\text{RMSE} = \sqrt{\frac{\sum_{i=1}^{N}(ei)^2}{N}} \quad (1)$$

In this study, point cloud, DSMs and orthomosaics were produced from the images obtained by an UAV. The length, areal and volumetric dimensions of the small green object in the point cloud, DSM and orthomosaic were compared with the actual dimensions of the object measured locally. Nowadays, UAV photogrammetry method provides low cost and time advantage compared to remote sensing techniques. The UAV photogrammetry method allows the production of high resolution point cloud, DSM and orthomosaic data from sequential series of photographs with the Structure-from-Motion (SfM) method. The SfM method enables the matching of objects in the UAV's images by arranging the camera parameters and their positions. By matching the objects in the images and generating the tie points, a spare dense point cloud is produced. Dense point cloud is produced by densification of spare point cloud data. As a result of producing three dimensional polygon network model with dense point cloud, DSM and orthomosaic productions are realized respectively (Snavely et al. 2008). Prior to the image matching process, GCPs, which are measured in the study area are integrated into the system for each flight at different altitude to produce highly accurate last product. Table 3 shows the specifications of the data produced at different altitudes in the study. The actual length measurements and area values of the upper surface of the green box object were calculated and compared with orthomosaics and point cloud data. However, both the length and area values were calculated by calculating the upper surface length measurements of the green box over the orthomosaics. In the point cloud data, lengths were calculated by taking sections on the point cloud data of green box in order to determine the width and length measurements of the green box.

In the point cloud data, lengths were calculated by taking sections on the point cloud data of green box in order to determine the width and length measurements of the green box. Comparisons of actual length and area values were made with different data produced with different UAV flight altitudes. Figure 3 shows cross and length sections of point cloud data produced at different altitudes. It was seen that the small size of the object cannot keep its rectangular shape as the UAV flight

altitude increases and the rolling of the edges starts in the point cloud data. Therefore, it was seen that differences occur in each measurement.

Table 3. Dataset resolutions and point cloud densities of each flight plan

Flight Alt. (m)	Dense of Point Cloud (m^3)	DSM Spatial Res. (m)	Ortomosaic Spatial Res. (m)
10	348395.00	0.004	0.004
40	6233.86	0.018	0.018
70	1026.81	0.031	0.031
100	383.10	0.044	0.044

The width, length and area calculations performed on the point cloud and orthomosaic data produced with images obtained at different altitudes were shown in Table 4. When the actual width and length of the green box were compared with orthomosaic and point cloud data, it was observed that the error value was increased with the altitude of flight. However, the error value was found to be between 0.1 and 2.4 cm. In addition, it was observed that the data at consecutive altitude had closer measurements. Besides, the width and length measurements obtained from point cloud data had closer values to orthomosaic measurements.

When the area measurements of the object were compared, it is seen that the data of the flight performed at an altitude of 10 m gave a closer result to the actual size. In addition, when the areal values of the data produced from different altitudes were compared, it was seen that they had differences between 0.34% and 3.7% proportional to the actual dimension. In areal measurements, it was observed that point cloud data approached actual measurements more than orthomosaic data. As a result, it was seen that the closest value to the actual areal value belongs to the point cloud obtained at an altitude of 10 m as expected.

The actual volume value of the green box was compared with the point cloud and DSM data of different altitudes. Figure 4 shows DSM and orthomosaic images of the green box produced at different altitudes.

It was observed that the small size of the object could not keep its quadrilateral shape and the height of the object decreased with increasing UAV flight altitude.

The volume calculations of the point cloud and DSM data of different altitude and the differences between the actual volume value were shown in Table 5. When the volume values of the green box were examined, it was seen that the error value of the volume value increased as the altitude of flight increased and this error value was between -32,262 cm^3 and 186,948 cm^3. The closest value to the actual volume values was found in the point cloud and DSM data of the flight performed at an altitude of 10 m.

When the actual volume values and the point cloud data produced from different altitudes were compared, the error rate were varying between 7% and 17%, respectively. This value was found to be between 13% and 46% actual value and DSM data, respectively. When the volume values were compared, it was seen that the point cloud data gave more accurate values than the DSM data. Volumetric differences between the two data varied between 88,257 cm^3 and -136,812 cm^3.

Figure 5 shows the change of the areal and volumetric values of the green box with graphs. As the areal measurements are examined, it could not be seen that there was a decrease or increase in direct proportion with altitude between the actual value and the point cloud and orthomosaic measurements. In the orthomosaic data at an altitude of 40 m, the areal value above the actual value was obtained. Similarly, the areal value in the point cloud data obtained at an altitude of 70 m was seen as a value above the actual value. In addition, it was observed that the point cloud data were found to be closer to the actual areal value than the orthomosaic data.

The volumetric analysis results showed that both the point cloud and DSM data have different values compared to the actual volume value as the altitude increases. The volumetric values at 10 m altitude were higher than the actual measurements in both data types.

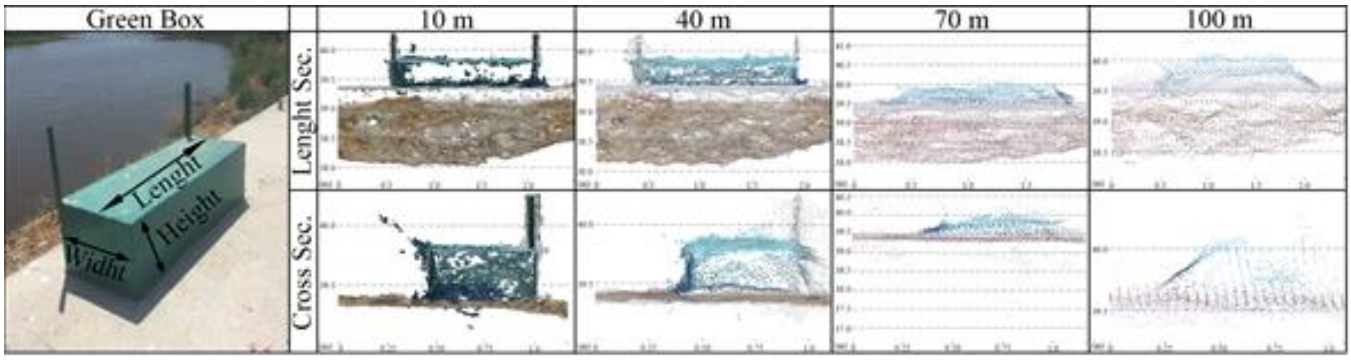

Figure 3. Representation of cross and length sections of point clouds

Table 4. Dimensions and area values of orthomosaic and point cloud

Flight Alt. (m)	Orthomosaic						Point Cloud					
	Width (cm)	Length (cm)	Area (cm^2)	Δl (cm) ΔW	Δl (cm) ΔL	ΔS (cm^2)	Width (cm)	Length (cm)	Area (cm^2)	Δl (cm) ΔW	Δl (cm) ΔL	ΔS (cm^2)
Actual Dim	55.0	153.5	8,442.50	-	-	-	55.0	153.5	8,442.50	-	-	-
10	54.4	152.9	8,317.76	-0.6	-0.6	-124.74	54.6	153.6	8,386.56	-0.4	0.1	-55.94
40	55.8	152.8	8,526.24	0.8	-0.7	83.74	54.6	153.2	8,364.72	-0.4	-0.3	-77.78
70	53.7	151.3	8,124.81	-1.3	-2.2	-317.69	56.5	152.4	8,610.60	1.5	-1.1	168.1
100	53.7	150.9	8,103.33	-1.3	-2.6	-339.17	53.4	150.6	8,402.04	-1.6	2.9	-40.46

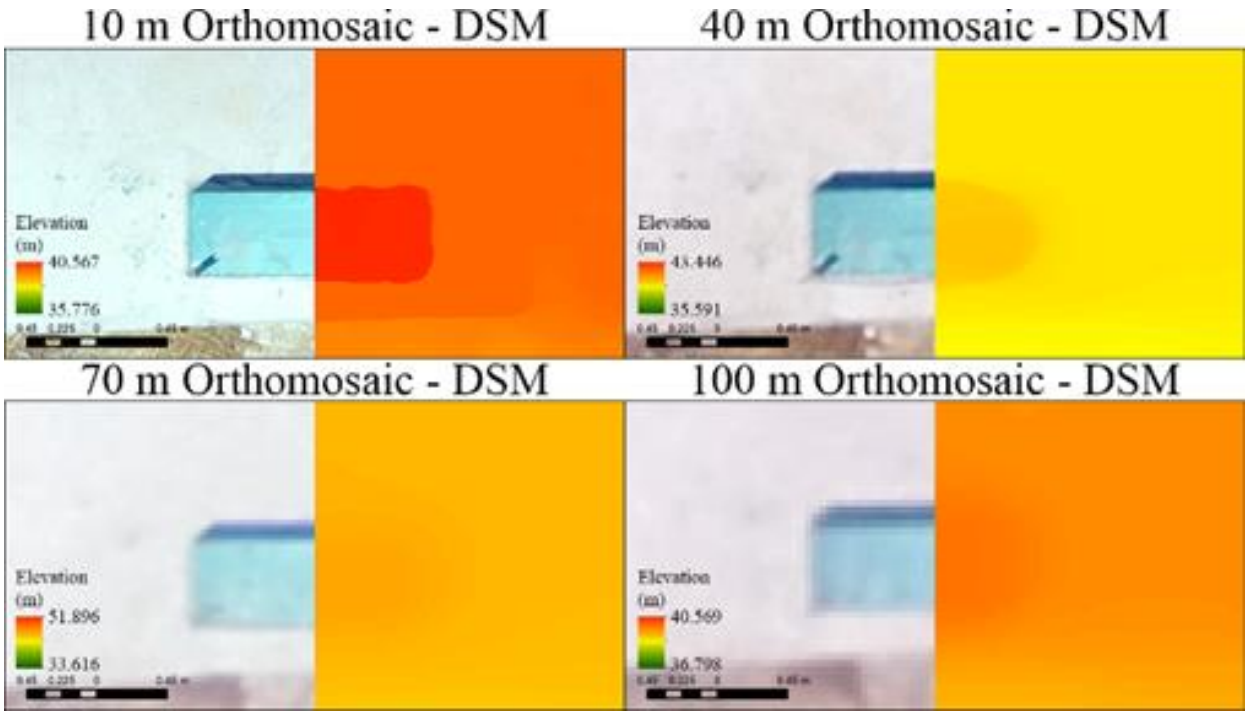

Figure 4. Representation of green box with orthomosaic and DSM data

Table 5. Volume values of point clouds and DSMs

Flight Elevation (m)	Point Cloud		DSM		PC-DSM (cm³)
	Volume (cm³)	ΔV (cm³)	Volume (cm³)	ΔV (cm³)	
Actual Volume			404,395		
10	436,657	32,262	460,390	55,995	-23,733
40	388,612	-15,783	286,180	-118,215	102,333
70	351,233	-53,162	240,900	-163,495	110,333
100	339,400	-64,995	217,447	-186,948	121,953

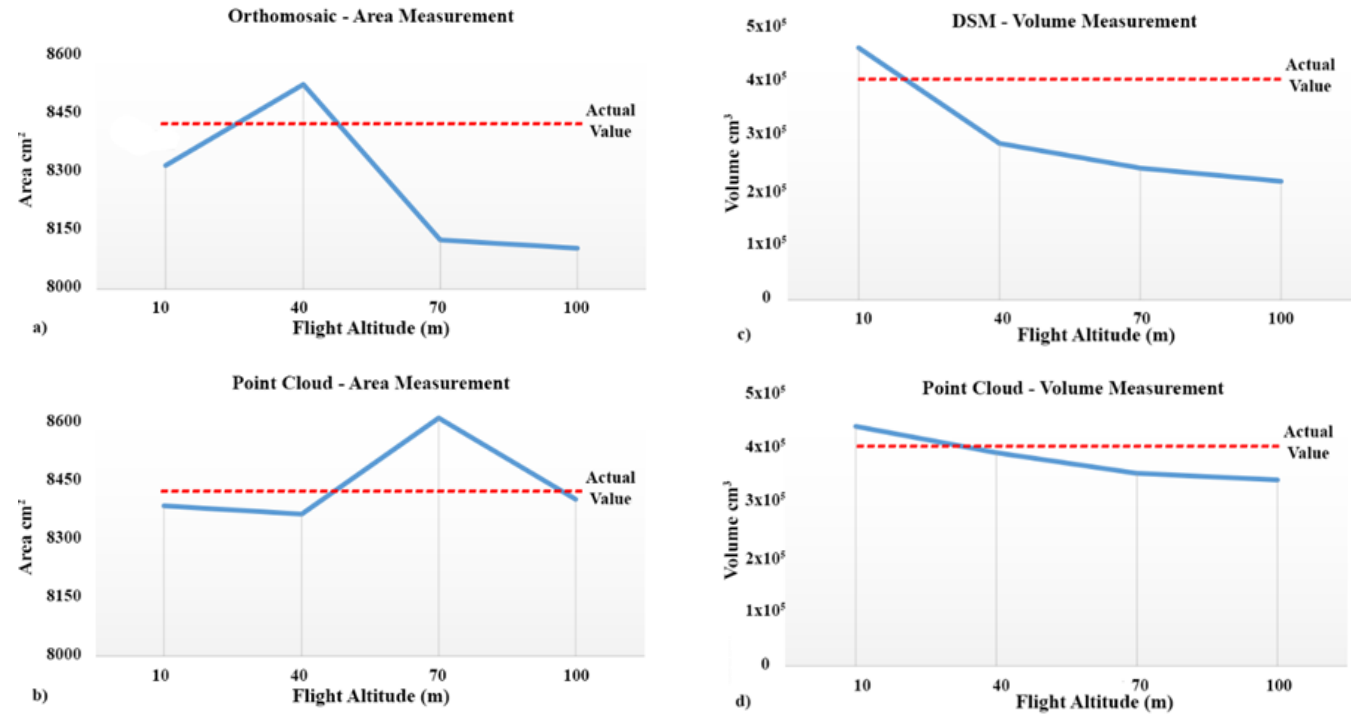

Figure 5. Change graphs of measurements depending on UAV altitude; a) Orthomosaic - area measurement, b) Point cloud - area measurement, c) DSM - volumetric measurement, d) Point cloud - volumetric measurement

5. CONCLUSION

In this study, the actual width, length, area and volume values of a fixed small green box on the river drainage system were compared with the data obtained from UAV flights at different altitudes. Point cloud, DSM and orthomosaic data of the green box were produced in order to make comparisons between different data models and to analyze width, length, area and volume

value. Herewith, in the comparison of UAV-derived dimensions with the actual values, it was observed to be similar in all flights. However, the best volumetric similarity achieved only at the lowest flight altitude. As flight altitude increased, it was seen that the volume values were distant from the actual value. Besides, it has been found that small objects could not keep their shape as the flight altitude increases. It can also be evincible that the point cloud data maintain the object shape better the DSM.

Consequently, UAV data can be used in width, length and area calculations of small objects, but UAV-derived point cloud data should be purified before using in volumetric calculations depending on the error rate determined in centimeters. Recently, UAVs were used in various projects instead of the traditional photogrammetry methods due to their low cost, practicality and capabilities. In the near future, it is not hard to estimate that UAVs will allow users to get last products without any uncertainties with the development of various payloads and processing techniques.

REFERENCES

Ab Rahman A A, Abdul Maulud K N, Mohd F A, Jaafar O & Tahar K N (2017). Volumetric calculation using low cost unmanned aerial vehicle (UAV) approach. IOP Conference Series: Materials Science and Engineering, 270. DOI: 10.1088/1757-899X/270/1/012032.

Akar A (2017). Evaluation of accuracy of DEMs obtained from UAV-point clouds for different topographical areas. International Journal of Engineering and Geosciences, 2(3), 110-117. DOI: 10.26833/ijeg.329717

Akay S.S. and Ozcan O. (2017). Volumetric Comparison of Uav-Based Point Clouds Generated from Various Softwares. International Symposium on GIS Applications in Geography and Geosciences, Çanakkale, Turkey, 240, ISBN : 978-605-4222-54-4.

Eltner A, Kaiser A, Abellan A & Schindewolf M (2017). Time Lapse Structure-From-Motion Photogrammetry for Continuous Geomorphic Monitoring. Earth Surface Processes and Landforms, 42(14), 2240–2253, DOI: 10.1088/1757-899X/270/1/012032.

Ozcan O & Akay S S (2018a). Modeling Morphodynamic Processes in Meandering Rivers with UAV-Based Measurements. International Geoscience and Remote Sensing Symposium, Valencia, Spain, 7886-7889 DOI: 10.1109/IGARSS.2018.8518221

Ozcan O & Akay S S (2018b). Monitoring Hydromorphological Changes in Meandering Rivers via Multi-Temporal UAV-Based Measurements. AGU Fall Meeting, 10-14 December 2018, DOI: 10.13140/RG.2.2.10156.10886.

Pérez M, Agüera F & Carvajal F (2013). Low Cost Surveying Using an Unmanned Aerial Vehicle. International Archives of the Photogrammetry, Remote Sensing and Spatial Information Sciences, Volume XL-1/W2, DOI:10.5194/isprsarchives-XL-1-W2-311-2013.

Pix4D Support (2020), https://support.pix4d.com/hc/en-us/articles/203604125-How-are-the-GCP-Errors-defined-in-the-Quality-Report. Accessed date: 20 January 2020

Psirofonia P, Samaritakis V, Eliopoulos P & Potamitis I (2017). Use of Unmanned Aerial Vehicles for Agricultural Applications with Emphasis on Crop Protection: Three Novel Case-studies. International Journal of Agricultural Science and Technology, 5(1), 30-39. DOI: 10.12783/ijast.2017.0501.03.

Rusnák M, Sládek J, Kidová A & Lehotsky M (2018). Template for High-Resolution River Landscape Mapping Using UAV Technology. Measurement, 115, 139-151, DOI: 10.1016/j.measurement.2017.10.023.

Şasi A & Yakar M (2018). Photogrammetric modelling of Hasbey Dar'ülhuffaz (Masjid) using an unmanned aerial vehicle. International Journal of Engineering and Geosciences, 3(1), 006-011. DOI:10.26833/ijeg.328919.

Snavely N, Seitz S M & Szeliski R (2008). Modeling the World from Internet Photo Collections. International Journal of Computer Vision, 80(2), 189–210. DOI:10.1007/s11263-007-0107-3.

Stalin J.L & Gnanaprakasam R (2017). Volume Calculation from UAV based DEM. International Journal of Engineering Research & Technology (IJERT), 6(6), 126-128. DOI: 10.17577/IJERTV6IS060076.

Tampubolon W & Reinhardt W (2015). UAV data processing for rapid mapping activities. The International Archives of the Photogrammetry, Remote Sensing and Spatial Information Sciences, Volume XL-3/W3, 371-377. DOI: 10.5194/isprsarchives-XL-3-W3-371-2015.

Thumser P, Kuzovlev V V, Zhenikov K Y, Zhenikov Y N, Boschi M, Boschi P & Schletterer M (2017). Using structure from motion (SfM) technique for the characterisation of riverine systems - Case study in The Headwaters of the Volga River. Geography Environment Sustainability, 10(3), 31-43. DOI: 10.24057/2071-9388-2017-10-3-31-43.

Ulvi A & Toprak A S (2016). Investigation of Three-Dimensional Modelling Availability Taken Photograph of the Unmanned Aerial Vehicle; Sample of Kanlidivane Church. International Journal of Engineering and Geosciences, 1(1), 1-7, DOI:10.26833/ijeg.285216.

Ulvi A (2018). Analysis of the utility of the unmanned aerial vehicle (UAV) in volume calculation by using photogrammetric techniques. International Journal of Engineering and Geosciences, 3(2), 043-049. DOI:10.26833/ijeg.377080.

Turkish Journal of Engineering

https://dergipark.org.tr/en/pub/tuje

e-ISSN 2548-0960

The effects of including social factors in ride-matching algorithms on the performance and the quality of matches

Omer Faruk Aydın [*1], **Ilgin Gokasar** [1]

[1]*Bogaziçi University, Faculty of Engineering, Department of Civil Engineering, İstanbul, Turkey*

Keywords
Dynamic Ride-Sharing
Ride-Matching
Social Parameters
Transportation

ABSTRACT

Advancement in communication technologies has fostered alternative transport modes, such as ride-sharing. Ride-sharing aims to increase vehicle occupancy rates by matching riders with the drivers, who have empty seats on their vehicles and have similar routes and time schedules. Regarding to the success of a ride-sharing system, many researchers have been interested in efficient ride-matching algorithms. Ride-matching optimization problem is considered as NP-Hard Problem. In most of the ride-matching algorithms in the literature, to be able find matches at short notice some parameters were omitted. Hence, social characteristics and choices of participants, such as gender, age, employment status and willingness to socialize, were not included in many ride-matching algorithms. In this paper, the effects of including such factors in a ride-matching algorithm on the performance and the quality of the matches are investigated. Several ride-matching algorithms in the literature are simulated with randomly generated data. The simulation results show that when social factors are included the computation times and the quality of the matches increase significantly.

1. INTRODUCTION

Traffic congestion is one of the most important problems of modern cities. A significant shift from public transport towards private vehicles has been observed despite of increasing oil prices, parking problem and traffic congestion (European Environment Agency, 2005). On the other hand, while most private vehicles can transport 4 passengers, occupancy rates in private vehicles are very low. Occupancy rates in private vehicles were found to be 1.45 in European Countries in 2015, where this ratio is 1.42 in Germany, 1.3 in Netherlands and 1.58 in the UK (European Environment Agency, 2015). Many alternative transport modes have been studied such as ride-sharing to decrease traffic congestion by increasing occupancy rates.

Ride-sharing can be defined as matching riders who have no vehicle, with the drivers who have empty seats in their vehicles and have similar itineraries and time schedules. The history of ride-sharing can be traced back to the 1940s. At the time it was applied to conserve resources during World War II (Chan and Shaheen, 2012). Rapid growth in smartphone technologies and software packages made building an advanced ride-sharing system possible. Technological changes, such as app-based shared transportation, growth of cloud computing, advanced navigation services and data sharing, contribute the growth of innovative shared transportation services (Shaheen et al. 2018). In recent years, many leading ride-sourcing companies, such as Uber and Lyft, have increasingly focused on ride-sharing and they have launched smartphone applications (e.g., UberPOOL, ExpressPOOL, Lyft Line) to allow potential users finding matches and lowering their travel costs from 25% to 60% (Shaheen and Cohen 2018). These applications also enable dynamic route changes.

Building an automated ride-sharing system requires ride-matching algorithms, which can optimize matches between drivers and riders at short notice. Automated ride-matching, which optimally matches riders and drivers in real-time, plays a key role in ride-sharing (Agatz et al. 2012).

Dynamic ride-matching algorithms are very complicated systems and require a lot of attention of the researchers to overcome challenges. Ride-matching optimization problem has been considered as non-deterministic polynomial-time hard (NP-hard) problem (Gu et al. 2018; Qian et al., 2017; Herbawi and Weber, 2012). To be able to offer feasible solution approaches, some parameters such as social characteristics and

* **Corresponding Author**

*(faruk.aydin@tau.edu.tr) ORCID ID 0000 – 0001 – 9345 – 3997
(ilgin.gokasar@boun.edu.tr) ORCID ID 0000 – 0001 – 9896 – 9220

Cite this article

Aydın O F & Gokasar I (2021). The effects of including social factors in ride-matching algorithms on the performance and the quality of matches. Turkish Journal of Engineering, 5(1), 41-47

Research Article / DOI: 10.31127/tuje.657867

Received: 10/12/2019; Accepted: 05/01/2020

choices of the participants and/or some transportation modes, such as multiple rider or multi-hop, are omitted in these problems. There are some algorithms in the literature, which considers these parameters and modes, but most of these studies did not consider computation times.

To maximize system benefits in ride-matching algorithms, a previous study has proposed a novel approach to solve the ride-matching problem by modeling it using a traditional maximum-weight bipartite matching algorithm (Agatz et al. 2011). This algorithm is based on a single rider-single driver match. It is demonstrated that the weighted bipartite matching algorithm can be used for ride-matching; however, this algorithm requires long processing times because it calculates distance savings for each rider-driver pair to determine distance savings. The algorithm also omits multiple riders-single driver matches and ignores individual preferences to simplify the problem. This algorithm aims to increase the number of matches. This approach would not encourage people to be included in ride-sharing systems; even should users specify a deadline for their travel request, they do not like to wait long (Nielsen et al. 2015). This study is extended by adding social parameters as constraints, but solution approach for this problem is not offered (Ghoseiri et al. 2011).

A novel biosequence based ride-matching algorithm is created to optimize matches when considering participants' gender, age, employment status and social tendencies (Aydin 2019). This algorithm aims to maximize social compatibility between drivers and riders. A biosequence matching algorithm, namely Needleman-Wunsch algorithm, is used to check the similarity of routes of drivers and riders. First comes first served approach is utilized in this algorithm to solve the problem at short notice.

In this paper, several dynamic ride-matching algorithms in the literature are modelled with different settings, such as including social parameters, using different driver capacities and allowing multiple riders. To evaluate effects of including social parameters, these algorithms are simulated using the same data and performance of the algorithms and quality of matches are evaluated.

The remainder of the paper is structured as follows. In Section 2, the ride-matching algorithms are presented. Section 3 describes the details of the simulation process. In Section 4 and 5, performance of the ride-matching algorithms and quality of matches are analyzed. In Section 6, the findings of the study are summarized and directions for the future studies are discussed.

2. RIDE-MATCHING ALGORITHMS

2.1. Biosequence Based Ride-Matching Algorithm

The biosequence based ride-matching algorithm utilizes social parameters, namely gender, age, employment status and willingness to socialize. The objective function of this algorithm is to maximize social compatibility between drivers and riders (Aydin 2019).

To score social compatibility, a parameter, Joint Socialness Score (JSS), is defined. The JSS is calculated as follows:

$$\gamma^{rd} = x_g^{rd}\gamma_g^r\gamma_g^d + x_a^{rd}\gamma_a^r\gamma_a^d + x_w^{rd}\gamma_w^r\gamma_w^d + x_\sigma^{rd}\gamma_\sigma^r\gamma_\sigma^d. \quad (1)$$

In Eq. (1), weights of the social parameters of the rider (r) and feasible driver (d) are multiplied to calculate the JSS, γ^{rd}, The social parameters are gender weight γg, age weight γa, employment status weight γw and willingness to socialize weight $\gamma\sigma$. The variable x equals to positive one if the social characteristics are the same and negative one if they are different. Table 1 shows a sample calculation of the JSS.

Table 1. An illustrative example of the computation of JSS

	Driver *d1*		Rider *r2*			
	Char.	Factor	Char.	Factor	*x*	Scores
Gender	male	1	female	5	-1	-5
Age	18-25	3	25-40	4	-1	-12
Employment	TAU	4	TAU	4	1	16
Socialness	Yes	5	Yes	3	1	15
Total score						14

In Table 1, driver d1 represents a male driver with an age of between 18-25 who works at the TAU. Driver d1 claims that the weights of a rider's gender, age range and working place are one, three and four out of five, respectively. Driver d1 also claims that he wants to meet a new person on a ride with a weight factor of five. On the other hand, rider r1 represents a female rider with an age of between 25-40 who also works at TAU. Her weight factor for willingness to meet a new person on a ride is three. As mentioned previously, the variable x^{rd} equals to positive one if social characteristics of a driver and a rider are the same and negative one otherwise. In the example given in Table 1, x^{rd} is found to be negative one for gender and age because the driver and the rider's gender and age range are not the same. x^{rd} is found to be positive one for employment and socialness because they are working at the same location and they both want to meet with new people on a ride. In this situation, the score for gender becomes 1x5x(-1) = (5). When the scores for the other characteristics are calculated the same way, the JSS is calculated by simply adding the scores of each characteristic.

This algorithm assumes that routes of drivers are determined before the beginning of a ride and drivers do not change their routes to pick up a rider. This algorithm utilizes first comes first served approach, so that the matches found by the algorithm may not give the optimal result when the overall system benefit is considered. On the other hand, due to first comes first served approach, the algorithm shows good computation time performance. The social parameters are not utilized as constraints. A match is considered as feasible if the routes and time schedules of the participants are compatible and capacity of the vehicle is adequate.

There are some limitations of this algorithm. First of all, this algorithm utilizes greedy-heuristic approach that does not guarantee the optimal matches or maximum number of matches. This would cause decrease in quality

of matches, when the objective function is set to maximizing JSSs. Secondly, there are no constraint for social factors. This assumes that all participants will accept their matches, even if their JSSs are low. This case may not be valid in real-life, so the performance of the algorithm may decrease.

The JSSs are calculated separately for each rider. First, the objection function of the rider with the earliest trip announcement time is calculated. After this rider is matched using the objective function, the next rider is selected, and the process is repeated. The pseudo codes and flowchart of the biosequence based ride-matching algorithm are depicted in Fig. 1 and 2.

```
m =number of riders
n =number of drivers
for i in range(0,m) do
  if rider count > 0 then
    for j in range(0,n) do
      if driver capacity > rider count then
        Route feasibility is checked as in Figure 3.4
        if route is feasible then
          calculate socialness score {See Eqn.2.1}
        end if
      end if
    end for
  end if
  Match the rider with the best driver
  Eliminate the rider from the system
  capacity of the driver = capacity of the driver − rider count
end for
```

Figure 1. Pseudo code of the biosequence based ride-matching algorithm (Aydin 2019)

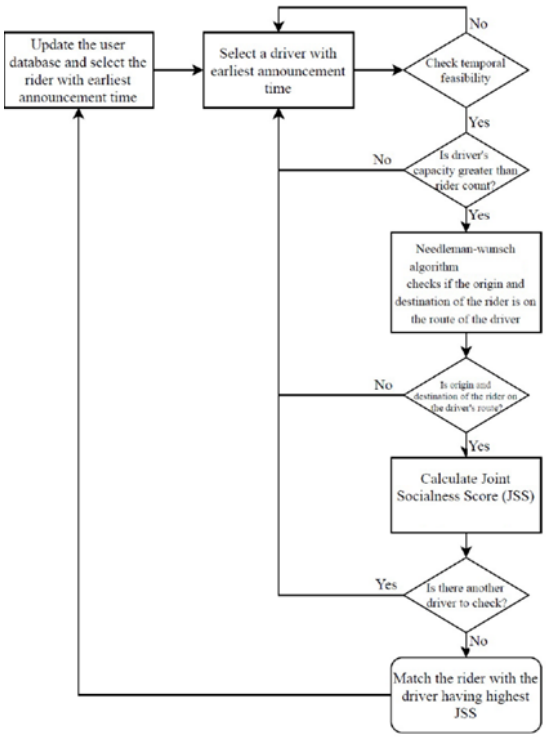

Figure 2. Flowchart of the biosequence based ride-matching algorithm (Aydin 2019)

2.2. Weighted Bipartite Ride-Matching Algorithm

The weighted bipartite matching algorithm can be constructed using several different objective functions, such as maximizing total distance savings, number of matches or fuel savings. In this paper, one of most preferred objective function, maximizing system-wide distance savings, are selected. This algorithm allows only single rider-single driver matches, because drivers change their routes to pick up riders. It also ignores the choices of participants. This study is extended by adding social parameters as constraints (Ghoseiri et al. 2011).

The algorithm builds arcs between each rider and each driver. These arcs are considered feasible if they create positive distance savings. Distance savings are calculated using the following equation (Agatz et al. 2011):

$$\sigma_{(i,j,k,l)} = d_{o_i d_i} - (d_{o_i k} + d_{kl} + d_{l d_i}) + \sum_{j \in R} (d_{o_j d_j} - (d_{o_j k} + d_{l d_j})). \quad (2)$$

In Eq. (2), distance savings are calculated for the scenario in which driver i picks up rider j from point k and drops him or her off at point l. To maximize system-wide distance savings, the calculations of distance savings are performed for all possible matches before any match is finalized. The matches are then finalized, starting with the match that offers the highest distance savings. Since all participants in the system must wait for the algorithm to make calculations for all possible matches, it takes a relatively long time to find a match for a participant.

There are some limitations of this algorithm. This algorithm utilizes heuristics that may not offer the optimal solutions. Furthermore, number of matches decreases dramatically when social factors are included as constraints; because, many feasible matches are eliminated, even if only one of the social characteristics is not compatible.

The pseudo code and flowchart of the weighted bipartite algorithm including social factors are presented in Fig. 3 and 4.

3. SIMULATION PROCESS

All matching algorithms were modeled in Python 2.7. Their performances were measured on a computer with an i5 2.7 GHz processor and 8 GB of RAM. All ride-matching algorithms were simulated using the same data and the same computer. To conduct a computational study, 1000 drivers and 1000 riders were randomly generated including their routes, origin/destination locations and social parameters. Drivers and riders are selected randomly from the generated data pool.

The algorithms were tested using different scenarios that are created with different number of riders, drivers, capacities of drivers and JSS limits. To measure the effects of including social parameters in an algorithm the biosequence based algorithm and weighted bipartite matching algorithm are simulated. Each case is simulated five times to eliminate the effects of stochastic behavior.

4. PERFORMANCE OF THE RIDE-MATCHING ALGORITHMS

Computation times of the matching algorithms with different combinations of independent variables are examined using multiple regression analysis. Independent variables are number of riders, number of drivers, capacity of each driver and JSS limits. Model summary and regression analysis for biosequence including social factors model results are given in Table 2 and 3, respectively.

```
m, n = number of riders, number of drivers
for j in range(0,n) do
  if driver capacity > 0 then
    for i in range(0,m) do
      if distance savings (Eqn. 5.1) ≥ 0 then
        if routes are compatible then
          if social choices are compatible then
            add to feasible matches
          end if
        end if
      end if
    end for
  end if
end for
for k in range(0,feasible_matches_count) do
  Select the match with max distance saving
  if driver_capacity > 0 then
    if driver is unmatched then
      Match the driver with the rider
      Eliminate the matched rider from the list
      driver_capacity = driver_capacity − 1
    else if driver is matched with other riders then
      if social choices are compatible between riders then
        Match the driver with the rider
        Eliminate the matched rider from the list
        driver_capacity = driver_capacity − 1
      end if
    end if
  end if
end for
```

Figure 3. Pseudo code of the weighted bipartite matching algorithm (Aydin 2019)

R^2 values of 0.88 shown in Table 2 states that the regression model explains 88% of the relationship between coefficients and computation times.

Table 2. Model summary of the regression for computation times

Model	R	R Square	Adjusted R Square	Std. Err. of the Estimate
Biosequence incl. social factors	0.938	0.880	0.879	2.3916
Biosequence excl. social factors	0.938	0.879	0.878	1.6465
Bipartite incl. social factors	0.999	0.999	0.999	0.7372
Bipartite excl. social factors	0.998	0.996	0.996	0.9086

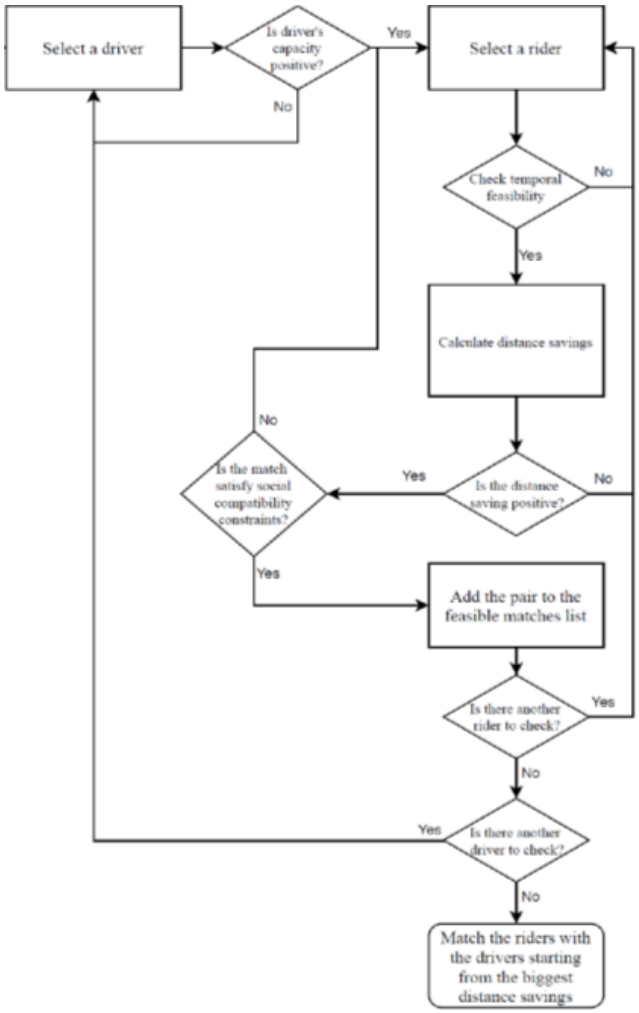

Figure 4. Flowchart of the weighted bipartite matching algorithm (Aydin 2019)

Table 3. Coefficients of the regression for computation times

Model: Bioseq. Incl. Social		Unstandardized Coefficients B	Unstandardized Coefficients Std. Error	Standardized Coefficients Beta	t	Sig.
1	(Constant)	-22.33	0.919		-24.52	0.00
	Number_of_riders	0.188	0.005	0.757	38.15	0.00
	Number_of_drivers	0.216	0.005	0.873	43.96	0.00
	Capacity	0.668	0.146	0.082	4.58	0.00
	JSS_Limit	-0.009	0.004	-0.050	-2.62	0.01

Table 3 shows that number of riders and drivers, capacities and JSS limits are significantly important for the computation times. Computation times increase as

the problem sizes and/or JSS limits increase. The relationship between number of riders and computation times are depicted in Fig. 5.

Figure 5 shows that including social parameters increases computation times of the weighted bipartite algorithm and biosequence based algorithm. The descriptive analysis for each algorithm is given in Table 4.

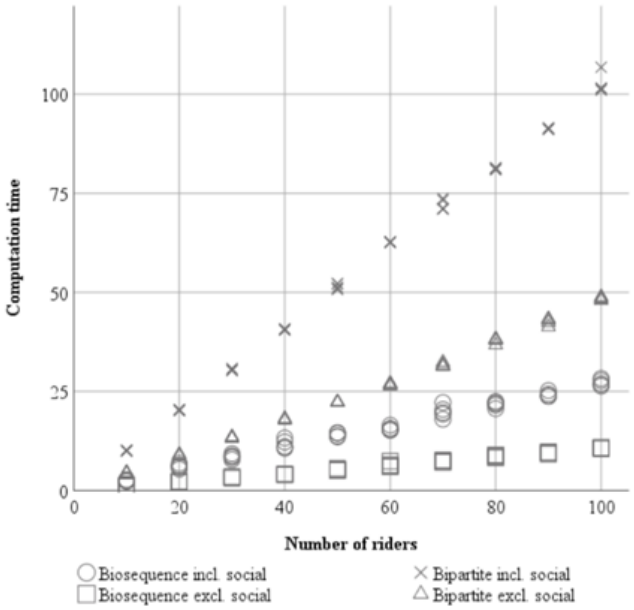

Figure 5. Computation times versus number of riders for the algorithms

Mean computation times given in Table 4 states that including social factors causes 71% increase in computation times for biosequence based algorithm and %220 increase for weighted bipartite algorithm. Average computation times of biosequence based algorithm are significantly lower than weighted bipartite algorithm because biosequence based algorithm utilizes first comes first served approach.

Table 4. Descriptive analysis of computation times for each algorithm

	N	Mean	Std. Deviation	Std. Error
Biosequence inc. social	412	13.9022	6.8767	0.3388
Biosequence exc. social	413	8.1387	4.7104	0.2318
Bipartite inc. social	413	68.5130	31.9897	1.5741
Bipartite exc. social	430	31.1825	14.6050	0.7043

5. QUALITY OF MATCHES

The importance of social parameters for matching riders and drivers in a ride-sharing system has been discussed in the literature. To achieve critical mass in ride-sharing, considering social parameters can be seen as one of the key factors (Agatz et al. 2012; Shaheen et al. 2018). In this paper, the quality of matches found by the algorithms are measured by analyzing the similarity between their choices and the matches. The similarities are scored by calculating the average JSSs of the matches found by the algorithms.

The simulation results of the biosequence algorithm and weighted bipartite algorithm including or excluding social parameters are shown in Fig. 6. In this Figure, the average of JSS scores of the matches found by the algorithms under different JSS limits are depicted.

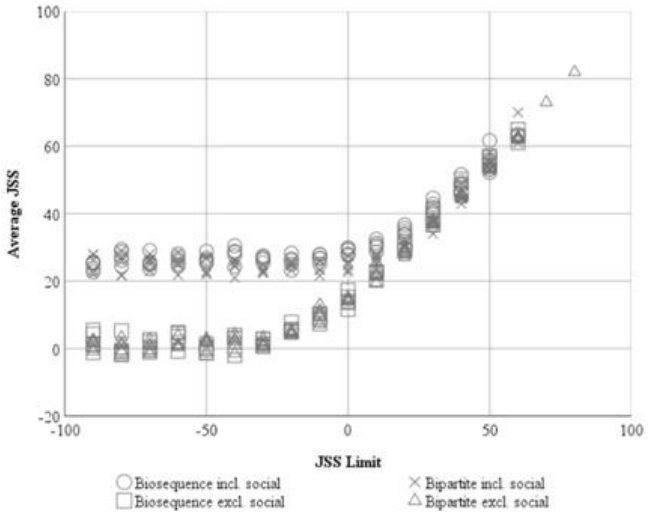

Figure 6. Average JSSs versus JSS limit for the algorithms

Figure 6 shows that including social parameters in the algorithms show better JSSs, even should there is no limit for JSS. This is because, the objective function of the biosequence matches riders and drivers, who have the highest JSS. Similarly, social parameters constraints used by the weighted bipartite algorithm eliminate the matches when there are one or more social parameters that are not compatible for drivers and riders. When there are no JSS limit, the average JSSs found by the algorithms are 26.43, -0.18, 23.65 and 1.32 for the biosequence algorithm including social parameters, biosequence based with excluding social parameters, weighted bipartite algorithm including social parameters and weighted bipartite algorithm excluding social parameters, respectively.

When a JSS limit is set, average JSSs of the matches found by the algorithm increases because the matches having lower JSSs than the JSS limit are eliminated. Therefore, the number of matches decreases with increasing JSSs. The relationship between the number of the matched riders and JSS limit is shown in Fig. 7.

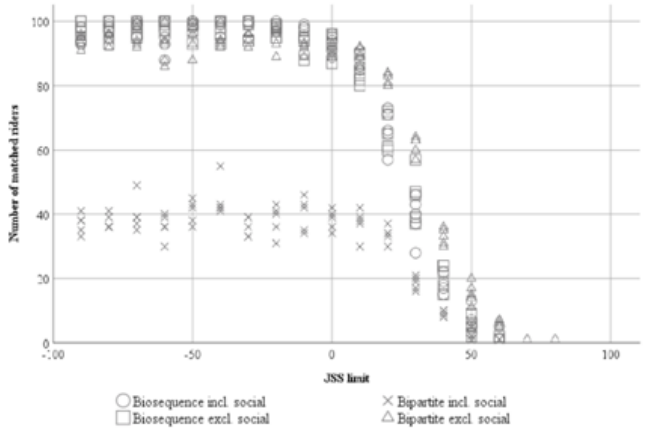

Figure 7. Number of matched riders versus JSS limit

Figure 7 shows that number of the matched riders significantly drops, when a JSS limit is set that is higher than the average JSSs found by the algorithms where no limit is set. The relationship between the average JSSs of the matches found the algorithms and number of matched riders are examined using regression analysis. Model summary and regression analysis results are given in Table 5 and 6, respectively.

Table 5. Model summary of the regression for average JSSs

Model	R	R Square	Adjusted R Square	Std. Error of the Estimate
1	,800	0.640	0.639	10.91

Table 6. Coefficients of the regression for average JSSs

Model		Unstandardized Coefficients		Standardized Coefficients		
		B	Std. Error	Beta	t	Sig.
1	(Constant)	52.18	1.314		39.71	0.00
	Number_of_matched_riders	-0.419	0.018	-0.800	-23.56	0.00

R^2 value of 0.640 shown in Table 5 states that the regression model explains 64% of the relationship between average JSSs and number of matched riders. Table 6 shows that number of matched riders are statistically significant to describe average JSSs. The regression results explain that when JSS limit is increased by one, number of matched riders decreases by 0.419. Consequently, it can be concluded that higher quality of the matches can be achieved but it costs reduction of number of matches.

6. CONCLUSION and DISCUSSION

Advancement in technology, especially smartphones, brings important advantages for ride-sharing. Dynamic ride-sharing system requires automated ride-matching. Ride-matching algorithms are at the center of ride-sharing systems that optimize matches between people with similar routes and schedules at short notice. Yet, computation times of these algorithms and the quality of the found matches are still studied by many researchers. In this paper, several ride-matching algorithms in the literature are modeled, simulation study is conducted and the results of the simulation study are analyzed. It is aimed (1) to present the effects of including social parameters and/or allowing different options, such as multiple rider-single driver match, on the performance of an algorithm and (2) to analyze the quality of the matches found by the algorithms.

The computation time of an algorithm is directly proportional to the number of computation. Therefore, including social parameters causes decrease in performance of the algorithms for biosequence based algorithm and weighted bipartite matching algorithm. Furthermore, first comes first served approach causes the most significant decrease in computation times but this approach does not promise to find the best possible matches in the system. As a result, it can be concluded that including social parameters has negative effect on the performance, whereas utilizing first comes first served approach positive effect. Consequently, while creating an algorithm, a trade-off analysis should be done to decide which variables to include or exclude.

Achieving critical mass in ride-sharing has been widely discussed in the literature, yet it is not achieved in real world. To achieve critical mass in ride-sharing, social characteristics and choices of participants should be analyzed. Most ride-matching algorithms omitted choices of participants that may lead participants to reject the matches found by the algorithms. Thus, in this paper, the quality of the matches is measured by scoring the similarity between social characteristics and choices of the matched participants. The results show that including social parameters in the algorithms has significant effect on the quality of matches. When objective function of the algorithm is to maximize social compatibility of riders and drivers, the quality of matches significantly increases while the number of found matches did not change. Similarly, when the social parameters are used as constraints in the weighted bipartite algorithm, the quality of matches are found to be significantly higher than the same algorithm excluding social parameters. On the other hand, number of matches decreases, because if one of the characteristics and choices of the participants are not compatible, the match is eliminated. Thus, many matches having low quality score were eliminated and average quality of the matches increased. As a result, including social parameters in a ride-matching algorithm and/or setting a limit for social compatibility score are very important for the quality of the matches but number of found matches may decrease. In the future, case studies should be conducted to measure the necessity of setting a limit for social compatibility so that number of matches can be maximized while satisfying enough social compatibility quality for potential participants.

As a conclusion, the performance of a ride-matching algorithm and quality of the matches found by an algorithm depends on the variables used in the algorithms. Including social parameters increase the quality of matches significantly while decreasing computation time performance. Furthermore, first comes first served approach cause significant decrease in computation times. In the future, it would be intriguing to analyze trade-off costs of such variables on the performance and quality of the various matching algorithms. The importance of social parameters and travel choices of potential participants in real-life should be investigated by conducting surveys. Thus, better understanding of participants' travel behavior can be achieved.

ACKNOWLEDGEMENTS

An earlier version of this paper was presented at iSTE-CE'2019- International Conference on Innovation, Sustainability, Technology and Education in Civil Engineering in Iskenderun, Turkey.

REFERENCES

Agatz N, Erera A L, Savelsbergh M W P & Wang X (2011). Dynamic ride-sharing: A simulation study in metro Atlanta. Procedia Social and Behavioral Sciences, 17, 532-550. DOI: 10.1016/j.sbspro.2011.04.530

Agatz N, Erera A, Savelsbergh M & Wang X (2012). Optimization for dynamic ride-sharing: A review, European Journal of Operational Research, 223(2), 295-303. DOI: 10.1016/j.ejor.2012.05.028

Aydin Ö F (2019). A Biosequence Based Ride-Matching Algorithm that Takes into Account Social Factors. PhD Thesis, Boğaziçi University, Department of Civil Engineering, Istanbul, Turkey.

Chan N D & Shaheen S A (2012). Ridesharing in North America: Past, Present, and Future. Transport Reviews, 32(1), 93-112. DOI: 10.1080/01441647.2011.621557

European Environment Agency (2005). Household consumption and the environment, 11, European Environment Agency.

European Environment Agency. (2015). Occupancy rates of passenger vehicles, European Environment Agency.

Ghoseiri K, Haghani A & Hamedi M (2011). Real-Time Rideshare Matching Problem. Final report, University of Maryland, Department of Civil and Environmental Engineering, MD, USA.

Gu Q-P, Liang J L & Zhang G. (2018). Algorithmic analysis for ridesharing of personal vehicles. Theoretical Computer Science, 749, 36-46. DOI: 10.1016/j.tcs.2017.08.019

Herbawi W M & Weber M (2012). A genetic and insertion heuristic algorithm for solving the dynamic ridematching problem with time windows. Proceedings of the Fourteenth International Conference on Genetic and Evolutionary Computation Conference, pp. 385-392. DOI: 10.1145/2330163.2330219

Nielsen J R, Hovmoller H, Blyth P-L & Sovacool B K. (2015). Of “white crows" and “cash savers:" A qualitative study of travel behavior and perceptions of ridesharing in Denmark. Transportation Research Part A: Policy and Practice, 78, 113-123. DOI: 10.1016/j.tra.2015.04.033

Qian X, Zhang W, Ukkusuri S V & Yang C (2017). Optimal assignment and incentive design in the taxi group ride problem. Transportation Research Part B: Methodological, 103, 208-226. DOI: 10.1016/j.trb.2017.03.001

Shaheen S & Cohen A (2018). Shared ride services in North America: definitions, impacts, and the future of pooling. Transport Reviews, 39(4), 1-16. DOI: 10.1080/01441647.2018.1497728

Shaheen S, Cohen A & Bayen A (2018). The Benefits of Carpooling. UC Berkeley: Transportation Sustainability Research Center. http://dx.doi.org/10.7922/G2DZ06GF.

CONTENTS

ISSN 2587-1366

TURKISH JOURNAL OF ENGINEERING

VOLUME 5 ISSUE 1 JANUARY 2021